

Contents lists available at [ScienceDirect](https://www.sciencedirect.com)

Geochimica et Cosmochimica Acta

journal homepage: www.elsevier.com/locate/gca

Towards a better understanding of the geochemical proxy record of complex carbonate archives

M. Mueller^{a,*}, B.F. Walter^{b,c,d}, R.J. Giebel^{e,f}, A. Beranoaguirre^{c,d,g}, P.K. Swart^h, C. Lu^h, S. Riechelmann^a, A. Immenhauser^{a,i}^a Institute for Geology, Mineralogy and Geophysics, Ruhr-Universität Bochum, Universitätsstraße 150, 44801 Bochum, Germany^b Eberhard Karls University Tübingen, Petrology and Mineral Resources, Schnarrenbergstraße 94-96, 72074 Tübingen, Germany^c Karlsruhe Institute for Technology, Chair of Economic Geology and Geochemistry, Adenauerring 20b, 76131 Karlsruhe, Campus South, Germany^d Laboratory for Environmental and Rawmaterial Analyses (LERA), Adenauerring 20b, 76131, Karlsruhe, Campus South, Germany^e Technische Universität Berlin, Ernst-Reuter-Platz 1, 10587 Berlin, Germany^f University of the Free State, 250 Nelson-Mandela-Drive, Bloemfontein 9300, South Africa^g Frankfurt Isotope and Element Research Center, Goethe-Universität Frankfurt, Altenhöferallee 1, 60438 Frankfurt am Main, Germany^h Department of Marine Geosciences, Rosenstiel School of Marine, Atmospheric and Earth Sciences, University of Miami, Miami, 33149, FL, USAⁱ Fraunhofer Research Institution for Energy Infrastructures and Geothermal Systems IEG, Am Hochschulcampus 1, 44801 Bochum, Germany

ARTICLE INFO

Associate editor: Chao Li

Keywords:

Carbonate geochemistry
Proxy record
Rock archive
Diagenesis
U-Pb dating
Dolomite
Dolomitisation
Paleothermometry
Karstification

ABSTRACT

Carbonate archives record a brief snapshot of the ambient Earth's surface conditions at their deposition. However, the geologically reasonable extraction and interpretation of geochemical proxy data from ancient, diagenetically altered rock archives is fraught with problems. Three issues stand out: the dichotomy between petrographic and geochemical alteration; the lack of quantitative age constraints for specific diagenetic phases resulting in a poorly constrained admixture of local, basin-wide and over-regional (far-field) features; and an often insufficient understanding of the temperatures and compositions of diagenetic fluids. Here, the archive of Devonian marine limestones exposed to multiple far-field diagenetic events is used as an example to explore the above-listed issues. Methods applied include petrography, micro XRF, fluid inclusion data, clumped isotopes, $\delta^{13}\text{C}$ and $\delta^{18}\text{O}$ isotopes, $^{87}\text{Sr}/^{86}\text{Sr}$ ratios and quartz trace element data. Devonian limestones studied here were overprinted by two cross-cutting regional fault zones ($T \approx 230\text{ °C}$) by multiple events between the Variscan Orogeny and the late Paleogene. The following processes are recorded: (i) protolith deposition and partial dolomitisation during rapid burial in the Middle/Late Devonian ($T \approx 180\text{ °C}$); (ii) deep burial to *ca.* 6.5 km and tectonic/hydrothermal overprint during the Variscan Orogeny in the Carboniferous ($T \approx 90\text{--}230\text{ °C}$); (iii) rapid uplift to 1–2 km burial depth at the end of the Variscan Orogeny and hypogene karstification ($T \approx 50\text{ to }100\text{ °C}$) initiated by regional geology in the Permian/Triassic; (iv) tectonic/hydrothermal overprint during the opening of the Proto-Atlantic Ocean between the Early Jurassic and the Early Cretaceous ($T \approx 50\text{ to }130\text{ °C}$); (v) tectonic/hydrothermal overprint including renewed hypogene karstification and hydrothermal calcite cement precipitation ($T \approx 50\text{ to }180\text{ °C}$) during Alpine Orogeny between the Late Cretaceous and late Paleogene. Despite this complex series of diagenetic events, the protolith limestones largely preserved their respective Middle/Late Devonian dissolved inorganic carbon (DIC) and $^{87}\text{Sr}/^{86}\text{Sr}$ signatures. This study documents that geochemical proxy data, placed into their petrographic, paleotemperature, and local to over-regional context, significantly increases the ability to extract quantitative information from ancient carbonate rock archives. Research shown here has wider relevance for carbonate archive research in general.

1. Introduction

Marine and terrestrial carbonate archives record, at the time of their

deposition, a brief snapshot of the ambient Earth's surface conditions (Folk, 1965; Veizer et al., 1999; Brand et al., 2011; Fantle et al., 2020 and reference therein). When these materials precipitate, they record a

* Corresponding author.

E-mail address: mathias.mueller-11y@rub.de (M. Mueller).<https://doi.org/10.1016/j.gca.2024.04.029>

Received 13 October 2023; Accepted 23 April 2024

Available online 1 May 2024

0016-7037/© 2024 The Author(s). Published by Elsevier Ltd. This is an open access article under the CC BY-NC license (<http://creativecommons.org/licenses/by-nc/4.0/>).

complex interplay of equilibrium and non-equilibrium processes (review in Swart, 2015). Carbonate minerals may form via amorphous precursor phases (Mavromatis et al., 2017), or the precursor mineral may undergo subsequent ripening in the sense of Ostwald's step rule (Nordeng and Sibley, 1994). Parameters such as fluid geochemistry, temperature, salinity, alkalinity and pH, mineralogy-dependent isotope fractionation, sulphate and vital/kinetic effects all interact in an often stochastic (but, under favourable conditions, deterministic) manner. The challenge of the carbonate archive researcher concerned with climate dynamics is to separate geochemical proxy data reflecting the environment at deposition from the plethora of non-equilibrium processes and the effects of later diagenetic or metamorphic alteration (Bathurst, 1971; Allan and Matthews, 1982; Higgins et al., 2018).

Carbonates, which have seen multiple phases of diagenetic or metamorphic overprint over geological time scales, represent the research frontier in this regard. Where possible, these archives are avoided, but for some regions of the world and particularly with regard to the deep time record, these archives might be the only ones at hand (Melezhik et al., 2005; Klein, 2005; Spence et al., 2016; Immenhauser, 2022). That said, geologically old archives are not necessarily overprinted, and geologically young ones are not always well preserved. Numerous workers have dealt with these issues, and new analytical techniques have resulted in a significantly improved understanding of geochemical proxy data in carbonate archives (Böhm et al., 2006; Fantle and Bullen, 2009; Geske et al., 2015; Schurr et al., 2021). Despite these advances, the geologically reasonable extraction and interpretation of environmental proxy data from geologically complex archives remain, where possible, a task fraught with problems. Three problems stand out: (i) the dichotomy between petrographic (recrystallisation and neomorphism) and geochemical resetting of a given archive and its proxy data, (ii) the scarcity of quantitative age constraints for specific diagenetic events resulting in an insufficient understanding of what are local, basin-wide and over-regional (far-field) effects, and (iii) and insufficient data of temperatures and compositions of diagenetic fluids. These issues are detailed below.

A growing number of often provocative studies (Czerniakowski et al., 1984; Ferry et al., 2002; Perrin and Smith, 2007; Bernard et al., 2017; Pederson et al.; Mueller et al., 2022a) has questioned the general assumption that petrographic alteration is *per se* indicative of geochemical alteration of geochemical proxy data (or *vice versa*), which must be increasingly seen as an oversimplification. The perhaps counter-intuitive implication is that some petrographically altered carbonates might still record fairly well-preserved marine proxy data, whereas others that seem petrographically or mineralogically (near) pristine were geochemically reset. At the earliest diagenetic end of the spectrum, aragonite-aragonite recrystallisation of corals (Perrin and Smith, 2007) and subtle yet significant diagenetic effects may have taken place in apparently pristine foraminifera or bivalve archives (Bernard et al., 2017; Lange et al., 2018), to name some examples. At the fully recrystallised, deep burial to the metamorphic end of the spectrum, high-grade marbles may still record what seems to be marine proxy data (Melezhik et al., 2005; Immenhauser, 2022). This is remarkable, as in many natural systems, advective or diffusive transport creates fluid-buffered systems, and a commonly held view is that metamorphism wipes out any useful environmental signal (discussion in Immenhauser, 2022).

The concept of basin-wide (or beyond) diagenetic events recorded in the paragenetic succession of carbonate archives and its geochemical archive has been discussed and is often referred to as 'far-field effects'. Examples include fluid migration oceanward into forearc basins and fluids from the compressional margin sediment wedge travelling into the continental interior (Oliver, 1986 'squeeze flow'). Generally, compressional fluid flow paths may be platform-wide (Blättler et al., 2019) or basin-wide (Yao and Demicco, 1995; Mueller et al., 2020), extending for hundreds of kilometres. The difficulty is to separate these events from what might be local diagenetic features. Recent work employs Uranium-Lead (U-Pb) age dating (Mangenot et al., 2018; Ganade

et al., 2022) of specific diagenetic phases, an approach that allows, under favourable conditions, far-field assignment and correlation of diagenetic events to basin-wide (and beyond) patterns (discussion in Mueller et al., 2020).

Fluid inclusion data of limestones and early-marine diagenetic dolostones track the circulation patterns and thermal history of ambient fluids at the time when the carbonate precipitated (primary fluid inclusion assemblages) or migrated through the porosity and fractures after precipitation (secondary fluid inclusion assemblages; Goldstein and Reynolds, 1994; Walter et al., 2015). Fluids are trapped whenever the crystal growth progresses, or cracks are healing. The crystal traps the fluid during growth and, therefore, archives the original conditions of fluid entrapment, i.e., the fluid composition and pressure-temperature conditions at the time of entrapment (Boiron et al., 2010; Walter et al., 2020a; Epp et al., 2019). When fluid inclusion data are combined with carbonate-clumped isotope geochemistry (Mangenot et al., 2017; Mueller et al., 2022b), a detailed paleotemperature evolution of a given carbonate archive may result that is of major significance when aiming to separate marine from later, diagenetic proxy data.

This paper makes use of the case example of a Devonian carbonate archive to test and explore the potential of the geochemical and petrographic tools applied here (Gillhaus et al., 2003; Balcewicz et al., 2021; Lippert et al., 2022) characterised by a particularly complex diagenetic history (Pederson et al., 2021). The aims of this paper are three-fold: (i) Compile an isotope geochemical, petrographic, diagenetic and structural framework for a carbonate archive that has seen multiple episodes of burial/hydrothermal and tectonic fault zone overprint. (ii) Apply fluid paleo-temperatures and fluid chemistry using carbon ($\delta^{13}\text{C}$), oxygen ($\delta^{18}\text{O}$) and strontium ($^{87}\text{Sr}/^{86}\text{Sr}$) isotope data with combined clumped isotopes/fluid inclusion microthermometry and place these data into a stratigraphic/temporal context employing U-Pb carbonate dating. (iii) Use these data as a litmus test for diagenetically complex archives with the question in mind to which degree environmental proxy data can be extracted. This contribution is of broad relevance and aims to provide a framework against which existing and subsequent work can be placed to extract quantitative science concerned with geochemical systems, mechanisms and processes.

2. Regional Geotectonic Setting

The Steltenberg Quarry, the study site of this paper, is located at the northern margin of the Remscheid-Altena Anticline, forming part of the Rhenish Massif of North Rhine-Westphalia (NRW), Germany (Fig. 1). From the Early to Middle Devonian, the depositional environment was dominantly shallow marine to deltaic siliciclastic, while in the late Middle Devonian reef development at the shelf edge and the open shelf prevailed. These carbonates form a massive limestone unit, now referred to as 'Massenkalk' (Fig. 1). At present, a lithostratigraphic revision for these massive limestones is in progress (e.g., Löw et al., 2022; Stichling et al., 2022).

The Devonian carbonate factories were active until the early Late Devonian. Afterwards, the sediment deposition was, once more, dominated by siliciclastics (Krebs, 1974). The Variscan Orogeny during the Carboniferous led to extensive folding and faulting in the area (Oncken, 1988, Fig. 1), during which hydrothermal ("warm" fluids; $T > 10$ to 15°C) mineralisation of the Rhenish Massif resulted in intensive dolomitisation of the massive limestone units (Kirnbauer et al., 1998; Richter, 2000; Gillhaus et al., 2003). Two main fault types occur in the neighbouring region of the Steltenberg Quarry, which may have caused secondary alteration of the Devonian units. Near-perpendicular (to the quarry orientation) fractures create networks in the Devonian carbonates along the northern margin of the Remscheid-Altena Anticline. The earliest fracture orientation is WSW-ENE-striking (Oncken, 1988). The study area's second main type of fault is an NNW-SSE-striking system of Post-Variscan age normal faults (Gillhaus et al., 2003). These normal faults represent reactivated extensional structures that formed

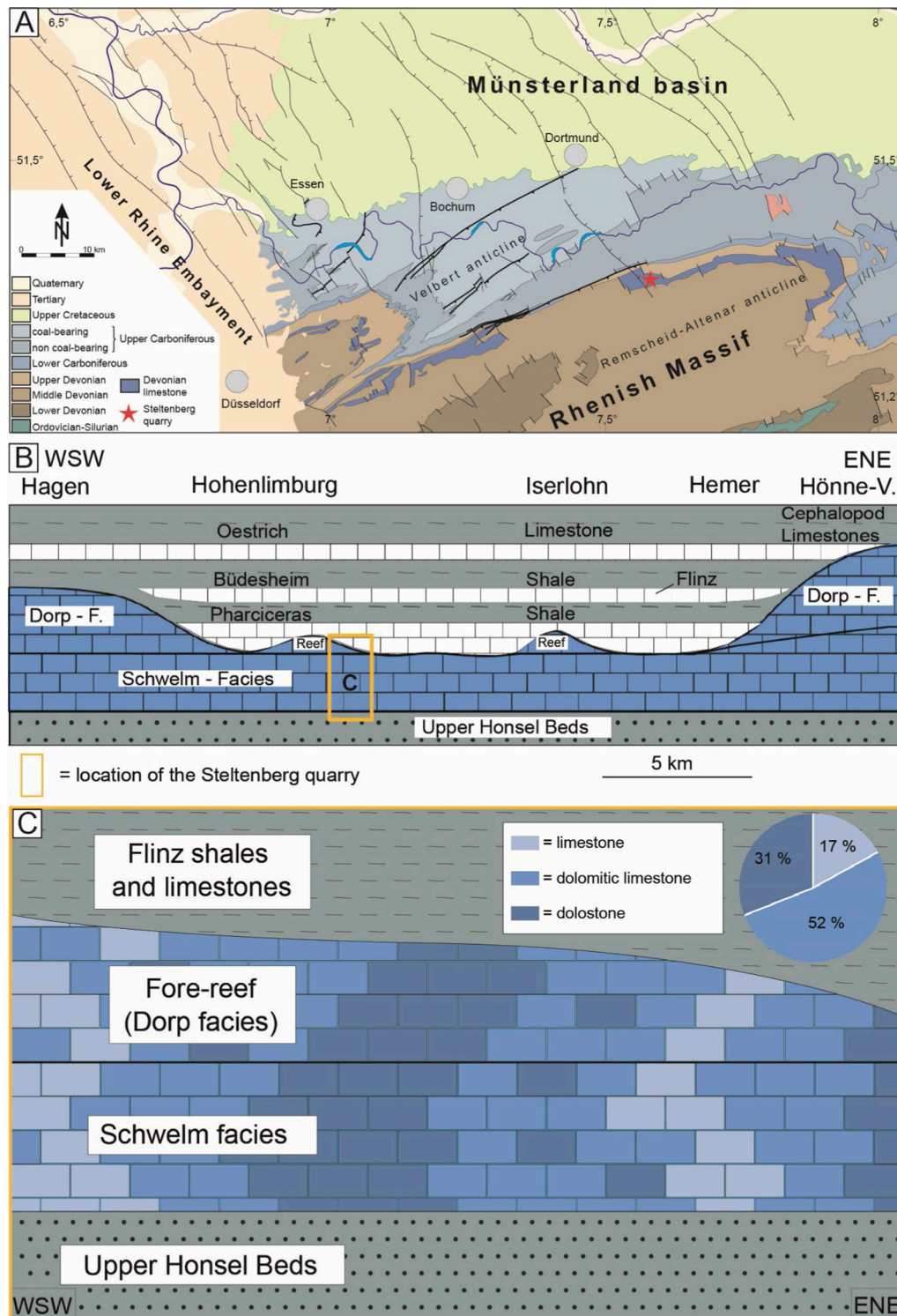


Fig. 1. (A) Geological map of the northern Rhenish Massif. The studied outcrop in the Devonian Massenalk is indicated by a red star (modified from Götte, 2004; Pederson et al., 2021). (B) Cross-sectional schematic redrafted from Krebs (1974) through the carbonate range on the northern flank of the Rhenish Massif (after Beckmann, 1948; Rosenfeld, 1961; Kamp, 1968; Krebs, 1974). The yellow frame marks the location of the Steltenberg Quarry, which is schematically displayed in (C). (C) Depositional and mineralogical facies model of the Devonian carbonate depositions of the Steltenberg Quarry in Hagen, including top and footwall layers of siliciclastic sediments (Krebs, 1974; Koch et al., 2018). The carbonates, displayed as a tiled pattern, are represented by the Schwelm facies and the fore-reef subtype of the Dorp facies and are equally affected by the fracture-related, hydrothermal dolomitisation leading to the quarry-wide mineralogical facies distribution as indicated by the colouration of the tiles and shown in the cake diagram. Modified from Pederson et al., 2021.

perpendicularly to the strike of the fold belt at the end of the Paleozoic due to crustal uplift and stretching until the Givetian, prior to the Variscan Orogeny. During that time, a clockwise rotation of the compressive stress field caused an NNW SSE extension. While the direction of this extensional regime changed slightly, this stress field is still active (Oncken, 1988). More recently, a third fracture orientation (WSW-ENE) cross-cutting older fractures and veins was reported (Balcewicz et al., 2021; Lippert et al., 2022).

The Devonian carbonates of the northern part of the Rhenish Massif near the study area were buried to a maximum depth of about 6.5 km during the later stages of the Variscan Orogeny roughly 300 Myr ago.

Since the Permian (Zechstein), the Paleozoic pre- and *syn*-Variscan sediments of the region have been uplifted and thus cooled, while overburden thicknesses of 4–5.5 km have been eroded in the study area (Littke et al., 2000; Nöth et al., 2001; Götte, 2004). Karstification of the Devonian Massenkalk units is a common feature, and numerous cave systems are known from the area (Niggemann et al., 2018 and references therein; Immenhauser et al., 2023). For many of these, a tectonically induced hydrothermal (Mesozoic-Cenozoic) and/or meteoric-phreatic (Oligocene-Recent) formation was documented (Drozdowski et al., 2017; Niggemann et al., 2018; Richter et al., 2020).

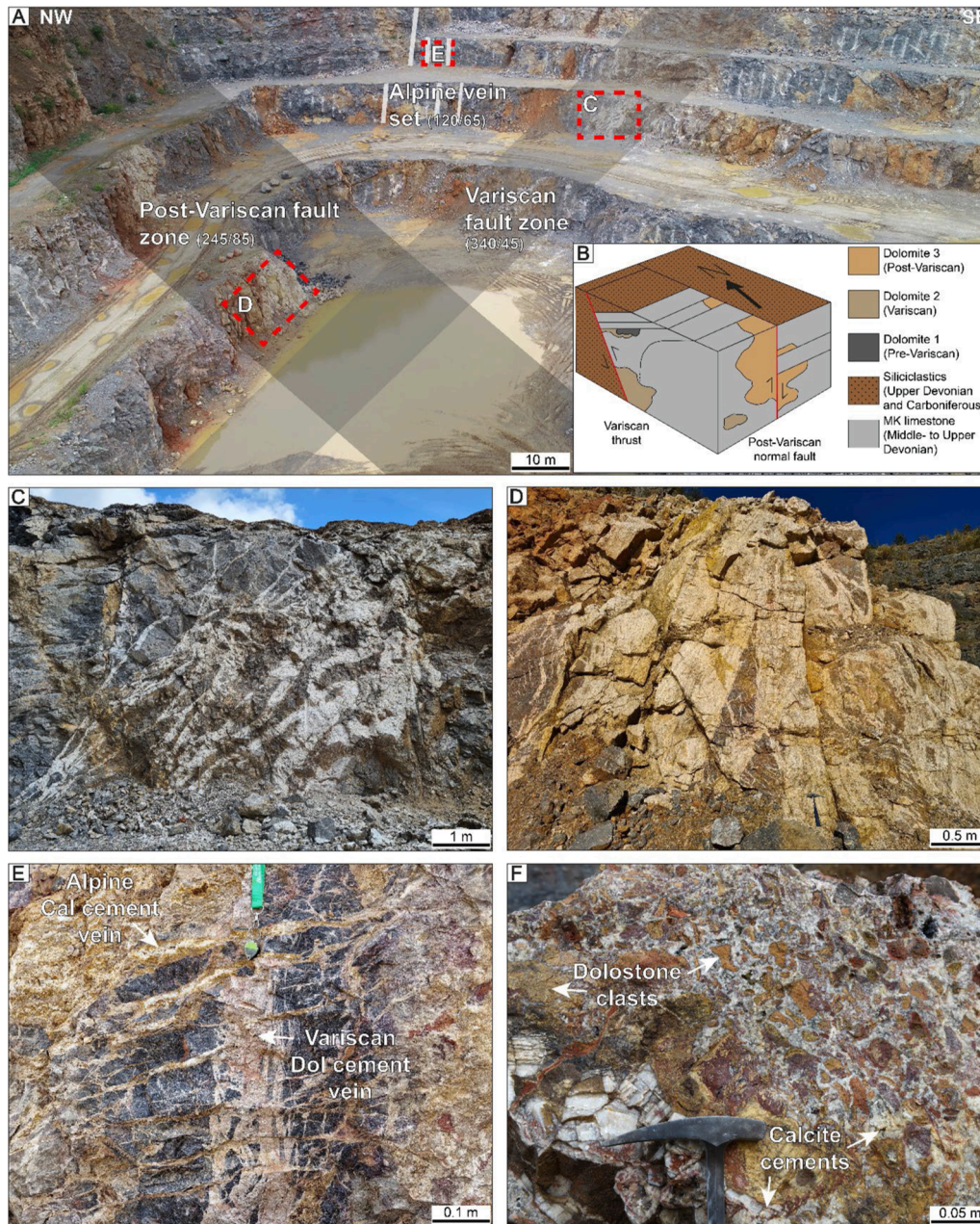


Fig. 2. (A) Drone image displaying the WSW-ENE (340/45) striking secondary faults of a Variscan thrust fault zone and the NNW-SSE (245/85) striking Post-Variscan normal fault zone in the northeastern part of the quarry. A third vein set (120/65) cuts through veins associated with the Post-Variscan fault zone. Note that the mineralisation of all three tectonic structures cross-cut each other, resulting in very complex mineral paragenesis. (B) Schematic model of dolostone occurrence in Steltenberg Quarry. Modified from Gillhaus et al. (2003). (C) Variscan mineralisation containing metre-sized dolostone clasts floating in blocky calcite cement. (D) Some prominent calcite mineralisation (up to ~15 m thick) of the Post-Variscan main fault in the northwestern quarry wall. It contains metre-thick radial calcite veins, including m-sized dolostone fragments in the cement. (E) Calcite vein set cutting through dolomite cement veins from the Post-Variscan fault zone. This vein set represents a geologically younger tectonic event. (F) One of the most prominent breccias with oxidised clasts, dolomite and calcite cement from the southern quarry wall in the main strand of the Post-Variscan fault zone.

3. Methodology

3.1. Sampling strategy

The Devonian Massenkalk (Figs. 1-3) was the chosen target for this study because it offers a wide range of carbonate rock types and is a highly complex geochemical archive, including well-preserved limestones to various types of (partly dedolomitised) dolostones. This region's Devonian geological and tectonic framework is well-established (Schaeffer, 1984; Oncken, 1988; Gillhaus et al., 2003; Götte, 2004 and references therein). To assess the spatial variability of diagenetic and tectonic impact on geochemical proxy data, the following approach was used: (i) 71 hand specimens with visible diagenetic features were

collected throughout the quarry to assess the complete paragenetic succession and their geochemical composition for the reconstruction of paleo-fluid flow and its relation to fault zone overprint. Detailed fluid petrography was performed to assess microthermometric data of all measurable diagenetic phases. A combination of microthermometry and clumped isotope analysis was then applied to reconstruct the paleo-temperature evolution of these rocks. Micro XRF maps were recorded to be applied for U-Pb age dating of suitable phases in the paragenetic succession.

3.2. Petrography

A total of 127 polished thin sections were analysed using both

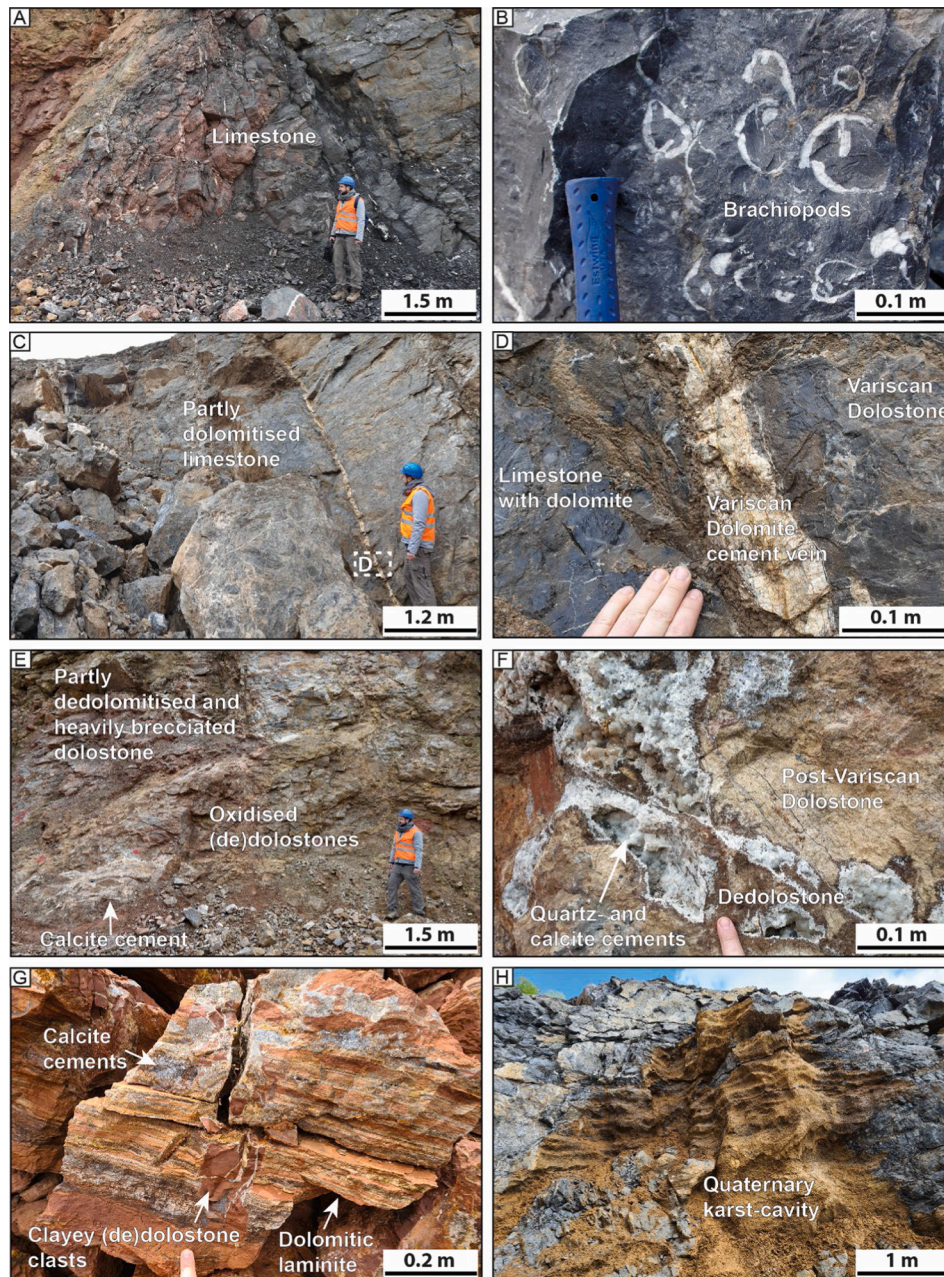


Fig. 3. Field images of the main facies types in the Steltenberg Quarry. (A, B) Devonian Massenkalk limestone. (C, D) Partly dolomitised limestones and Variscan dolostones, including dolomite cement veins. (E, F) The main strand of the Post-Variscan fault zone (southern quarry wall) includes very porous Post-Variscan dolomite-, dedolomite- and calcite cement in a heavily oxidised and dedolomitised breccia. Modified from Pederson et al., 2021. (G) Dolomitic laminite in breccia from the main strand of the Post-Variscan fault zone. Note the intercalation of clayey brown carbonate sediments and dolomitic cement layers. (H) Oligocene-Recent karst cavities up to several tens of metres are common in the Steltenberg Quarry.

polarised and cathodoluminescence microscopy. Polarised images were taken on a Leica DM4500P microscope (Leica Microsystems GmbH, Wetzlar, Germany). Cathodoluminescence analyses were performed using a hot cathode (HC1-LM) facility at the Ruhr-Universität Bochum (Neuser et al., 1996) equipped with a DC73 camera system (Olympus). Thin sections were sputter coated with a 15 nm thick gold layer to avoid charging. The electron beam had an acceleration voltage of 14 kV, a current density from 5 to 10 $\mu\text{A}/\text{mm}^2$, and a beam current from 0.1–0.2 mA. Dolomite and calcite cement phases were identified based on different luminescence colours representative of their diagenetic formation environment (following Bruckschen and Richter, 1993) and textural criteria after Friedman (1965), Sibley and Gregg (1987), Flügel (2004). By evaluating the various cement phases with each other, a paragenetic sequence, from earliest to latest precipitates, was developed. For further details on cement stratigraphy using cathodoluminescence microscopy, see Bruckschen et al. (1992), Bruckschen and Richter (1993) and Richter et al. (2003).

3.3. Micro XRF

Elemental distribution and macro textures in thin sections were investigated using the “area” mode of a Bruker Tornado M4 microXRF at the Mineralogical and Geochemical Micro-Analytical Laboratory (MAGMA Lab, Department of Applied Geochemistry, Technische Universität Berlin, Germany). The acceleration voltage was 50 kV using a beam current of 600 μA . The measuring point distance was 30 μm at a 20 μm beam diameter. The measuring time was 60 ms per analysis spot. The analyses were run with two simultaneously operating spectrometers to obtain more precise data from a stronger signal.

3.4. Fluid inclusion thermometry

Microthermometric analyses were conducted using a Linkam THMS600 heating and freezing stage at the Laboratory of Environmental and Raw Material Analyses (LERA) facilities at Karlsruhe Institut für Technologie (KIT). Double-polished thick sections (100 to 150 μm) were prepared. The petrographic relation of fluid-inclusion assemblages was carried out by optical and cathodoluminescence microscopy (Goldstein and Reynolds, 1994). Fluid-inclusion assemblages (FIA) were classified as (i) primary inclusions situated in growth zones (p), (ii) pseudo-secondary (ps), (iii) secondary (s), and (iv) isolated inclusions with no genetic relationship (iso; Walter et al., 2015). For each analysis, three repeated heating and freezing cycles were performed to document the final dissolution temperature of ice ($T_{m, \text{ice}}$) and hydrohalite ($T_{m, \text{hh}}$) and the homogenisation temperature (T_h). Fluid-inclusions were considered only when a triplet measurement varied between 0.1 $^\circ\text{C}$ for $T_{m, \text{ice}}$ and $T_{m, \text{hh}}$ and 1 $^\circ\text{C}$ for T_h . Each fluid inclusion was visually inspected (inclusion shape, volume fractions, pinch-off textures) and compared with the neighbouring fluid inclusions within an FIA employing reproducible measurements to strictly exclude the following post-entrapment modifications: necking down, leakage, decrepitation, re-equilibration, post-entrapment migration of FI and inclusion-wall precipitation. Fluid inclusions that do not fulfil the quality criteria due to post-entrapment effects were not measured. Additional details on the fluid-inclusion methodology can be found in the digital supplement S1.

3.5. Crush leach analysis

Following the method of Mueller et al., (2022b), 20 samples with one

dominant fluid type (evaluated by detailed fluid inclusion petrography) were selected for bulk fluid crush-leach analyses to determine major-, minor-, and trace-element compositions. About 2 g of carbonate with a grain size of 0.5 to 1 mm were hand-separated, and visible impurities were removed. See the digital supplement S1 for details.

3.6. Mineralogy, element and isotope geochemistry

The mineralogy of individual cement phases was analysed using powder X-Ray Diffraction (PXRD). A total of 70–100 mg of powder was drilled from the samples with a handheld Dremel to identify the minerals present. Sampling locations within individual phases were based on previous petrographic evaluation using normal, polarised and cathodoluminescence microscopy.

Element concentrations, carbon- and oxygen-isotope values ($\delta^{13}\text{C}$ and $\delta^{18}\text{O}$), and $^{87}\text{Sr}/^{86}\text{Sr}$ ratios were analysed at Ruhr-Universität Bochum. For $\delta^{13}\text{C}$ and $\delta^{18}\text{O}$ analysis, 90–110 μg of carbonate sample powder was reacted with phosphoric acid (concentration 104 %) at 70 $^\circ\text{C}$ before analysis. Isotope values were determined using a MAT 253 (Thermo Fisher Scientific) continuous flow isotope ratio mass spectrometer (CF-IRMS) coupled with a ConFloIV and a GasBenchII. Values are reported in ‰ relative to the VPDB standard. Measurement error is reported as 1 σ standard deviation (SD).

Elemental concentrations (Ca, Mg, Sr, Fe, Mn) were measured for all carbonate phases. Samples were run by dissolving approximately 1.5 mg of sample powder in 1 ml 3 M HNO_3 for 24 h at room temperature before diluting with 2 ml deionised water. Concentrations were determined by inductively coupled plasma optical emission spectrometry (ICP-OES, iCAP 6500 DUO, Thermo Fisher Scientific).

Strontium-isotope ratio analyses were performed by dissolving between 0.3 to 16.3 mg (to receive a Sr content of 400 ng per sample) of sample powder in 1 ml 6 M HCl and dried on a hot plate at 90 $^\circ\text{C}$ before being re-dissolved in 0.4 ml 3 M HNO_3 . Perfluoroalkoxy alkane (PFA) polymer columns filled with TrisKem Sr ion exchange resin (100–150 mesh) were used to collect the Sr fraction with 2 ml of deionised water. Subsequently, samples were dried on a hot plate at 90 $^\circ\text{C}$ and re-dissolved in 1 ml of a H_2O_2 - HNO_3 (1:1; 30 %:65 %) to remove organic remains. Samples were then evaporated on a hot plate at 60 $^\circ\text{C}$ and re-dissolved in 0.4 ml 6 M HCl. After evaporation at 90 $^\circ\text{C}$, samples were re-dissolved in 1 μl of ionisation-enhancing solution (after Birck 1986) and loaded on Re single filaments. Isotope ($^{87}\text{Sr}/^{86}\text{Sr}$) ratios were analysed by thermal ionisation mass spectrometry (TIMS) TI-BOX (formerly MAT 262; Spectromat). Details on the standards used and long-term reproducibility for all geochemical methods can be found in the digital supplement S1.

3.7. Clumped isotope analysis

Single-phase powder samples were used for clumped-isotope analysis. The samples were hand-drilled based on a detailed petrographic assessment (field observations, transmitted light microscopy, cathodoluminescence; Table 1). Each measurement of the Δ_{47} value requires 8 mg of carbonate to produce sufficient CO_2 for analysis. Samples were weighed into copper reaction boats and reacted using the common acid bath at 90 $^\circ\text{C}$, using concentrated phosphoric acid (density = 1.95 g/cm³) on the University of Miami Stable Isotope Laboratory’s vacuum line.

The $\delta^{13}\text{C}$ and $\delta^{18}\text{O}$ values of the reference gas were determined by analysing NBS-19 (National Bureau of Standards) and data for the

Table 1

Summary of the petrographic characteristics in the paragenetic sequence (starting at the bottom with precursor MK limestone and ending with LMC 10 at the top) of the Steltenberg Quarry, including characteristic features, crystal size, volumetric significance and luminescence colours. Additional petrographical data for all phases is provided in the digital supplement S1.

Phase	Characteristic features	Crystal size	Vol. significance	Luminescence
LMC 10	Forms mm to 1 cm sized botryoidal cements in open pores and on karstified surfaces	Micro to macrocrystalline	Very low	Bright yellow-orange-red zoned to magenta
LMC 9	Forms mm to cm sized clear crystals with thin Fe-oxide layers and crusts on LMC 7, low formation temperature, overprints all older phases	Micro to macrocrystalline	Low	Intrinsic dark blue with bright yellow zonation, often overprints older cfs
LMC 8	Forms mm sized clear crystals grown in Post-Variscan breccia	Micro to macrocrystalline	Low	Dark red to bright red zonation
LMC 7	Forms cm sized cloudy to clear crystals covered by thin Fe-oxide layer	Macrocrystalline	Low	Patchy orange to zoned red
LMC 6	Forms mm to cm sized brown (6A) to white (6B-D) crystals grown discordantly on LMC 5 and around breccia clasts in Post-Variscan fault zone	Macrocrystalline	Moderate	Patchy dark orange to clear red zonation
LMC 5	Forms dog tooth to radial cm to dm-sized clear to cloudy brownish crystals in veins + mm to cm sized white blocky crystals in breccias from Post-Variscan fault zone	Macrocrystalline	Moderate	Bright orange to patchy phase A and patchy bright yellow phase B
Dedol 3	Retained Dol 2 and Dol 3 crystal structure, very porous, etched surface, appears below Late Cretaceous-Paleogene hydrothermal calcites, macroscopically brown-red	Micro to macrocrystalline	Low to moderate	Patchy dark red to red
LMC 4B	Forms brown to dull white μm to cm-sized radial and blocky crystals	Micro to macrocrystalline	Low	Non-luminescent to yellow zoned
LMC 4A	Occurs along grain boundaries in LMC 3 and older phases	Microcrystalline	Low	Patchy bright yellow
Sulphides	Chalcopyrite, pyrite, locally forming crusts on breccia clasts, overprinted by later oxides	Crypto- to macrocrystalline	Insignificant	Non-luminescent
Qz 2	Forms clear to yellow crystals, forms crusts on Dol 3, clearly related to Post-Variscan fault zone	Microcrystalline to cm-sized	Low to moderate	Dark blue to pale blue
Qz 1	Small crystal size, green luminescence, one m-thick gangue known, clearly related to Post-Variscan fault zone renewed hydrothermal activity	Crypto- to microcrystalline	Low	Dark green to pale bright green
LMC 3	Forms cm to dm-sized fibrous (in klefts) blocky (in breccia) crystals, indications of fast skeletal growth, clearly related to Post-Variscan fault zone	Macrocrystalline	Moderate	Dark red to red zoned
Fe-oxides	Hematite, Goethite, limonite occurring as clasts in breccia or crusts on other paragenetic phases	Microcrystalline	Low	Non-luminescent
Dedol 2	Retained Dol 3 crystal structure, very porous, etched surface, low formation temperature, macroscopically brownish	Micro to macrocrystalline	Moderate to high	Patchy dark red, orange-yellow
Dol 3B	Skeletal and saddle growth, undulous extinction, often etched and at least partly dedolomitised, macroscopically light beige	Macrocrystalline	Moderate to high	Patchy pale dark to bright orange
Dol 3A	Matrix dolomite, locally forms saddle dolomites as cavity infill in cell dolomite	Micro to macrocrystalline	Moderate	Patchy dark red to dark pale orange
LMC 2	Forms cm to dm-sized blocky, cloudy to pale clear crystals associated to Laminite 1 and also forms a m-sized vein in the Post-Variscan fault zone	Macrocrystalline	Moderate	Clear red to orange zoned phase A and non-luminescent phase B
Laminite 1	Forms laminae of Dol cement and clayey redbrown dolopackstone in Post-Variscan fault zone; occurs in 10m-sized karst cavities or as clasts in collapse breccia	Micro to macrocrystalline	Moderate to high	Patchy red to bright orange
LMC 1	Forms around dol breccia clasts, macroscopically white, highest formation temperature, reactivation of Variscan thrust fault zone	Macrocrystalline	Moderate to high	Dark red
Dedol 1	Brownish mm thick layers and dedolomitised clasts on top and in Dol 2B, retained crystal structure of Dol 1 rhombs	Micro to macrocrystalline	Low	Non-luminescent to patchy dark red
Dol 2B	Forms beige saddle dolomite veins next to Dol 2A, clear field relation to Variscan thrust fault zone, contains breccia of older dolomite and limestone clasts	Macrocrystalline	Moderate to high	Patchy pale bright red
Dol 2A	Brown replacement dolomite clearly related to Variscan thrust fault zone	Micro to macrocrystalline	High	Dark red to patchy pale bright red
Dol 1B	Forms white saddle dolomite veins	Micro to macrocrystalline	Low	Patchy pale orange
Dol 1A	Macroscopically only dark grey dolomite in the paragenesis	Micro to macrocrystalline	Moderate	Red to pale orange
MK Fossils	Non-recrystallized pristine shell material (brachiopods, crinoids)	Macrocrystalline	Low	Dark red (brachiopod); red (crinoid)
MK limestone matrix	Hostrock, dark, organic rich, contains marine to burial cements and fossil detritus, mostly wackestones to floatstones	Micro to macrocrystalline	Very high	Pale bright red

samples reported relative to Vienna Pee Dee Belemnite (V-PDB) using the conventional notation. The $\delta^{18}\text{O}$ values for dolomite have been corrected by 0.8 ‰ to account for the differential fractionation of ^{18}O during dolomite formation compared to calcite (Sharma and Clayton, 1965).

Calculation of temperature and fluid $\delta^{18}\text{O}$ values: For lab-internal consistency, the calculation of temperatures was performed using the calibration of Swart et al. (2019), which is statistically identical to the later calibration for the Intercarb-CDES scale as published by Anderson et al. (2021):

$$\Delta_{47} = 0.0392 * 10^6 / T^2 + 0.158.$$

Calculation of the $\delta^{18}\text{O}$ values of fluids ($\delta^{18}\text{O}_f$) was performed using the equation of Kim and O'Neil (1997) and Horita (2014) for calcite and dolomite, respectively. See the digital supplement S1 for analytical details.

3.8. U-Pb age dating

Uranium-Pb isotopic ratios were collected on a ThermoFisher Element XR sector-field single-collector ICPMS coupled to a 193-nm ArF Excimer laser with a HelEx 2- vol cell (Analyte Excite+, Teledyne PhotonMachines) at LERA, Karlsruhe Institute of Technology (Germany), using the method described by Beranoguirre et al. (2022). The ablation

was carried out in a helium atmosphere, and argon and nitrogen were added before the plasma torch. The instrument was adjusted to obtain the best compromise between the sensitivity, oxide formation ($UO/U < 0.1\%$) and element fractionation (i.e., $Th/U = \sim 1$). Static ablation used a spot size of $150\ \mu\text{m}$ in diameter and a fluence of $2\ \text{J}/\text{cm}^2$ at 10 Hz. For analytical details, see the digital supplement S1.

The soda-lime glass SRMNIST612 (Jochum et al., 2011) was used as the primary reference material to correct for mass bias ($^{207}\text{Pb}/^{206}\text{Pb}$) and the inter-element fractionation and instrumental drift ($^{206}\text{Pb}/^{238}\text{U}$) during the analytical session. Additionally, carbonate reference material WC-1 (254 Ma, Roberts et al., 2017) was used to correct the different behaviour during the ablation of the carbonate and SRMNIST612. The

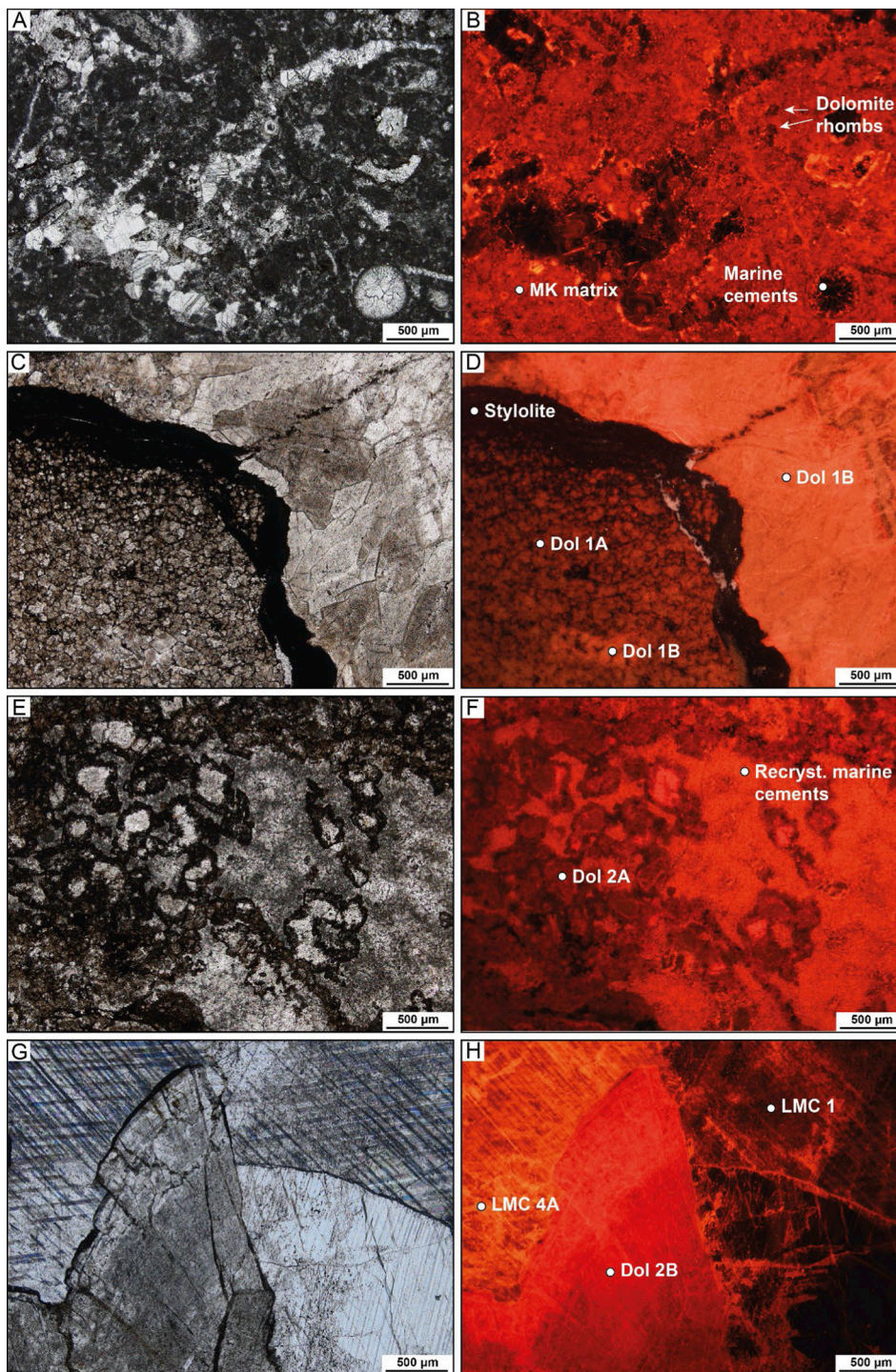


Fig. 4. Transmitted light and corresponding cathodoluminescence images of the Massenkalk limestone and Variscan fault zone-related carbonates in the Steltenberg Quarry. (A, B) Bright red luminescent Massenkalk limestone, including marine cements and a few dolomite rhombs grown in the matrix. (C, D) Red to pale orange luminescent Devonian dolomite Dol 1A (subhedral matrix dolomite) and Dol 1B (anhedral saddle dolomite). Note the stylolite that developed as a result of pressure solution during burial. (E, F) Stromatopore with marine cements from MK limestone partly replaced by euhedral to anhedral, dark red to patchy pale orange luminescent Dol 2A. (G, H) Anhedral bright red to patchy pale orange luminescent Dol 2B saddle dolomite overgrown by blocky calcite generations LMC 1 and LMC 4A. Note that LMC 4A is genetically related to the Post-Variscan fault zone, which locally overprints older paragenetic phases.

correction values estimated on the common Pb-corrected WC-1 were applied to all carbonate samples, assuming similar behaviour. Secondary reference calcite materials, JT-1 (Guillong et al., 2020) and B-6 (only LA-ICPMS data, Pagel et al., 2018), were measured for quality control.

Raw data were corrected offline using an in-house VBA spreadsheet program (Gerdes and Zeh, 2006, 2009). Uncertainties for each isotopic ratio are the quadratic addition of the within-run precision, counting

statistic uncertainties of each isotope, and the excess of scatter and variance (Horstwood et al., 2016) calculated from the SRM NIST 612 and the WC-1 after drift correction. Data were displayed in Tera-Wasserburg plots, and ages were calculated as lower Concordia-curve intercepts using the same algorithms as Isoplot 4.15 (Ludwig, 2012).

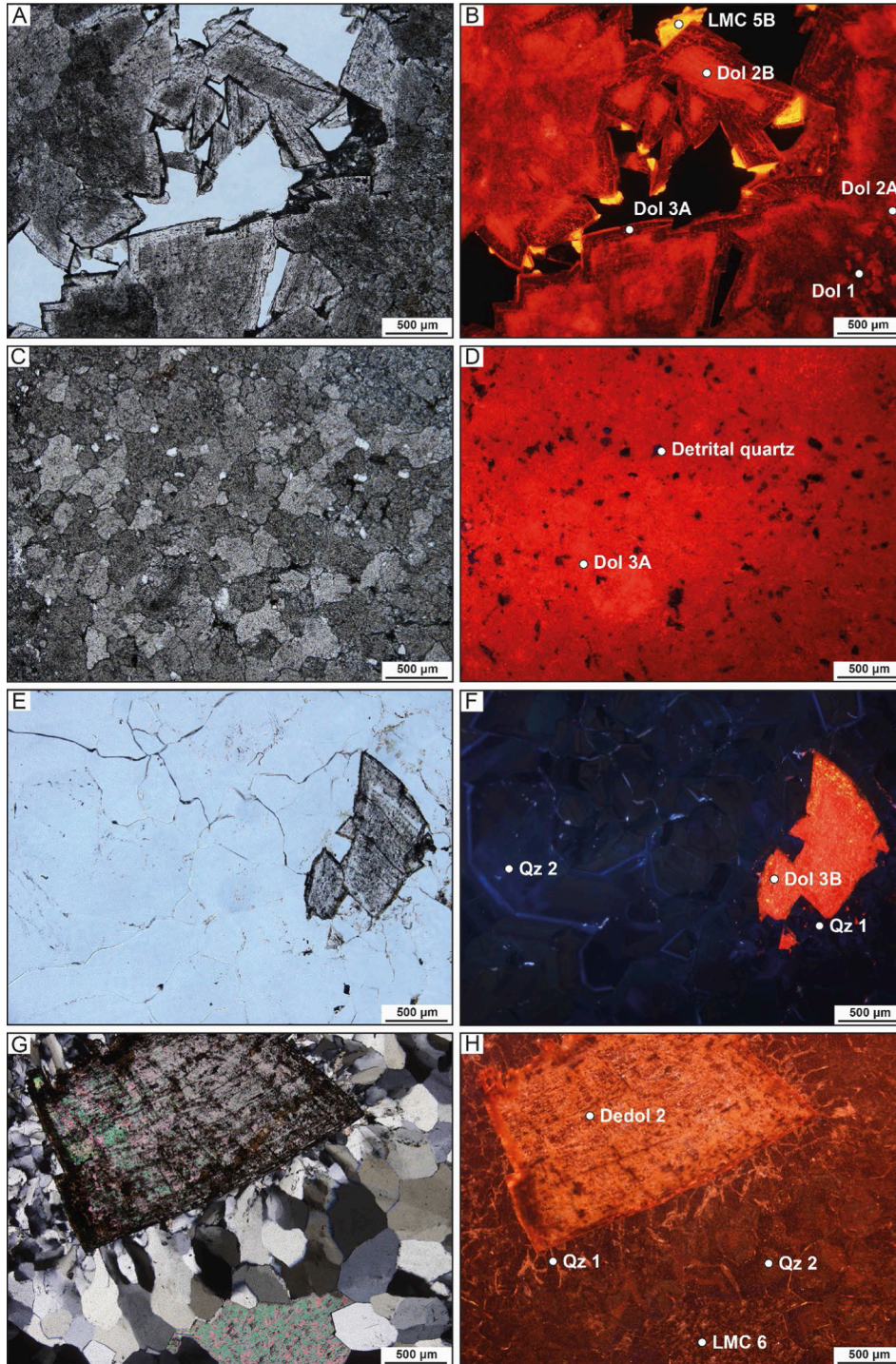


Fig. 5. Transmitted light (G: crossed polarisers) and corresponding cathodoluminescence images of the Post-Variscan fault zone related carbonates in the Steltenberg Quarry. (A, B) Euhedral to anhedral Dol 3A overgrows Dol 1 and Dol 2, clearly visible by its patchy dark red luminescence. (C, D) Anhedral patchy dark orange luminescent Dol 3A matrix dolomite with detrital quartz grains. (E, F) Anhedral patchy pale orange-luminescent Dol 3B saddle dolomite is overgrown by the blue to green-luminescent quartz phases Qz 1 and Qz 2. (G, H) Dedolomitised Dol 3 (=Dedol 2) from the Post-Variscan fault zone core is generally patchy red to patchy orange luminescent. In the fault zone core, the quartz phases Qz 1 and Qz 2 appear red-luminescent rather than their typical blue or green luminescence. (G) depicts a cross-polarised image to display the grain size difference between Qz 1 and Qz 2. The pore-filling phase LMC 6 is patchy dark red luminescent.

3.9. Trace elements in quartz

In-situ trace element compositions of quartz were obtained by laser ablation inductively coupled plasma mass spectrometry (LA-ICPMS) using a Teledyne Analyte Excite + ArF (193 nm) excimer laser ablation

system coupled to a Thermo-Scientific Element XR sector field mass spectrometer at LERA, KIT following the method of Walter et al. (2023a). For analysis, a laser spot size of 65 μm , a pulse rate of 10 Hz and an energy density of 11.0 J/cm^2 were used. See the digital supplement S1 for analytical details. The laser spots follow a transect through the

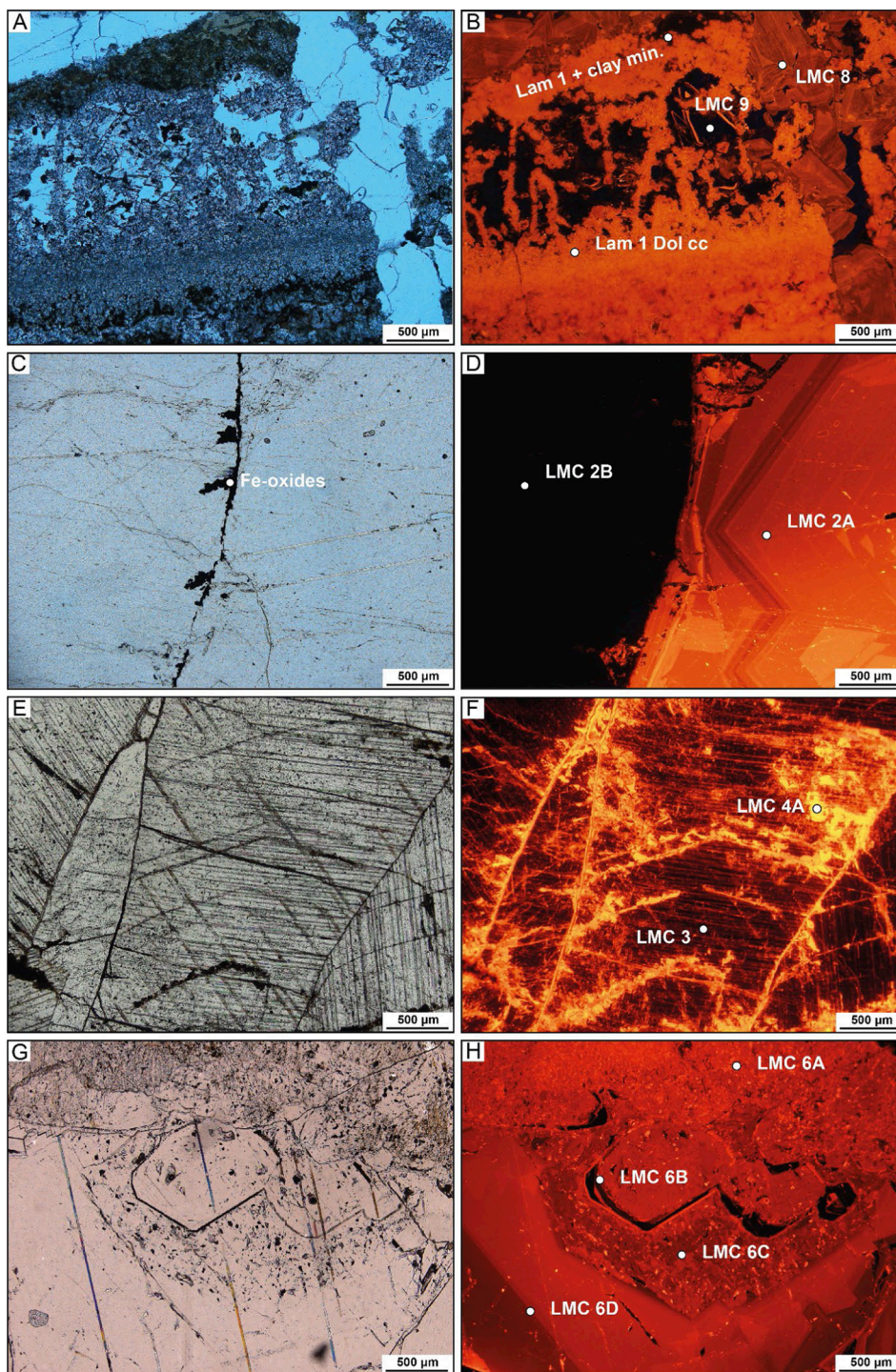


Fig. 6. Transmitted light and corresponding cathodoluminescence images of the Post-Variscan fault zone and paragenetically younger related carbonates in the Steltenberg Quarry. (A, B) Patchy red to bright orange luminescent dolomite cements form Laminites 1. The darker layers (A) contain up to 30 vol% of clay minerals, whereas cavities in the clear layers are often filled with meteoric dark blue to yellow luminescent LMC 9. Note that the dolomite cements are cut by a zoned red luminescent LMC 8 vein. (C, D) Zoned, bright red to bright orange luminescent LMC 2A is concordantly overgrown by non-luminescent LMC 2B. Macroscopically and in transmitted light, there is no difference between both sub-phases. Dendritic Fe-oxides developed along the grain boundary between both phases. (E, F) Primary dark red luminescent radial LMC 3 crystals show stepwise skeletal crystal growth. Along the crystal boundary, LMC 4A overprinted the structure. (G, H) The phases LMC 6A-D occur in vein swarms, which cross-cut all paragenetically older phases in places. LMC 6A and 6C are patchy pale red to bright orange luminescent and rich in inclusions, whereas LMC 6B is non-luminescent to yellow. These sub-phases are overgrown by red to orange luminescent LMC 6D.

quartz crystals, reflecting the growth from old to young. Spatial intervals between the single ablation spots are $\sim 50 \mu\text{m}$.

4. Results

4.1. Cement stratigraphy

Geochemical proxy data not placed into a rigorous petrographic

framework are difficult to interpret. Hence, a paragenetic succession of the carbonates in the Steltenberg Quarry was established from field observations (Figs. 2, 3), thin section data ($n = 127$), and cathodoluminescence analysis (Figs. 4-6; Table 1). We complement the initial data on the complex paragenetic sequence presented in Pederson et al. (2021) with new data. The dolomite terminology applied follows Sibley and Gregg (1987). A detailed paragenetic phase description and additional cathodoluminescence images on all phases are given in the

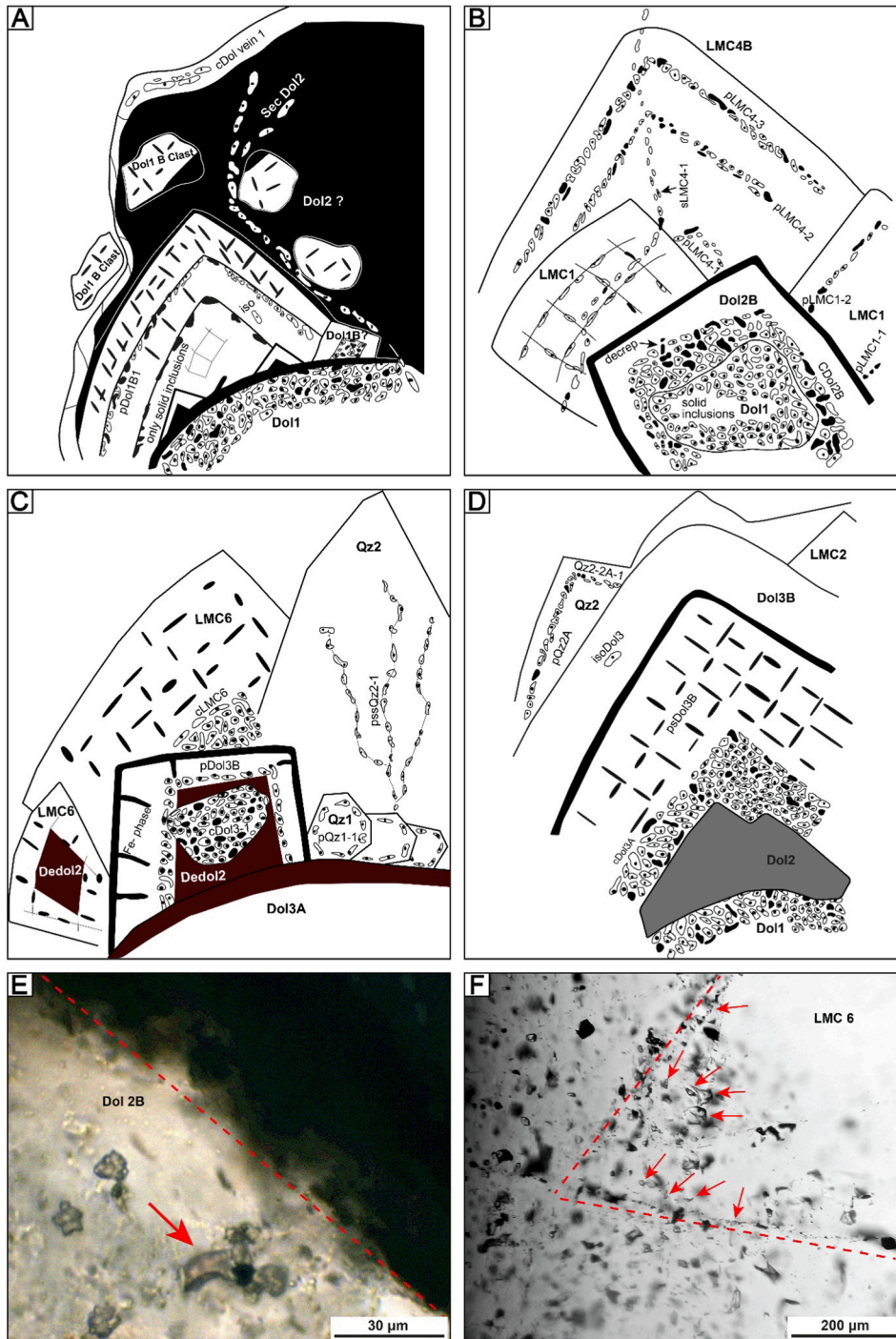


Fig. 7. Schematic petrography of fluid inclusion assemblages at Steltenberg Quarry. (A, B) Phase assemblage genetically related to the Variscan hydrothermal activity. Note that LMC 6 is genetically related to the Post-Variscan fault zone, which overprinted the Variscan mineralisation in places. (C) Phase assemblage genetically related to the Post-Variscan fault zone hydrothermal activity. (D) In places, fluids from the Post-Variscan fault zone overprinted the genetically older dolomite phases. This leads to partial recrystallisation of older cement generations; hence, these often form the core of overgrown dolomite crystals. (E, F) Exemplary transmitted light images with a 50 x magnification of fluid inclusions in (E) Dol 2B and (F) LMC 6. Due to the birefringence in carbonates, the image quality is limited. The red arrows denote measurable fluid inclusions.

digital supplement S1.

4.2. Micro XRF data

Micro-XRF maps of all relevant key samples (thin sections) were generated to obtain an appropriate preparation for further analyses on a micrometre scale. In general, element distributions were examined to characterise the corresponding presence of certain elements in whole rock samples and their distribution in certain mineral phases. The abundance and distribution of different geochemical phases were quantified using their distinct chemical variations (fingerprints). This approach enabled us to identify the best samples subsequently studied through further geochemical methods. In this respect, micro scale XRF analyses defined clear differences in Mn (and partially Fe) contents of carbonates, which is used to identify (in combination with cathodoluminescence microscopy and general petrography) eight generations of carbonate phases in the analyzed samples. These groups include MK-fossils (crinoid fragments; Fig. 8A), Dolomite 1A, 1B (saddle dolomite cement), 2A (matrix dolomite), laminite (Lam) 1 (dolomite cement), LMC 4B, 7 and 8. To highlight (and mark for further analyses) the compositional differences we used Mn intensity maps (blue indicates low, red colour high concentrations of Mn; Fig. 8A, 9C,E) and Fe distribution maps (green, Fig. 8C). Crinoid fragments typically show the complete absence of Mn and Fe, which separates them from Dol 1A. Furthermore, Mn concentrations generally increase from Dol 1B < Dol 1A < LMC 4B < LMC 7 < Dol 2A, with Dol 1A showing the highest Fe contents (Fig. 8C).

4.3. Fluid inclusion data

A detailed fluid-inclusion petrography is required to decipher the fluid evolution of a hydrothermal system. This task was performed using transmitted light microscopy (Fig. 7; Goldstein and Reynolds, 1994; Walter et al., 2015). It was possible to gather data from primary, pseudo-secondary, and isolated inclusions (n = 215 fluid inclusions in 55 fluid inclusion assemblages, FIA) in quartz and carbonate phases. A summary of the most important fluid inclusion data is given in Table 2. The full microthermometric dataset is given in the digital supplement S1. Please note: not all diagenetic phases in this study contained measurable fluid inclusions.

4.4. Crush leach data

The crush leach data of the various cement phases (n = 20) are shown in Table 3. Here, only the most relevant aspects are presented. There is no systematic paragenetic trend. Cl/Br ratios range from low 9 (Qz 2) to 175 (Dol 2B). The Cl/J ratios are clustering between 7 (MK limestone) and 372 (Dol 2B) with few outliers at 3,618 (LMC 6), 2,662 (Dol 3B), 691 (Dol 3B), and 619 (Dol 3A). The Rb/Cs ratios show strong variations between 3.9 and 82.6.

4.5. Carbon, oxygen and strontium isotope geochemistry

Carbon and oxygen isotope values and $^{87}\text{Sr}/^{86}\text{Sr}$ ratios for all drilled cement phases are given in Table 2; only the most important features are reported. Detailed tables, including (i) major and trace element concentrations, (ii) $\delta^{13}\text{C}$ and $\delta^{18}\text{O}$ range, and $^{87}\text{Sr}/^{86}\text{Sr}$ ratios in sample groups, are given in the digital supplement S1. The $\delta^{18}\text{O}$ values of 180 powder samples range from -13.9‰ (LMC 1) to -0.4‰ (Laminite 1), independent of mineralogy and age of formation. The $\delta^{13}\text{C}$ values of all 180 powder samples range from -7.4‰ (Dedol 2) to $+4.6\text{‰}$ (Dol 3B). The strontium isotope ratios (n = 38, Table 2) range between 0.707915 ± 0.000005 (pristine brachiopod shell) and 0.714721 ± 0.000006 (Laminite 1). The phases LMC 4A and LMC 5A were not drillable due to their small size.

4.6. Clumped isotope thermometry

A summary of the carbonate-clumped isotope results (n = 20) is presented in Table 3. Errors in temperatures are $\pm 1\sigma$ of the replicates. The clumped isotope temperature of the MK limestone precursor is $85 \pm 41\text{ °C}$. The dolomite temperatures range from $90 \pm 38\text{ °C}$ (Dol 2A) to $181 \pm 13\text{ °C}$ (Dol 1B). Dol 1A ($124 \pm 5\text{ °C}$), Dol 2B ($146 \pm 21\text{ °C}$), Dol 3A (130 ± 23), and Dol 3B ($133 \pm 34\text{ °C}$) plot within this range. The Laminite 1 phases range from $80 \pm 22\text{ °C}$ (Lam 1 Dol cc) to $106 \pm 14\text{ °C}$ (Lam 1 clayey dolo-packstone). Compared to the dolomite phases, the Dedol 2 temperature is significantly lower ($27 \pm 11\text{ °C}$). The low Mg calcites display a very variable temperature range, with temperatures as low as $23 \pm 8\text{ °C}$ (LMC 9) up to $227 \pm 17\text{ °C}$ (LMC 1). The remaining calcite phases LMC 2 ($48 \pm 4\text{ °C}$), LMC 3 ($57 \pm 28\text{ °C}$), LMC 4B ($102 \pm 8\text{ °C}$), LMC 5 ($81 \pm 30\text{ °C}$), LMC 6 ($78 \pm 14\text{ °C}$), LMC 7 ($50 \pm 1\text{ °C}$), and LMC 8 ($73 \pm 1\text{ °C}$) plot within this range. The full dataset is available in the digital supplement S1.

4.7. U-Pb dating

Dolomite phases range in $^{207}\text{Pb}/^{206}\text{Pb}$ values from 0.100 to 0.873 and $^{238}\text{U}/^{206}\text{Pb}$ values from 0.089 to 35.954. The Tera-Wasserburg diagram results in lower intercept ages of $388.8 \pm 4.9/5.8\text{ Ma}$ to $30.0 \pm 2.80/2.81\text{ Ma}$ (Figs. 8, 9, Table 2). Based on micro XRF, cathodoluminescence and transmitted light microscopy, no evidence of uranium minerals was recognised in any samples. The U-Pb dolomite ages record mineralisation and recrystallisation between the Middle/Late Devonian and the Oligocene. The ages of some phases (Dol 1A/B, Dol 2A/B, Laminite 1/LMC 2, LMC 5/LMC 7) overlap so that their age was constrained by cathodoluminescence microscopy and cross-cutting relationships or paragenetic overgrowth in the field. Cement phases LMC 1, Dol 3A/B, LMC 3, LMC 6, LMC 9 and LMC 10 were not datable due to low U ($\ll 10^4\text{ cps}$) concentration and too high Pb ($\gg 10^6\text{ cps}$) concentration, respectively.

4.8. Trace elemental data

Trace elemental concentrations in quartz show two types of patterns (Table 4). Pattern 1 is observed in Quartz 1, whereas pattern 2 is related to quartz 2 and 3. Pattern 1 shows an asymmetric enrichment of the different trace elements during crystal growth, whereas quartz 2 and 3 show a rhythmic scatter, whereas all trace elements are enriched together and depleted in individual zones (see Fig. 10).

5. Interpretation and Discussion

In the following, we document and discuss the chain of diagenetic events that shaped these carbonates and their proxy data from their Givetian-Frasnian (387.7–372.2 Ma) deposition to Oligocene-Recent meteoric karstification.

5.1. Paragenetic succession

The complex paragenetic succession of Massenalk limestones in the Steltenberg Quarry is composed of bulk limestones (mud-, wacke-, floatstones; $\Delta_{47} = 85 \pm 41\text{ °C}$; U-Pb age = $388.8 \pm 4.9/5.8\text{ Ma}$, Table 2) and includes marine and burial cement phases (Fig. 4A, B, 11; 12A, E). These include burial dolo-grainstones (Dol 1) consisting of matrix dolomite (Dol 1A; $\Delta_{47} = 124 \pm 5\text{ °C}$; U-Pb age = $381.4 \pm 21.8/22.0\text{ Ma}$, Table 2, Fig. 4C, D) and a void-filling saddle dolomite cement phase (Dol 1B; $\Delta_{47} = 181 \pm 13\text{ °C}$; U-Pb age = $384.2 \pm 4.7/5.6\text{ Ma}$, Table 2, Fig. 4C, D).

The partially dolomitised limestones experienced several subsequent fault-induced hydrothermal (de-) dolomitisation events. The first events were triggered by folding and faulting during the Variscan Orogeny (Fig. 11; 12B, F; Gillhaus et al., 2003). Side strands of the neighbouring

Table 2

Summary of the geochemical and paleothermometrical characteristics in the paragenetic sequence (starting at the bottom with precursor MK limestone and ending with LMC 10 at the top) of the Steltenberg Quarry including their carbon-isotope, oxygen-isotope and strontium-isotope composition, clumped isotope temperature, primary fluid inclusion homogenisation temperatures, fluid salinities, fluid densities, and the U-Pb age (if applicable). Additional geochemical data, the full clumped-isotope and fluid-inclusion datasets for all analysed samples are provided in the digital supplement S1.

Phase	$\delta^{13}\text{C}$ (‰)			$\delta^{18}\text{O}$ (‰)			$^{87}\text{Sr}/^{86}\text{Sr}$ ($\pm 2\sigma$)		Δ_{47} ($^{\circ}\text{C}$) ($\pm\text{SD}$)	Primary T_{h} uncorr. ($^{\circ}\text{C}$) ($\pm\text{SD}$)	Fluid salinity (wt-% NaCl+CaCl ₂)	Fluid density (g/cm ³) ($\pm\text{SD}$)	U-Pb age (Ma) ($\pm\text{SD}$)
	min.	max.	mean	min.	max.	mean	min.	max.					
LMC 10	-6.4	-5.6	-6.0	-9.2	-7.5	-8.2	No data	No data	No data	No data	No data	No data	No data
LMC 9	-5.3	-3.6	-4.3	-5.8	-5.0	-5.4	0.709386 (5)	0.709386 (5)	23 (8)	No data	No data	No data	No data
LMC 8	-2.9	-1.5	-2.2	-3.8	-3.4	-3.6	0.711656 (5)	0.711656 (5)	73 (1)	180 (14)	16.2 (0.7)	1.01 (0.02)	30.0 (2.80/2.81)
LMC 7	-0.4	2.6	1.5	-7.5	-5.9	-6.4	0.709161 (5)	0.709506 (5)	50 (1)	127 (3)	17.4 (0.6)	1.06 (0.01)	60.5 (9.57/9.58)
LMC 6	-0.1	2.3	1.7	-6.4	-5.3	-5.9	0.708658 (5)	0.709306 (5)	78 (14)	Domain 2: 178 (13) Domain 1: 57 (2)	16.3 (1.1) 18.5 (1.0)	1.01 (0.02) 1.12 (0.01)	No data
LMC 5B	-0.7	2.1	0.5	-6.9	-5.4	-6.3	0.711526 (5)	0.713170 (5)	81 (30)	88 (3)	25.5 (0.6)	1.16 (0.01)	5B: 63.85 (5.62/5.64)
LMC 5A	No data			No data			No data	No data	No data	No data	No data	No data	5A: 60.81 (6.02/6.04)
Dedol 3	No data			No data			No data	No data	No data	No data	No data	No data	No data
LMC 4B	1.1	1.3	1.2	-8.7	-8.5	-8.6	0.712528 (5)	0.712528 (5)	102 (8)	124 (4)	5.5 (0.3)	0.98 (0)	95.02 (2.59/2.70)
LMC 4A	No data			No data			No data	No data	No data	No data	No data	No data	125.6 (8.6/8.4)
Sulphides	Not applicable			Not applicable			Not applicable		Not app.	No data	No data	No data	No data
Qz 2	Not applicable			Not applicable			Not applicable		Not app.	104 (11)	22.4 (1.1)	1.13 (0.02)	No data
Qz 1	Not applicable			Not applicable			Not applicable		Not app.	No data	No data	No data	No data
LMC 3	0.4	2.7	1.5	-9.8	-6.0	-7.5	0.710094 (5)	0.710094 (5)	57 (21)	86 (5)	Bim. distr.: 23.1 (0.5); 5.8 (1.3)	Bim. Distr.: 1.14 (0.01); 0.99 (0.03)	No data
Fe-oxides	Not applicable			Not applicable			Not applicable		Not app.	No data	No data	No data	No data
Dedol 2	-7.4	-1.9	-5.1	-6.7	-4.2	-5.6	0.709761 (5)	0.709934 (6)	27 (11)	126 (3)	11.3 (2.8)	1.02 (0.02)	No data
Dol 3B	-1.3	4.6	1.5	-7.0	-3.4	-5.7	0.708626 (5)	0.709064 (4)	133 (34)	131 (24)	21.6 (0.9)	1.09 (0.01)	No data
Dol 3A	3.2	3.8	3.5	-7.2	-7.0	-7.1	0.708565 (5)	0.708574 (5)	130 (23)	96 (15)	22.7 (0.5)	1.12 (0)	No data
LMC 2	-3.1	-2.5	-2.8	-6.4	-5.8	-6.2	0.711326 (5)	0.711326 (5)	48 (4)	No data	No data	No data	254.1 (3.9/4.4)
Lam 1 cl. dol.	-3.0	-2.8	-2.9	-2.0	-0.4	-1.1	0.714721 (6)	0.714721 (6)	106 (14)	No data	No data	No data	No data
Lam 1 dol cc	-2.9	-2.1	-2.4	-4.5	-2.1	-3.6	0.709028 (5)	0.709028 (5)	80 (22)	214 (5)	4.3 (1.2)	0.96 (0.01)	252.4 (8.5/8.7)
LMC 1	1.3	2.2	1.8	-13.9	-8.4	-11.4	0.708757 (5)	0.709314 (5)	227 (17)	209 (9)	16.6 (1.3)	0.99 (0)	No data
Dedol 1	-3.3	0.5	-1.8	-7.3	-5.5	-6.2	0.709334 (4)	0.709334 (4)	No data	No data	No data	No data	No data
Dol 2B	2.2	3.7	3.1	-9.8	-5.4	-8.4	0.708861 (5)	0.709524 (5)	146 (21)	108 (7)	21.7 (0.7)	1.12 (0.01)	339.3 (24.9/25.4)
Dol 2A	1.4	3.8	3.1	-9.0	-6.6	-7.6	0.709236 (5)	0.709786 (5)	90 (38)	112 (16)	22.9 (2.1)	1.13 (0.03)	343.9 (19.9/20.0)
Dol 1B	3.5	3.7	3.6	-10.1	-8.2	-9.2	0.708870 (5)	0.708870 (5)	181 (13)	111 (10)	21.5 (1.8)	1.11 (0.02)	384.2 (4.7/5.6)
Dol 1A	3.4	3.9	3.7	-9.5	-4.5	-6.7	0.709655 (5)	0.710021 (5)	124 (5)	40 (0)	6.6 (1.2)	1.04 (0)	381.4 (21.8/22.0)
MK Fossils	2.8	3.0	2.8	-7.7	-7.1	-7.3	0.707915 (5)	0.707915 (5)	No data	No data	No data	No data	388.8 (4.9/5.8)

(continued on next page)

Table 2 (continued)

Phase	$\delta^{13}\text{C}$ (‰)			$\delta^{18}\text{O}$ (‰)			$^{87}\text{Sr}/^{86}\text{Sr}$ ($\pm 2\sigma$)		Δ_{47} (°C) (\pm SD)	Primary T_h uncorr. (°C) (\pm SD)	Fluid salinity (wt-% NaCl+CaCl ₂)	Fluid density (g/cm ³) (\pm SD)	U-Pb age (Ma) (\pm SD)
	min.	max.	mean	min.	max.	mean	min.	max.					
MK limestone matrix	2.4	3.2	2.8	-9.9	-5.2	-7.1	0.708027 (5)	0.708879 (5)	85 (41)	No data	No data	No data	No data

WSW-ENE-striking regional Variscan thrust served as pathways for hydrothermal fluids causing corrosion and later dissolution-precipitation. These resulted in the formation of a second dolomite phase Dol 2 consisting of matrix dolomite (Dol 2A; $\Delta_{47} = 90 \pm 38$ °C; U-Pb age = $343.9 \pm 19.9/20.0$ Ma, Table 2, Fig. 4E, F) and a void-filling saddle dolomite cement phase (Dol 2B; $\Delta_{47} = 146 \pm 21$ °C; U-Pb age = $339.3 \pm 24.9/25.4$ Ma, Table 2, Fig. 4G, H). Breccia clasts in Dol 2B veins suggest precipitation during fracture opening. The reactivation of earlier formed Variscan faults in the Permian (Götte, 2004) resulted in the precipitation of high-temperature LMC 1 ($\Delta_{47} = 227 \pm 17$ °C, Table 2, Fig. 4G, H). Dedolomitised breccia clasts in this phase and corroded, dedolomitised surfaces of Variscan dolomites (Dedol 1) indicate a first dedolomitisation interval induced by this hydrothermal calcite (Fig. S1.1 digital supplement) (Fig. 12)

A rotation of the compressive stress field marked the end of Variscan Orogeny and resulted in the development of the NNW-SSE-trending Post-Variscan fault zone and, hence, the later initiation of a third hydrothermal dissolution-precipitation phase around the Permian-Triassic boundary (Fig. 11; 12C, G). Near this fault system, metre- to tens of metre-sized hypogenic karst cavities occur within the dolomitised intervals (Fig. 3G; Drozdowski et al., 2017; Mueller et al., 2023). These were filled by laminated dolostones (Laminite 1; Fig. 6A, B, 11; 13) consisting of bedded ABAB sequences of dolomite cement ($\Delta_{47} = 80 \pm 22$ °C; U-Pb age = $252.4 \pm 8.5/8.7$ Ma, Table 2) and clayey dolograins ($\Delta_{47} = 106 \pm 14$ °C, Table 2). These laminites are generally associated with LMC 2 ($\Delta_{47} = 48 \pm 4$ °C; U-Pb age = $254.1 \pm 3.9/4.4$ Ma, Table 2, Fig. 6C, D) in layers within the Laminite 1. LMC 2 also occurs in up to ~ 15 m-sized NNW-SSE-trending veins (Fig. 2D). The dolomite Dol 3 consists of a matrix dolomite (Dol 3A; $\Delta_{47} = 130 \pm 23$ °C, Table 2, Fig. 5A-D) and a void-filling saddle dolomite cement phase (Dol 3B; $\Delta_{47} = 133 \pm 34$ °C, Table 2, Fig. 5E, F). Another dedolomitisation phase (Dedol 2; $\Delta_{47} = 27 \pm 11$ °C, Table 2, Fig. 5G, H) may be triggered by hypogenic karstification and/or corrosive meteoric fluid. Renewed tectonic activity in the Mesozoic caused brecciation of Post-Variscan fault zone-associated phases and arguably rapid cementation by calcite cement (LMC 3; $\Delta_{47} = 57 \pm 21$ °C, Table 2, Fig. 6E, F). This LMC 3 is occasionally overgrown by Dol 3, indicating multiphase fluid pulses precipitating Dol 3 during the Mesozoic (Fig. 11). In places, quartz (Qz 1/2; $T_h = 104 \pm 11$ °C, Table 2, Fig. 5G, H) and sulphide cementation occurred during the Late Triassic to Early Cretaceous (Schaeffer, 1984; Götte, 2004 and references therein). Along grain boundaries a microcrystalline phase LMC 4A (U-Pb age = $125.6 \pm 8.2/8.4$ Ma, Table 2; Fig. 4H, 6F) altered older phases indicating a renewed fluid pulse in the Early Cretaceous. In places LMC 4A is overgrown by calcite cement (LMC 4B; $\Delta_{47} = 102 \pm 8$ °C; U-Pb age = $95.02 \pm 2.59/2.70$ Ma, Table 2), which indicates another Post-Variscan fault zone –associated hydrothermal activity phase in the Late Cretaceous.

An Alpine vein set cross-cuts both fault zones (Fig. 2A; 11; 12D, H)). These consist of Late Cretaceous-Early Paleogene hydrothermal calcite cement LMC 5 ($\Delta_{47} = 81 \pm 30$ °C; U-Pb age = $60.81 \pm 6.02/6.04$ Ma; $63.85 \pm 5.62/5.64$ My, Table 2, Fig. 5B), LMC 6 ($\Delta_{47} = 78 \pm 14$ °C, Table 2, Fig. 6G, H), and LMC 7 ($\Delta_{47} = 50 \pm 1$ °C; U-Pb age = $60.5 \pm 9.57/9.58$ Ma, Table 2). In places, this cement surrounds breccia clasts, indicating that renewed tectonism around the Cretaceous-Paleogene boundary mobilised the hydrothermal fluids and induced precipitation. Corrosive fluid circulation before the calcite cement precipitation

caused renewed hypogenic karstification in vugs on top of older dolomite phases. This resulted in a third dedolomitisation phase (Dedol 3). In places, breccia clasts are surrounded by the youngest hydrothermal calcite phase (LMC 8; $\Delta_{47} = 73 \pm 1$ °C; U-Pb age = $30.0 \pm 2.80/2.81$ Ma, Table 2, Fig. 6A, B), indicating renewed late Paleogene tectonic activity within the Post-Variscan fault zone (Fig. 13). All hydrothermal dolomite and calcite phases are often (partially) covered by meteoric calcite phases (LMC 9; $\Delta_{47} = 23 \pm 8$ °C, Table 2). Throughout the Steltenberg Quarry, surface karstification is a prominent feature (Fig. 3H). These surfaces are covered by botryoidal meteoric LMC 10 in places. In the following, this paragenetic succession is discussed in its temporal context.

5.2. Evolution of a complex carbonate archive

5.2.1. Protolith deposition and early to intermediate burial diagenesis

The Massenkalk limestone precursor carbonates were deposited at the shelf edge and open shelf in a shallow marine carbonate factory south of the Old Red continent (Krebs, 1974). Well-preserved features of the depositional facies include well-preserved brachiopod shells, echinoderm fragments and marine cement types (dog-tooth, radialial fibrous calcites; Fig. 3B, 4A, B, 12E, F; Götte, 2004). Carbon isotope values of the host limestone are within the range of their Middle/Late Devonian marine seawater values (ca -0.6 to 3.2 ‰; Fig. 14). In contrast, oxygen isotope ($\delta^{18}\text{O}$) data of the host limestone were shifted towards more negative values (-9.9 to -5.2 ‰; cf. Middle/Late Devonian marine fluids are in the range of -6 to -2.7 ‰). Similarly, well-preserved carbon isotope values and somewhat more negative oxygen isotope values are present in brachiopod shells (Fig. 14). These values are comparable to well-preserved Middle/Late Devonian rocks elsewhere (Buggisch and Joachimski, 2006; Xiong et al., 2018; Cramer and Jarvis, 2020; Grossman and Joachimski, 2020). The strontium isotopic ratios of the host limestone and a well-preserved brachiopod shell show a marine signature (Fig. 15; McArthur et al., 2020). Other host limestone samples, however, tend towards slightly more radiogenic ratios (up to $^{87}\text{Sr}/^{86}\text{Sr}_{\text{MK limestone}} = 0.708879$). These may be explained by a certain low degree of deep burial fluid overprint or later hydrothermal overprint of subsequent diagenetic phases.

The elevated clumped-isotope Δ_{47} temperatures (Δ_{47} -temperature) indicate that the limestone matrix was reset, either by solid-state reordering or recrystallisation, during later burial stage ($\Delta_{47} = 85 \pm 41$ °C; Fig. 16). The Δ_{47} -temperature altered by solid-state reordering, defined as blocking temperature (Passey and Henkes, 2012; Stolper and Eiler, 2015), can be estimated based on the burial history (Fig. 20) and the reordering model (Fig. 17; Lloyd et al., 2018). According to Agemar et al. (2012), the geothermal gradient in the study area is between 30 and 35 °C/km. Assuming these geothermal gradients as endmember values, the reordering model from Lloyd et al. (2018) suggests a blocking temperature range from 150 to 200 °C, which is much higher than the measured Δ_{47} -temperature and thus rejects the reordering origin. The lowered $\delta^{18}\text{O}$ values with invariant $\delta^{13}\text{C}$ values and elevated Δ_{47} -temperatures point to the closed-system recrystallisation in the burial stage. This observation is strengthened by patchy bright red cathodoluminescence (Fig. 4B). Additionally, depleted $\delta^{18}\text{O}$ values could be related to early meteoric fluid (*sensu* Lohmann, 1988); meteoric vadose or phreatic textures, however, are lacking. The U-Pb ages of

Table 3
Summary of crush leach data of carbonate and quartz phases from Steltenberg Quarry.

Sample	Paragenetic phase	¹³³ Cs											
		F	Cl	Br	NO ₃	SO ₄	I	⁸⁵ Rb	($\mu\text{g/l}$)	Cl/Br	Rb/Cs	Na/K	
HKW8-6-Ch1	LMC 7	0.003	0.429	0.005	0.255	0.055	0.025	0.83	0.09	86	17	9.21	3.81
HKW8-5-Ch3	LMC 9	0.006	0.203	0.008	0.196	0.041	0.007	0.16	0.01	25	29	13.10	1.57
HKW8-5-Ch2	LMC 7	0.005	2.450	0.015	0.045	0.133	0.011	0.14	0.02	163	223	8.21	9.13
HKW8-5-Ch1	LMC 5	0.008	14.474	0.155	0.048	0.670	0.004	0.64	0.09	93	3618	7.15	9.83
HKW8-4-Ch1	LMC 5	0.012	0.783	0.010	0.065	0.168	0.016	0.16	0.02	78	49	6.89	2.94
HKW8-3-Ch1	LMC 2	0	16.331	0.170	0.047	0.198	0.000	1.03	0.30	96	0	3.47	10.85
HKW5-MKHD-F-7-Ch1	Dol 3A	0.062	31.561	0.482	0.068	0.615	0.051	1.36	0.11	65	619	12.25	5.82
HKW5-MK-S-2-Ch1	MK limestone	0.453	0.949	0.014	0.164	11.341	0.142	6.78	0.59	68	7	11.54	0.21
HKW5-61-Ch2	Dol 1A	0.133	15.130	0.191	0.075	4.229	0.074	5.83	0.72	79	204	8.15	1.32
HKW5-61-Ch1	Dol 1B	0.045	6.322	0.053	0.054	0.666	0.017	1.02	0.10	119	372	10.69	3.39
HKW5-63-Ch2	Dol 2B	0.043	5.965	0.034	0.252	0.354	0.025	1.95	0.02	175	239	82.64	2.46
HKW8-7-Ch1	Qz 2	0.03	0.70	0.08	0.19	101.82	0.00	0.27	0.05	9	233	5.66	4.98
HKW5-66-Ch1	Qz 2	0.03	2.26	0.02	0.29	95.91	0.03	0.82	0.10	108	91	8.23	3.14
HKW5-63-Ch1	Dol 2A	0.085	16.978	0.248	0.185	0.506	0.067	0.65	0.03	68	253	25.65	7.82
HKW8-2-Ch1	Dedol 2	0.033	4.795	0.072	0.262	0.517	0.020	0.19	0.05	67	240	3.92	4.82
HKW8-1-Ch2	LMC 6	0.000	0.347	0.010	0.085	0.032	0.006	0.21	0.04	35	58	5.56	0.95
HKW8-1-Ch1	Dol 3B	0.024	39.929	0.741	0.186	0.649	0.015	1.58	0.41	54	2662	3.81	6.14
HKW5-HD-S-3,1-Ch1	Dol 3B	0.035	36.600	0.845	0.144	1.315	0.053	2.19	0.28	43	691	7.95	4.47
HKW5-MKHD-W-6-Ch2	LMC 4	0.012	7.827	0.079	0.139	0.265	0.031	0.60	0.03	99	252	17.28	5.22
HKW5-MKHD-W-6-Ch1	LMC 1	0.027	6.289	0.058	0.313	0.128	0.017	0.83	0.09	108	370	9.21	3.81

crinoid fragments suggest a late diagenetic stage of bioclast recrystallisation has not occurred (U-Pb age = $388.8 \pm 4.9/5.8$ Ma; Table 2).

5.2.2. Deep burial diagenesis and hot hydrothermal overprint

The $\delta^{13}\text{C}$ values of Dol 1A dolo-grainstone are moderately higher (Fig. 14) compared to Middle/Late Devonian marine values. This can be explained by mineralogy-dependent fractionation during dissolution-recrystallisation processes in the context of dolomitisation ($ca + 1$ ‰; Sheppard and Schwarcz, 1970; Swart, 2015). Therefore, they largely reflect a rock buffered $\delta^{13}\text{C}$ composition as known from other case examples of early diagenetic to hydrothermal dolomitisation (see discussion in Mueller et al., 2020; 2022a). In contrast, $\delta^{18}\text{O}$ values (-9.5 to -4.5 ‰) spread from Middle/Late Devonian marine values to lower ones. This dolomite phase may have been early marine diagenetic in origin and continued into the shallow burial (Udluft, 1929). This interpretation seems possible based on a few measurable isolated low-salinity fluid inclusions alone (Table 2, Fig. 18). Others, suggested dolomitisation along the lines of a modified mixing zone model during intermediate-to-deep burial in an early phase of Variscan Orogeny (Late Devonian; Gillhaus et al., 2003). These factors are in agreement with a partial resetting of $\delta^{18}\text{O}$ values, whereas $\delta^{13}\text{C}$ values remained conservative in a rock-buffered environment (Mueller et al., 2020). The bimodal $\delta^{18}\text{O}$ distribution within Dol 1A may be related to subsequent overprint by hot basin-derived fluids (Mueller et al., 2020 and references therein). Strontium isotope ratios (up to 0.710021) offer evidence for a basinal hydrothermal fluid component in Dol 1A, suggesting fluid interaction with continental crust (Fig. 15; Dickson, 1990; Moore and Wade, 2013). This interpretation is also supported by the patchy luminescence of Dol 1A (Fig. 4D), implying partial recrystallisation during subsequent burial. The U-Pb ages ($381.4 \pm 21.8/22.0$ Ma; Table 2) and clumped-isotope data ($\Delta_{47} = 124 \pm 5$ ‰; Fig. 16) support a burial diagenetic ripening and/or recrystallisation during early Variscan tectonism. With regard to the deep burial of these lithologies down to ca 6,500 m that continued to the onset of rapid uplift by Variscan Orogeny-driven compressional tectonism (Büker, 1996; Littke et al., 2000; Götze, 2004), Ostwald-type petrographic/geochemical ripening seems likely. The modelled blocking temperature, with a geothermal gradient of 30 to 35 °C/km, is between 100 to 150 °C and consistent with the measured Δ_{47} -temperature of Dol 1A within 95 % confidence limits (Figs. 16, 17). This may indicate that the temperature preserved in Dol 1 is the maximum burial temperature the succession experienced.

The void-filling saddle dolomite cement phase Dol 1B is characterised by comparable $\delta^{13}\text{C}$ and more negative $\delta^{18}\text{O}$ values similar to some of the Dol 1A samples (Fig. 14), indicating a potentially different burial diagenetic origin. Notably, the $^{87}\text{Sr}/^{86}\text{Sr}$ ratio of 0.708870 is less radiogenic than that of Dol 1A, which may point to a different strontium source in the parent fluid (Fig. 15). Saddle dolomites typically form during burial or from ascending hydrothermal fluids at formation temperatures between 50 and 320 °C (Liu et al., 2014; Peng et al., 2018; Mueller et al., 2022a; Immenhauser, 2022). Primary fluid inclusions in Dol 1B have high salinities and temperatures above 100 °C (Table 2; Fig. 18). Elevated fluid inclusion salinities around 20 wt-% are typical for basinal or continental basement brines (Frape et al., 1984).

The clumped-isotope temperature of Dol 1B points to an even higher temperature of the burial/hydrothermal formation fluids ($\Delta_{47} = 181 \pm 13$ ‰; Fig. 16) than estimated from the normal geothermal gradients (Fig. 17). The gap of ca 70 °C between primary fluid inclusion and clumped-isotope temperatures may be explained by the bulk analytical approach typical of clumped-isotope analysis averaging over several zonation/phases (see discussion in Mueller et al., 2022b). The precipitation of Dol 1B may have occurred after the partial recrystallisation of Dol 1A, as stylolites post-date recrystallisation, and are arguably coeval with the opening of voids and fractures in which saddle dolomite (Dol 1B) nucleated (Fig. 4C, D). The occurrence of Dol 1B in vein swarms points to precipitation during early-stage Variscan tectonism and ascension of deep-seated hydrothermal fluids (U-PB: $384.2 \pm 4.7/5.6$ Ma;

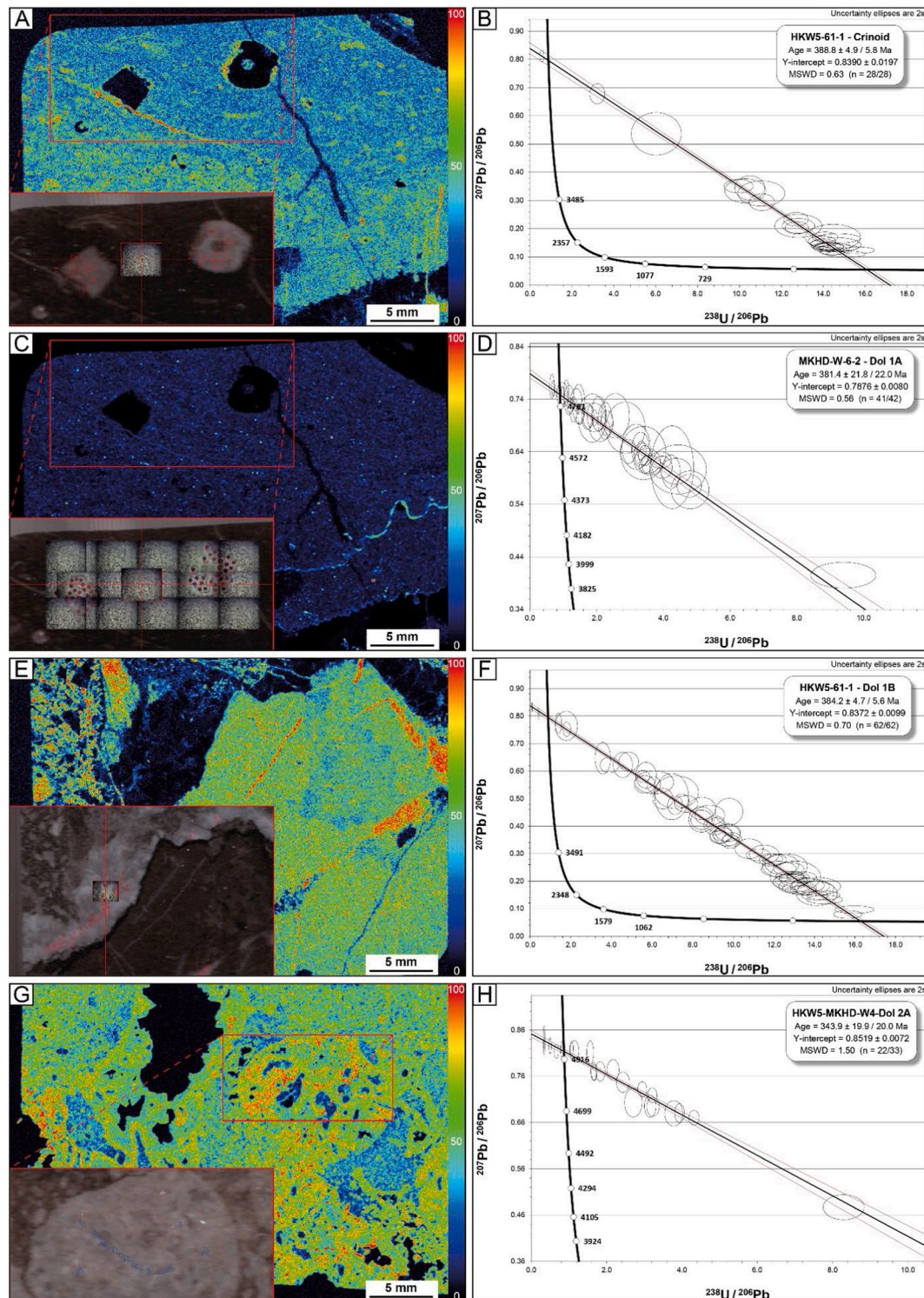


Fig. 8. Summary of U-Pb dating results for the key phases of this study. Additional data can be found in the digital supplement S1. (A, B) Micro XRF Mn intensity map (blue indicates low, red colour high concentration) and analysed area for MK fossils (crinoid fragments) placed against its Tera-Wasserburg diagram. (C, D) Micro XRF Fe content map (blue indicates low, red colour high concentration) and analysed area for Dol 1A placed against its Tera-Wasserburg diagram. (E, F) Micro XRF Mn intensity map (blue indicates low, red colour high concentration) and analysed area for Dol 1B saddle dolomite cement placed against its Tera-Wasserburg diagram. (G, H) Micro XRF Mn intensity map (blue indicates low, red colour high concentration) and analysed area for Dol 2A matrix dolomite placed against its Tera-Wasserburg diagram.

Table 2) as early as the Middle/Late Devonian.

5.2.3. Hydrothermal and tectonic overprint during the Variscan Orogeny

The Variscan Orogeny was driven by large-scale tectonic reorganisation and the collision of Gondwana and Laurussia during the

Devonian and Carboniferous. It caused folding and faulting and triggered fluid flow on a basin scale (Drozdowski and Wrede, 1994; Schulmann et al., 2014; Pastor-Galán et al., 2015; Franke et al., 2020). Variscan fluid flow events caused widespread precious metal, base metal and uranium mineralisation along the Variscan belt (including

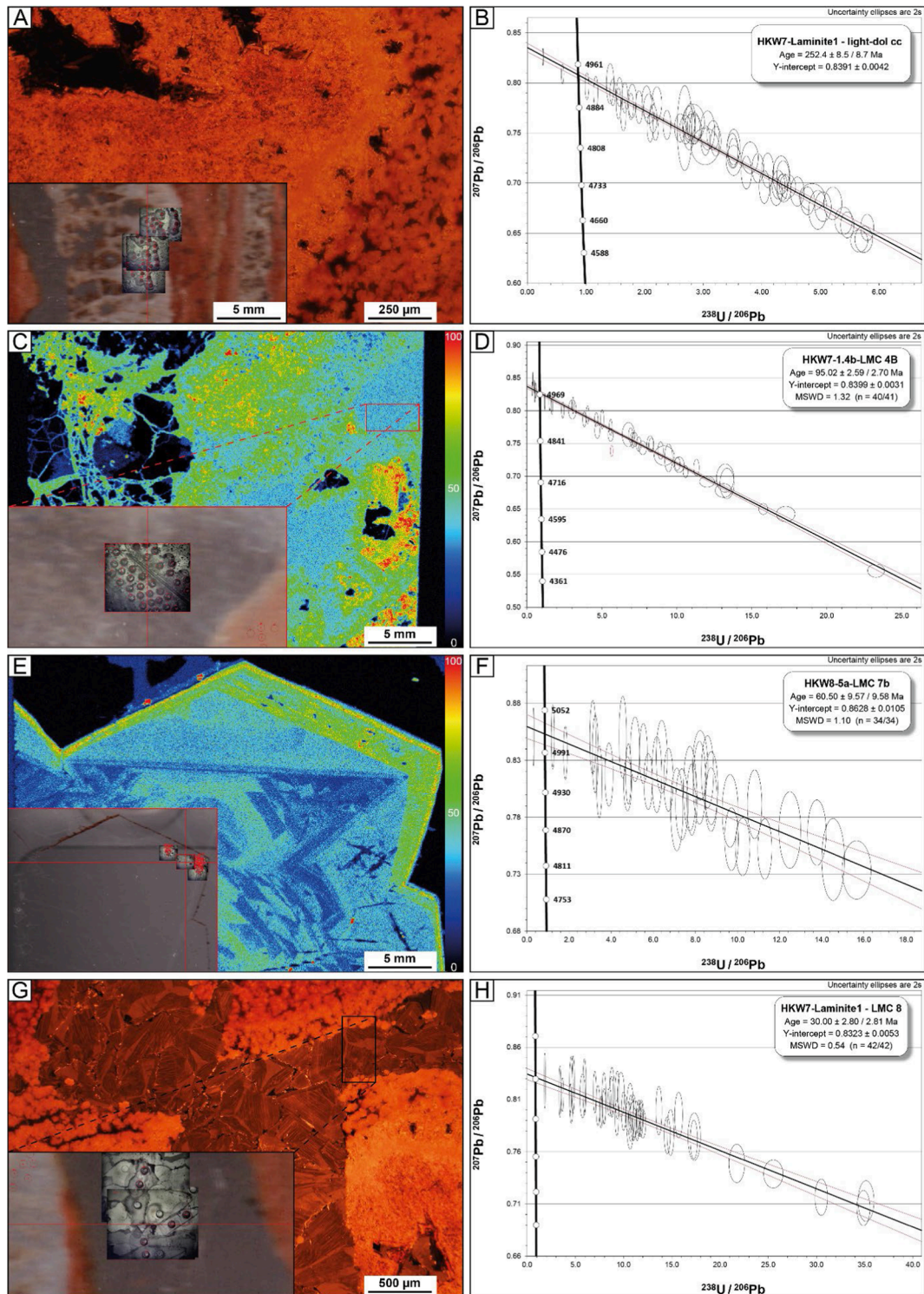


Fig. 9. Summary of U-Pb dating results for the key phases of this study. Additional data can be found in the digital supplement S1. (A, B) Cathodoluminescence image and analysed area for Laminite 1 dolomite cement placed against its Tera-Wasserburg diagram. (C, D) Micro XRF Mn intensity map (blue indicates low, red colour high concentration) and analysed area for LMC 4B placed against its Tera-Wasserburg diagram. (E, F) Micro XRF Mn intensity map (blue indicates low, red colour high concentration) and analysed area for LMC 7 placed against its Tera-Wasserburg diagram. (G, H) Cathodoluminescence image and analysed area for LMC 8 placed against its Tera-Wasserburg diagram.

carbonate minerals, e.g. [Hitzman et al., 1998](#); [Epp et al., 2019](#) and references therein), specifically also in the Rhenish Massif ([Nielsen et al., 1998](#); [Heijlen et al., 2001](#)). Within the Massenkalk carbonates in the northern Rhenish Massif, folding and faulting were accompanied by rapid uplift and erosion in the Late Carboniferous ([Littke et al., 2000](#)).

In the Steltenberg Quarry, the carbon and oxygen isotope values of Variscan fault zone-related dolomite phases Dol 2A, and saddle dolomite Dol 2B ([Fig. 14, Table 2](#)) are similar to those of Dol 1B ([Fig. 14, Table 2](#)). The $^{87}\text{Sr}/^{86}\text{Sr}$ ratios of Dol 2 are also comparable to Dol 1 ([Fig. 15, Table 2](#)). Moreover, the fluid inclusion temperatures and salinities of Dol

Table 4

Summary of trace elemental data of quartz phases Qz 1 to Qz 3 from Steltenberg Quarry.

Element	HKW-64-5 (Qz 1; ppm)			HKW8-7-b (Qz 2; ppm)			HKW8-QG1 (Qz 3; ppm)		
	Min.	Max.	Mean	Min.	Max.	Mean	Min.	Max.	Mean
Li7	0.10	361.15	95.38	0.10	54.18	4.98	0.10	763.62	47.31
Be9	0.00	0.73	0.18	0.00	0.13	0.04	0.00	204.42	12.70
B11	6.15	19.97	10.53	5.75	19.97	9.74	1.10	65595.95	2403.39
Na23	0.83	442.71	86.66	7.79	167.65	52.12	4.31	668978.06	25092.23
Al27	0.11	3788.65	604.39	0.21	265.48	26.75	1.15	14254.39	822.56
K39	1.36	325.95	23.98	0.83	42.92	9.10	0.29	24572.77	975.38
Ca44	37.83	57791.37	3254.66	30.37	51348.55	1167.23	36.69	1572938880.00	59700667.02
Ti48	0.01	28.16	1.57	0.00	23.51	0.60	0.01	795916.81	29841.64
Ti49	0.06	0.90	0.25	0.09	6.84	0.71	0.05	1233.81	71.62
Mn55	0.37	522.79	37.39	1.71	21.20	7.67	0.56	16125715.00	829262.30
Fe56	1.16	1343.92	100.33	0.63	3042.50	201.61	0.66	9998329.00	410437.97
Fe57	1.58	1586.77	148.57	1.29	4021.50	251.22	1.48	11860367.00	545038.44
Co59	0.03	0.53	0.11	0.02	0.09	0.05	0.03	416.00	31.17
Ni60	0.11	2.59	0.55	0.13	4.65	0.54	0.14	4738.00	227.40
Cu63	0.01	104.59	6.16	0.01	2.05	0.31	0.01	1764.03	85.69
Zn66	0.15	5.95	1.65	0.17	64.89	3.98	0.17	1236.78	98.66
Ga69	1.66	7.39	2.57	1.36	3.81	1.70	1.31	2078.61	69.34
Ge72	0.41	5.39	2.28	0.13	1.71	0.32	0.19	626.20	34.74
Rb85	0.00	1.17	0.08	0.01	0.05	0.01	0.00	39.24	2.65
Nb93	0.00	0.00	0.00	0.00	0.03	0.00	0.00	4.44	0.24
Mo95	0.00	0.22	0.03	0.01	0.09	0.02	0.01	5804.80	310.88
In115	0.00	0.01	0.00	0.00	0.01	0.00	0.00	11.84	0.91
Sn118	0.13	0.27	0.20	0.13	0.34	0.21	0.18	525.20	22.26
Sb121	0.50	20.21	6.08	0.02	12.39	1.53	0.08	945.71	17.72
W182	0.00	0.01	0.00	0.00	0.04	0.01	0.00	3.10	0.28
Au197	0.00	0.01	0.01	0.01	0.27	0.04	0.00	5.81	1.54
Pb208	0.00	0.22	0.05	0.01	2.83	0.43	0.01	110589.55	1681.81
Bi209	0.00	0.01	0.00	0.00	0.04	0.01	0.00	3.05	0.24
Te130	0.03	0.04	0.03	0.05	0.08	0.06	0.04	125.37	13.28

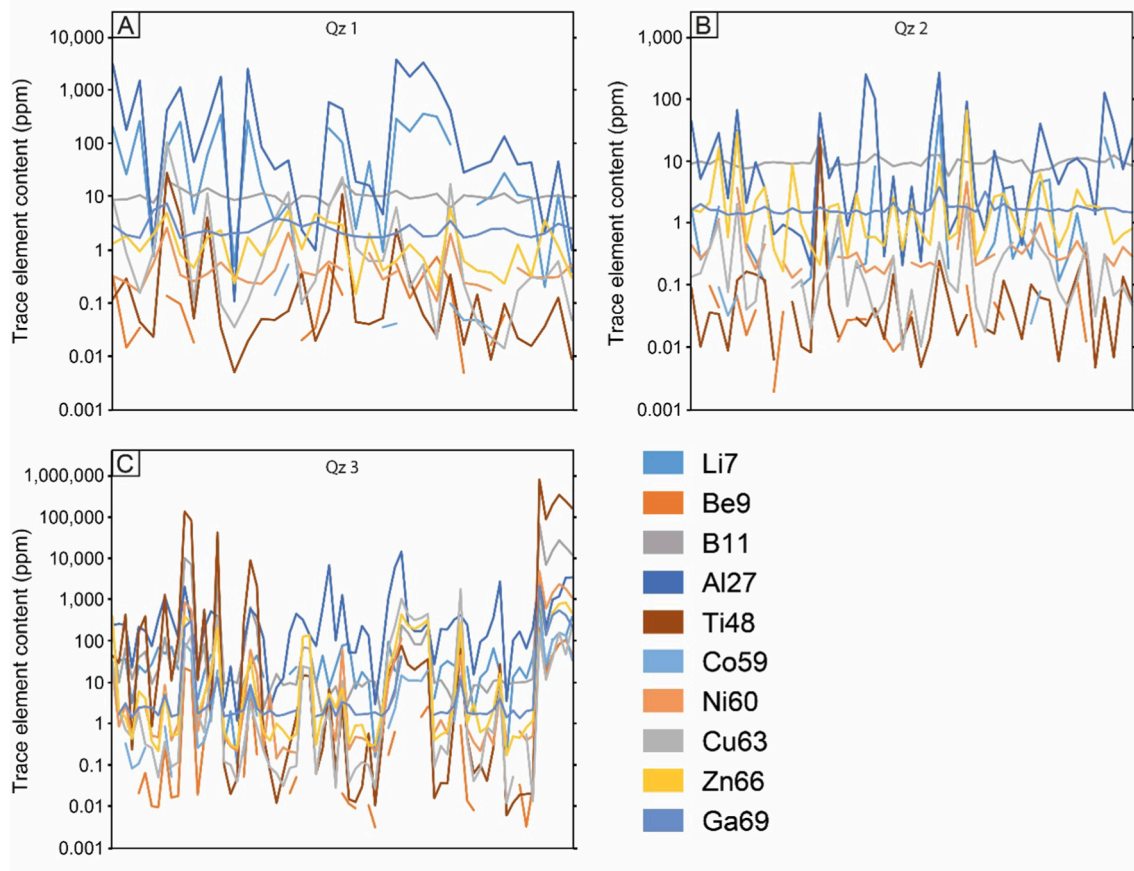


Fig. 10. In-situ trace element compositions of quartz phases 1, 2 and 3 derived from Steltenberg Quarry thin sections by laser ablation.

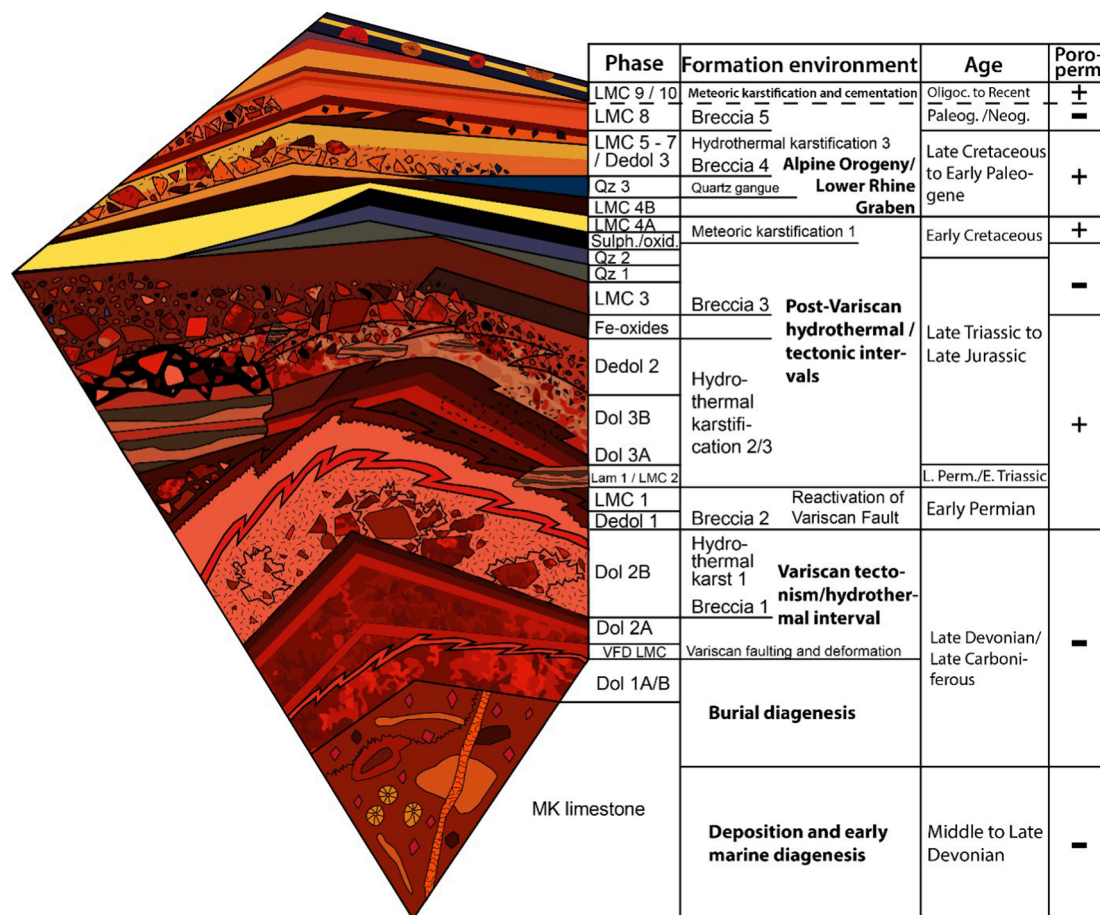


Fig. 11. Paragenetic sequence of all volumetrically significant diagenetic phases in the Steltenberg Quarry with typical cathodoluminescence colours related to their diagenetic and tectonic environment of precipitation or formation from deposition in the Devonian to subrecent karstification based on U-Pb dating in this study. The authors published a basic version of this paragenesis in Pederson et al. (2021), where some important diagenetic phases, including all phases U-Pb age were unknown. The tectonic activity phases and formation environments were compiled after Schaeffer (1984); Götte (2004); Drozdowski and Wrede (1994), and Sengör and Natal'in (2001). Modified from Pederson et al. (2021).

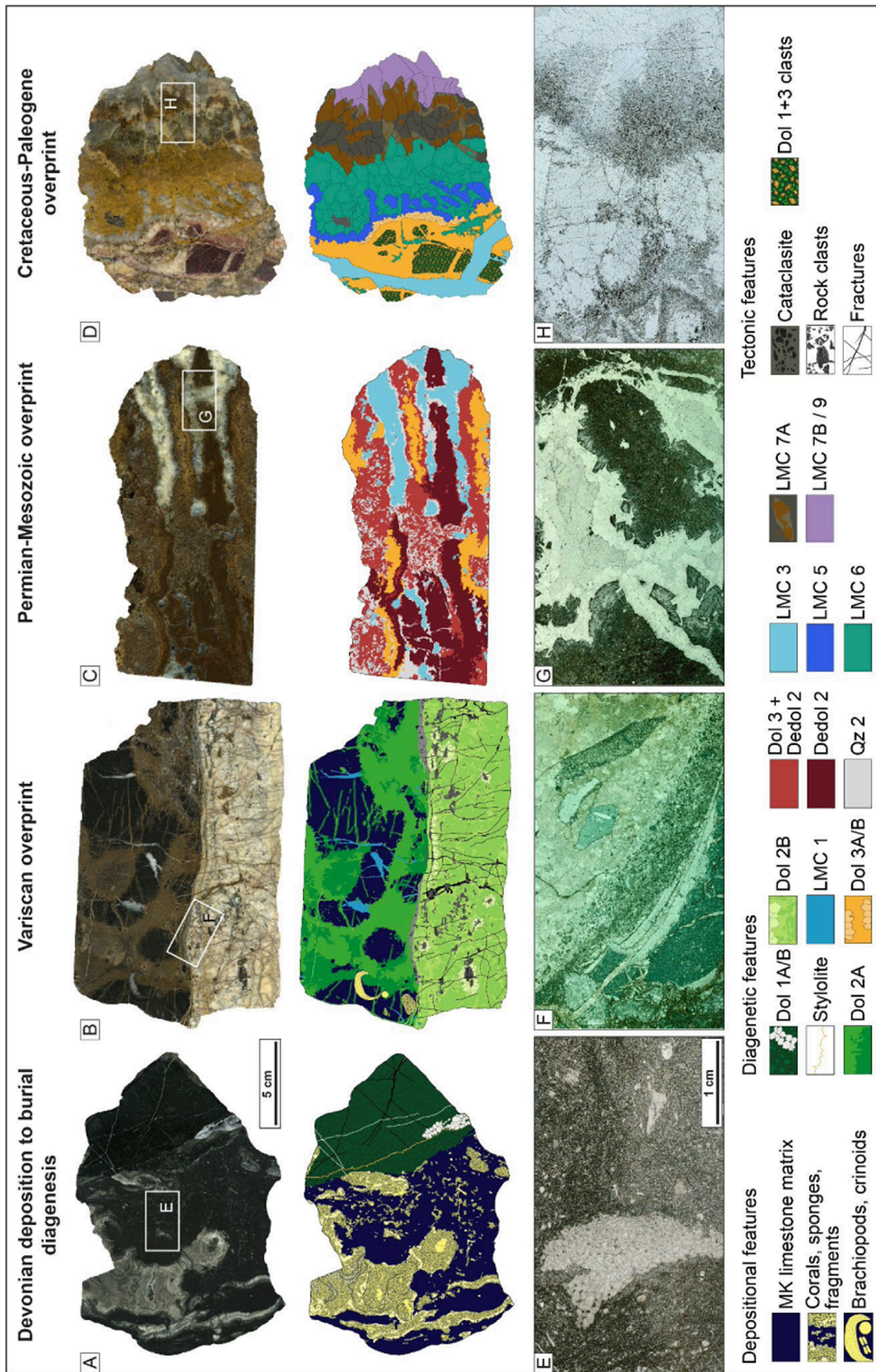
2A and 2B are comparable to those of Dol 1B, suggesting a similar origin (Figs. 16, 18, Table 2). Variscan hydrothermal dolomites from other basins share complementary geochemical and paleothermometrical properties (Boni et al., 2000; Gasparrini et al., 2006; Vandeginste et al., 2014; Al-Aasm et al., 2019). In the case of Devonian Massenkalk carbonates, Gillhaus et al. (2003) suggested the overgrowth of Dol 1(A) matrix dolomite by younger hydrothermal dolomite cement (Dol 1B to Dol 3). If this holds true, then this process explains the comparable isotopic values, higher paleotemperatures, and higher fluid salinities ($>21.5 \pm 1.8$ wt-% NaCl + CaCl₂; Table 2) between these phases. In contrast, the primary fluid inclusion homogenization temperature and fluid salinity in Dol 1A (40 °C, 6.6 ± 1.2 wt-% NaCl + CaCl₂, Fig. 18A, Table 2) versus much higher clumped isotope temperatures ($\Delta_{47} = 124 \pm 5$ °C, Fig. 16, Table 2) in the same phase, support subsequent overgrowth of Dol 1A. Alternatively, one type of deep-seated burial fluid precipitating different dolomite generations must be considered within a specific time interval. Dolomite phases U-Pb ages (Fig. 8, Table 2, Dol 1A: $381.4 \pm 21.8/22.0$ Ma and Dol 1B: $384.2 \pm 4.7/5.6$ Ma versus Dol 2A: $343.9 \pm 19.9/20.0$ Ma and Dol 2B: $339.3 \pm 24.9/25.4$ Ma), petrography and cross-cutting relationships suggest a series of different precipitation events between the Devonian and Carboniferous (Fig. 2B, 4C, D, 8E-H, 12A, B, E, F).

In SSW-NNE trending, cement-filled faults up to one metre in width, breccia clasts (μm to dm size, Fig. 3D, 12B, F) are encased three-dimensionally in Dol 2B cement. This remarkable observation is best explained by (i) collapse brecciation and very rapid cement

precipitation during the opening of these faults or (ii) fluid-induced brecciation related to ascending fluids from overpressured strata. Upward gushing fluids typically characterise overpressured basins that reach a threshold limit and burst open; this results in rapid pressure release, and previous work has suggested that cement precipitation might be rapid enough to encase fragments of the fracture walls that are broken off during this process (Jébrak, 1997).

Locally, the pre-Variscan and Variscan dolomite phases Dol 1 and Dol 2 were dedolomitised. The Dedol 1 $^{87}\text{Sr}/^{86}\text{Sr}$ ratios remained close to its Dol 2 precursor (Fig. 15). In contrast, $\delta^{13}\text{C}$ values of Dedol 1 shift towards lower values (Fig. 14). In contrast, Dedol 1 is moderately ^{18}O -enriched compared to the precursor phase (Fig. 14). Following a phase of quiescence in the wake of the Variscan dolomitisation, Variscan fractures were reactivated and opened, causing brecciation (Fig. 2C) and precipitation of hydrothermal LMC 1. The $\delta^{13}\text{C}$ and $\delta^{18}\text{O}$ values of LMC 1 (Fig. 14) differ from that of Dedol 1. In concert with the lower $\delta^{18}\text{O}$ values, Δ_{47} -temperatures and fluid inclusion homogenisation data suggest the presence of hot parent fluids (Fig. 16, Table 2, Δ_{47} -temperatures = 227 ± 17 °C; Fig. 16; $T_h = 209 \pm 9$ °C) with lower salinities compared to that precipitating dolomite phases (Table 2).

Although U-Pb dating of this phase was not feasible due to extremely high Pb-content $> 10^7$ cps, it seems clear that phase LMC 1 is geochemically not related to later paragenetic phases (Figs. 14, 15). A Permian reactivation of Variscan fractures and veins seems clear (Fig. 11; Tables 1, 2). The mechanism for dedolomitisation may be related to corrosive hydrothermal fluids migrating along the Variscan



(caption on next page)

Fig. 12. Main rock facies types in the Steltenberg Quarry and their depositional, diagenetic, and Tectonic features. Samples were cut, hand polished, scanned, redrawn, and complemented by a corresponding transmitted light thin section scan. (A, E) Massenkalk floatstone host rock with typical fossil content of sponges, corals, brachiopods and crinoids. Attached to this limestone is the burial dolo-grainstone Dol 1, typically accompanied by stylolites. (B, F) Partly dolomitised Massenkalk limestone with the Variscan dolomite phases Dol 2A (brownish eu- to anhedral matrix dolomite) and a Dol 2B saddle dolomite vein, which cut the limestone in the image horizontally. The Dol 2B veins often contain braccia clasts and few cataclaste of centimetre- to micrometre size, which arguably represents fragments from the hostrock that loosened from the fracture walls during tectonic activity and got trapped by the rapidly precipitating saddle dolomite. (C, G) Nearly dedolomitised Dol 3 from the Permian-Mesozoic Post-Variscan fault zone, including some of the most typical calcite and quartz phases related to hydrothermal and meteoric activity in this fault zone. Note the pervasive dedolomitisation and oxidation of the formerly Fe-rich Dol 3. (D, H) Permian-Mesozoic Dolomite breccia from the Post-Variscan fault zone overgrown by Cretaceous-Cenozoic types of cement LMC 5 to LMC 9.

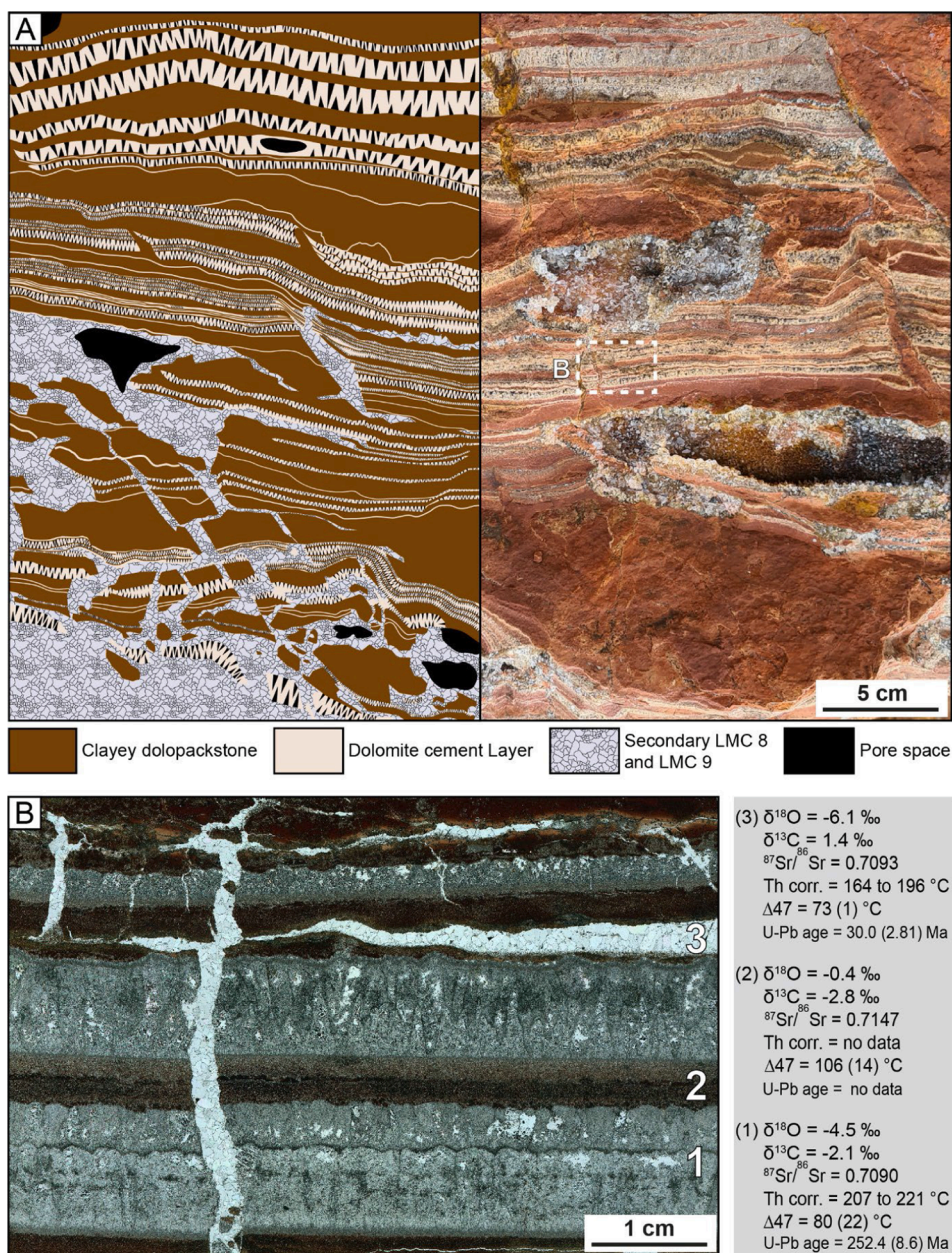


Fig. 13. Well-preserved sedimentary and cement layers in Laminite 1. (A) Re-drafted sedimentary and intercalated cement layers on the left correspond to features observed in the field on the right. The brown sedimented layers consist of a clayey dolopackstone whereas the cement layers consist of bladed dolomite cements. The dolomite phases were partly corroded, brecciated and filled by hydrothermal and meteoric calcite cements. (B) Thin section image of bladed Laminite 1 dolomite cement and clayey dolopackstones were cut by hydrothermal calcite cement veins. All three phases and their geochemical data (carbon, oxygen, strontium isotopes, fluid inclusion homogenisation temperatures, and clumped isotopes) are shown on the right.

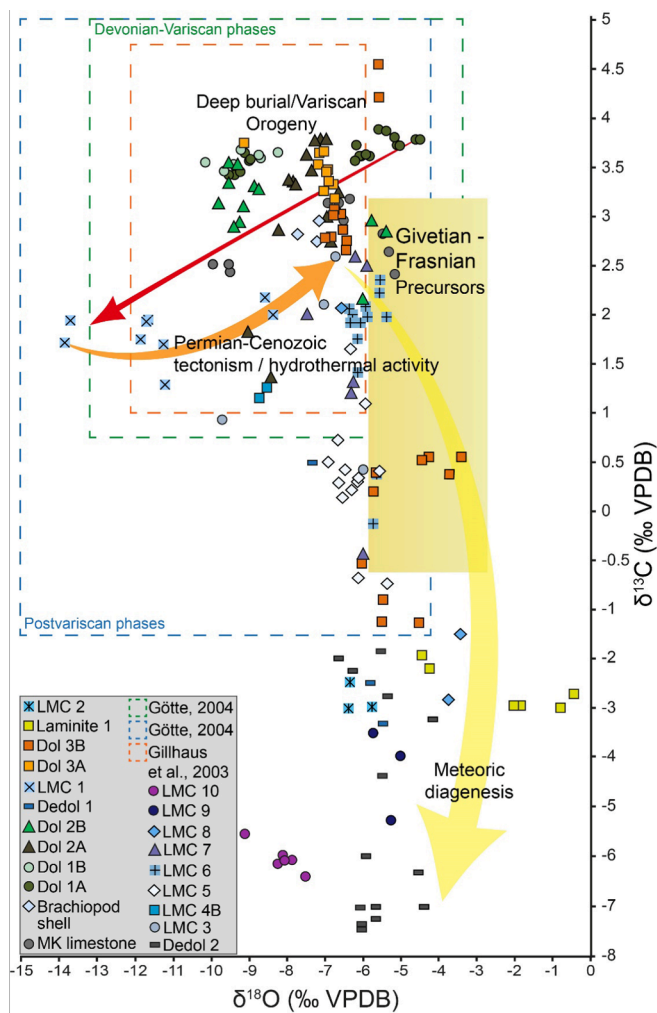


Fig. 14. Cross-plot of phase-specific $\delta^{18}\text{O}$ and $\delta^{13}\text{C}$ values for all analysed samples of dolomite and calcite phases at Steltenberg Quarry. The stable isotopic composition of Devonian (Givetian-Frasnian) marine calcites is indicated in the yellow and stippled purple boxes (from [Veizer and Prokoph, 2015](#); [Cramer and Jarvis, 2020](#); [Grossman and Joachimski, 2020](#)). Two dominant trends are present: burial diagenesis led to lower oxygen values (down to -14‰), and meteoric diagenesis to lower carbon values (down to -7.5‰). Modified from [Pederson et al., 2021](#).

fault system prior to LMC 1 precipitation or to meteoric fluids migrating in the uplifted rocks along faults at a later stage ([Lohmann, 1988](#); [Swart, 2015](#)).

5.2.4. Permian-Triassic tectonism, hydrothermal karstification and associated mineralisation

At the end of Variscan Orogeny, a clockwise rotation of the compressive stress field has caused an NNW-SSE extension in central Europe. This resulted in the reactivation of extensional structures that formed perpendicularly to the strike of the fold belt at the end of the Paleozoic due to crustal uplift and stretching until the Givetian ([Oncken, 1988](#)). In the Steltenberg Quarry, this tectonic phase is represented by the NNW-SSE trending regional Post-Variscan normal fault zone ([Fig. 2](#)).

The fault core and its side strands were used as conduits for corrosive hydrothermal fluids, resulting in hydrothermal (hypogene) karstification of the precursor limestone and earlier diagenetic phases. Hypogene karstification of carbonate rocks is known from many examples worldwide and differs from meteoric karsting ([Klimchouk et al., 2017](#) and references therein). In the Rhenish massif, hypogenic karsting is known from different locations and was interpreted as a consequence

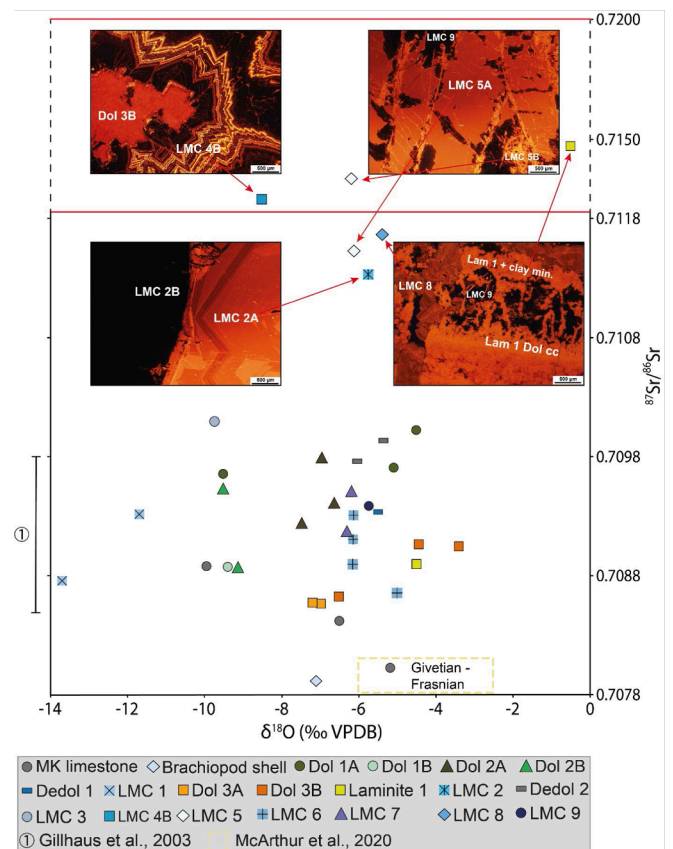


Fig. 15. Oxygen-isotope composition versus strontium-isotope ratios of dolomite and calcite phases compared to Givetian/Frasnian unaltered marine calcites from [McArthur et al. \(2020\)](#) and the range of a former study by [Gillhaus et al. \(2003\)](#). Except for one MK limestone bulk sample and a pristine brachiopod shell, there are no sample plots in the Givetian-Frasnian range for unaltered marine calcites. All remaining 36 samples are more radiogenic. The variation within most single phases is large, indicating a complex diagenetic overprint history. Most dolomite and calcite phases plot between 0.7090 and 0.7100, whereas some calcitic samples and one clayey dolostone, are more radiogenic up to values around 0.7150. The most radiogenic phases bear a possible clay content or were subject to hydrothermal and meteoric overprint from the Late Cretaceous onwards.

of hydrothermal/meteoric fluid mixing resulting in corrosive fluid composition ([Götte, 2004](#); [Drozdowski et al., 2017](#) and references therein; [Niggemann et al., 2018](#)). Previously, hypogenic karst in the Rhenish Massif was assigned to hydrothermal activity between the Late Triassic and the Early Cretaceous ([Götte, 2004](#); [Drozdowski et al., 2017](#)). Laminated dolomite cement intercalated with clayey dolograins in filled karst cavities and associated calcite cement from Steltenberg Quarry has a U-Pb age of $252.4 \pm 8.5/8.7$ Ma (Laminite 1) and $254.1 \pm 3.9/4.4$ Ma (LMC 2), respectively ([Figs. 9, 13, Table 2](#)). Remarkably, saddle dolomite cement from Devonian carbonates in the Sichuan Basin in southern China was recently U-Pb dated and assigned to the same phase of hydrothermal activity ([Chen et al., 2004](#); [Zou et al., 2023](#)). Although much of the Variscan overburden was eroded during the Permian, surface-related karstification ([Niggemann et al., 2018](#)) seems less likely due to the hydrothermal nature of all Post-Variscan fault zone-associated phases and the high clumped isotope and fluid inclusion temperatures assigned to Laminite 1 ([Figs. 16, 18](#)).

The low-salinity fluid inclusions compared to Variscan dolomites merit attention. According to [Götte \(2004\)](#), the Devonian limestones were buried at depths of $\geq 1,000$ m in the Late Permian/ Early Triassic and covered by sedimentary rock. The $\delta^{13}\text{C}$ and $\delta^{18}\text{O}$ values of Laminite 1 dolomite cement ([Fig. 14](#)) and associated LMC 2 cement ([Fig. 14](#))

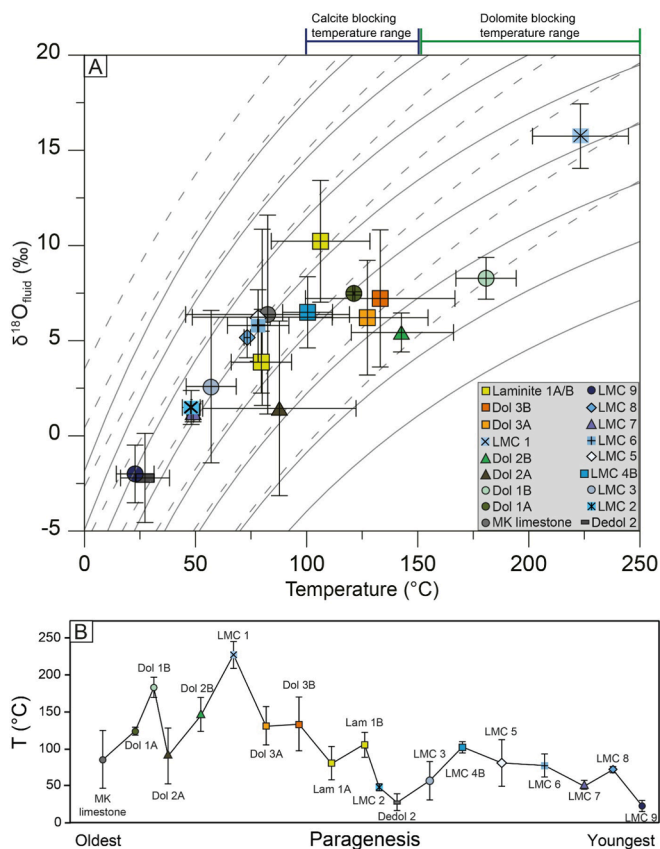


Fig. 16. Clumped isotope data of this study. (A) The cross plot between Δ_{47} -temperatures and $\delta^{18}\text{O}_{\text{fluid}}$ values of carbonates for all analysed paragenetic phases. The dashed and solid isolines are calculated by the fractionation equations of oxygen isotopes for calcite (Kim and O’Neil, 1997) and dolomite (Horita, 2014). Blocking temperature ranges of calcite and dolomite after Staudigel and Swart, 2016; Bonifacie et al., 2017; Lloyd et al., 2018; and Chen et al., 2019 indicated dark green (dolomite) and dark blue (calcite) lines between 100 and 300 °C, respectively. (B) Relative paragenetic age plotted against the clumped isotope temperature of all paragenetic samples from this study. The temperatures indicate several hydrothermal and meteoric activity phases. Note that LMC 1 exceeds the blocking temperature of calcite by nearly 100 °C, whereas all remaining calcite samples do not plot above a precipitation temperature of 100 °C. Amongst dolomite samples, only Dol 2B plots in the lower range of possible influence of blocking temperature.

differ significantly from that of the Variscan phases. According to Allan and Matthews (1982), meteoric fluids typically have lower $\delta^{13}\text{C}$ values due to soil-zone CO_2 . Mixing meteoric and hydrothermal fluids — at least during precipitation of LMC 2 — seems possible. If true, then mixing might explain the significantly lower clumped-isotope temperature of this phase compared to hot hydrothermal fluid inclusions ($\Delta_{47} = 48 \pm 4$ °C versus $T_{\text{h}} = 214 \pm 5$ °C; Figs. 16, 18). An alternative source for lower $\delta^{13}\text{C}$ values might be thermochemical sulphate reduction (Immenhauser, 2022 and references therein). Although Zechstein evaporite-related fluids might have influenced these carbonates, no sulphate-bearing fluid inclusions were found (Fig. 18). The presence of clay minerals in dolo-grainstones of Laminite 1 (Fig. 13) may indicate some form of a connection to stratigraphically overlying siliciclastic units during fluid convection through hydrothermal karst cavities. The $^{87}\text{Sr}/^{86}\text{Sr}$ ratios of Laminite 1 are highly variable (Fig. 15, Table 2, 0.709028 to 0.714721), a notion best explained by the influence of clay minerals on these laminated dolostones. Remarkably, LMC 2 does not exclusively occur as hypogene karst filling cement phase but also precipitated in veins up to 15 m thickness (Fig. 2D). Notably, this phase forms zoned radial calcite crystals up to meter-length. Therefore, they mark a first opening phase of the Post-Variscan fault system.

5.2.5. Late Triassic to Early Cretaceous dolomitisation, dedolomitisation, silicification and meteoric karstification

The replacement dolomite phase Dol 3 shares similarities with the Permian-Triassic dolomite cement phase in Laminite 1. Similarities include a clear genetic relation to the same fault zone, the macroscopic colour and similar cathodoluminescence properties (Fig. 5D, F; 6B). The $^{87}\text{Sr}/^{86}\text{Sr}$ ratios of some Dol 3B and clay-lean Laminite 1 samples overlap (Fig. 15). Morphologically, the equant (Laminite 1 dol cement) versus saddle dolomite (Dol 3) crystal morphology points to a different formation mechanism. Moreover, the carbon and oxygen isotope data of both dolomite phases differ significantly (Fig. 14, Table 2). Although there is a bimodal distribution in the isotopic composition of Dol 3B, partly similar to that of Laminite 1, it seems likely that some Dol 3 cement were altered by later hydrothermal and meteoric overprint in the Post-Variscan fault zone.

Geochemical differences are also evident in paleothermometric data (Figs. 16, 18). As the Δ_{47} -temperatures of Dol 3A and 3B are significantly higher than the ambient formation temperature and comparable to that of Dol 2, this implies a similar deep-seated burial fluid-related origin of Dol 3B to Devonian Dol 1B and Variscan Dol 2 phases, most evident in the high-salinity primary fluid inclusions of Dol 3 contrasted by the low-salinity inclusions in Laminite 1 (Figs. 17, 18 Table 2). Due to this phase’s low U- and high Pb-content, dating Dol 3 phases was unsuccessful. Given the different geochemical and paleothermometrical properties, this dolomite generation seems more likely related to hydrothermal activity in the Late-Triassic to Early Jurassic interval (see also Götte, 2004 and references therein). This pattern agrees well with an Early Jurassic fluid event on both sides of the Atlantic Ocean (e.g., Rddad et al., 2022 and references therein).

Comparing hydrothermal Dol 3 in Steltenberg Quarry to Late Triassic dolomites elsewhere (Geske et al., 2012; Gabellone et al., 2014; Preto et al., 2015; Hips et al., 2016; Mueller et al., 2020; Zou et al., 2023), it seems remarkable that most of these phases share a similar rock-buffered carbon isotopic composition, even after multiple tectonic, hydrothermal, and meteoric overprint (Fig. 14). It is at present unclear if this is an intrinsic pattern related to these fabrics or a more random coincidence related to a different set of mechanisms.

The precipitation of the calcite cement LMC 3 marks a pause between the dolomitising fluid pulses within Dol 3 precipitation events (Fig. 11). This phase holds some petrographic features comparable to Dol 2B, although these features are unique (Table 1). It often forms radial, dm-sized crystals encasing dolostone Dol 3 breccia clasts, which imply rapid crystallisation (Fig. 2F, 4E, F, Jébrak, 1997). The $\delta^{18}\text{O}$ values of LMC 3 are more negative compared to Dol 3, whereas the carbon isotope values are comparably variable (Table 2; Fig. 14). The temperatures of the fluids based on clumped isotope and fluid inclusion data are significantly lower than those of Dol 3 (Table 2, Figs. 16, 18). Evidence for a complex interplay between fluid composition and LMC 3 precipitation comes from the more radiogenic $^{87}\text{Sr}/^{86}\text{Sr}$ ratios in comparison to Dol 3 (Table 2, Fig. 15) and a bimodal fluid inclusion salinity and density distribution within LMC 3 domains (Table 2, Fig. 18).

The $\text{Na}_{\text{deficit}} \text{Ca}_{\text{excess}}$ discrimination diagram (Davisson and Criss, 1996; Bons et al., 2014; Kreissl et al., 2018; Kolchugin et al., 2020) can be used to decipher the genetic evolution of the fluid. Based on the data presented in Fig. 19, it seems likely that meteoric fluids interacted with Permian evaporites (in particular halite), leading to a halite dissolution brine. Such a brine has a high density and tends to migrate downwards, interacting with the crystalline basement underneath the Devonian basin. Fluid data forming a trend away from the halite dissolution brine indicate a combined process of sulphate dissolution, dolomitisation and water–rock interactions in crystalline rocks (clay mineral formation and albitisation). Since a bimodal fluid composition is trapped that shows variable degrees of evolution, it indicates that non-equilibrium processes overruled thermodynamic controls on the precipitation of diagenetic phases (Walter et al., 2018; Mueller et al., 2022b). The data imply short-lived fluid pulses of basement fluid into a shallower burial

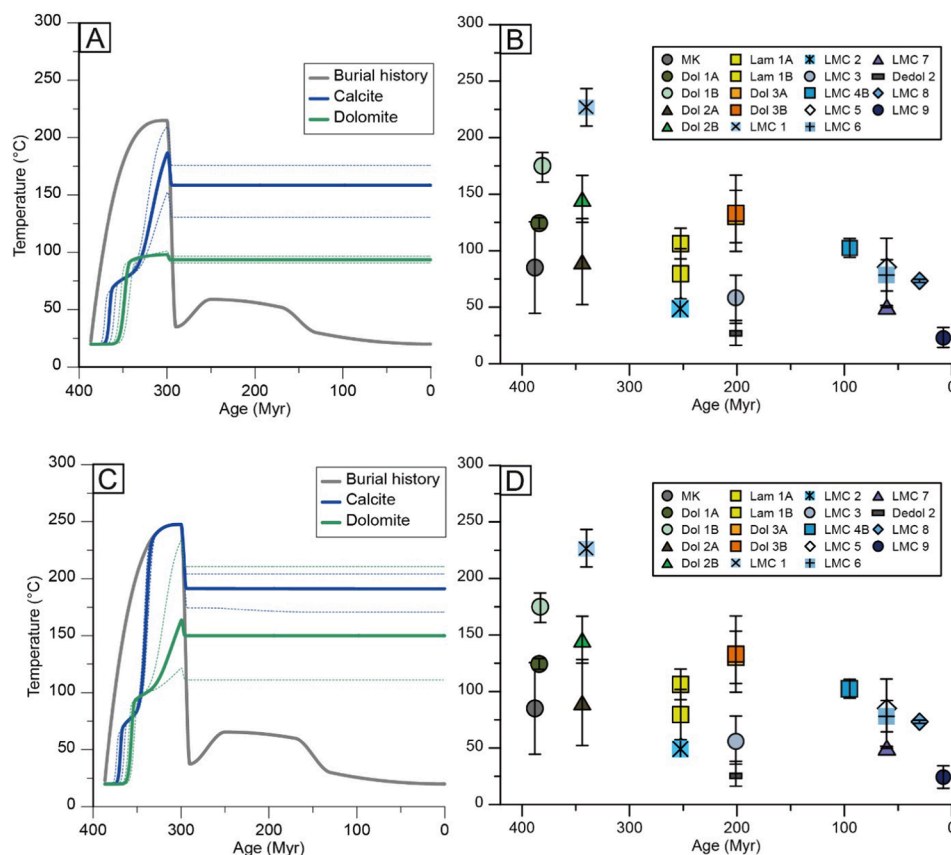


Fig. 17. The comparison between the modelled and measured Δ_{47} -temperatures. (A) and (C) The modelling Δ_{47} -temperatures from the solid-state reordering model of Lloyd et al. (2018). The dash lines represent the modelling errors. The input geothermal gradient for the study area in (A) is 30 °C/km whereas in (C) it is 35 °C/km (Agemar et al., 2012). (B) and (D) The changes in measured Δ_{47} -temperatures depend on the paragenetic sequence and U-Pb dating ages.

regime, resulting in rapid precipitation of calcite cement. Similar to petrographic features, such processes are known from over-pressured basins (e.g., Osborne and Swarbrick, 1997; Tingay et al., 2007; Frazer et al., 2014; Peacock et al., 2019) where tectonic events may cause fluid to ascent into a shallower burial regime while the fluid decompresses, which causes LMC 3 to precipitate around uprising clasts of older lithologies during an escape burst (De Riese et al., 2020). Dol 3 veins in LMC 3 imply that multiple pulses of dolomitising fluids occurred (Fig. 11).

Decimetre-sized vugs and the presence of cell dolomite within Dol 3 dolostones suggest karstification after the end of Dol 3 precipitation. This phase is marked by the pervasive dedolomitisation of dolostones (Fig. 3E, F; 5G, H; 12C, G). The phase Dedol 2 has a $\delta^{13}\text{C}_{\text{mean}}$ value of -5.1‰ and a clumped-isotope temperature of $27 \pm 11\text{ °C}$ (Figs. 14, 16), pointing to meteoric fluids as drivers for dedolomitisation. Nevertheless, there is evidence of a hydrothermal component in some primary fluid inclusions (Fig. 18). This is also exemplified in the U-Pb age of fluid inclusion lean microcrystalline LMC 4A ($125.6 \pm 8.2/8.4\text{ Ma}$, Table 2). Karst chutes with spores and pollen (Drozdowski et al., 1998) and dinosaur/mammal bones (Lanser and Heimhofer, 2015; Martin et al., 2021) point at a Lower Cretaceous minimum age for karstification. All these arguments indicate a complex interaction between hydrothermal and surface-related meteoric karstification at different time/depth intervals. Indicators for renewed hydrothermal activity are found within dolostones near the Post-Variscan fault zone within Steltenberg Quarry (Fig. 5H, 12C, G). Vugs and matrix porosity in Dol 3 dolostones were subsequently occluded by quartz cement between The Jurassic and the Cretaceous (Götte, 2004; Götte and Richter, 2003). These cement phases are occasionally overgrown by sulphide minerals, including chalcopyrite or pyrite (digital supplement S1; Götte, 2004).

5.2.6. Late Cretaceous-Paleogene Alpine Orogeny far-field effects and Oligocene-Recent meteoric karstification and cementation

Renewed tectonic activity (Breccia 4, Fig. 11) and mineralisation within the Post-Variscan fault zone, as well as the occurrence of an Alpine vein set (Fig. 2 and digital supplement S1; 120/65), heralds a new phase in the tectonic regime. Veins are now occluded by calcite cement (LMC 4B to LMC 8), assigned to a time interval between the Late Cretaceous (LMC 4B: $95.02 \pm 2.59/2.70\text{ Ma}$; Fig. 9, Table 2) and the Oligocene (LMC 8: $30.0 \pm 2.80/2.81\text{ Ma}$; Fig. 9, Table 2). These data agree with compressional tectonics and associated uplift caused by the reorientation of the European Cenozoic Rift System prior to and during the Alpine Orogeny. These events resulted in large-scale mineralisation in many European regions (Maillard and Mauffret, 1999; Kley, 2013; Walter et al., 2018a, b; Mueller et al., 2020). While the $\delta^{13}\text{C}$ and $\delta^{18}\text{O}$ values of calcite phases are highly variable (Table 2, Fig. 14), the $^{87}\text{Sr}/^{86}\text{Sr}$ ratios of LMC 4B, LMC 5 and LMC 8 are highly radiogenic compared to LMC 6 and 7 (Table 2, Fig. 15). This geochemical variability, combined with overall warm to cool hydrothermal clumped isotope temperatures versus warm and hot hydrothermal fluid inclusion temperatures points to a range of fluid sources within the Late Cretaceous to the Oligocene interval.

The Δ_{47} -temperatures from LMC 4B to LMC 9 show a decreasing trend, which is also observed in the $\delta^{18}\text{O}_{\text{fluid}}$ values calculated by Δ_{47} -temperatures and $\delta^{18}\text{O}$ values of calcites. Such trends indicate the multi-aquifer fluid mixing processes are recorded in the calcite types of cement, which is similar to Schwarzwald and Spessart mining districts (Fußwinkel et al., 2014; Walter et al., 2018a, 2019, 2020b).

The Cenozoic period in SW Germany was dominated by the breakup of Europe along the Central European Rift System, and numerous aquifers were juxtaposed and short-circuited. This leads to the observed

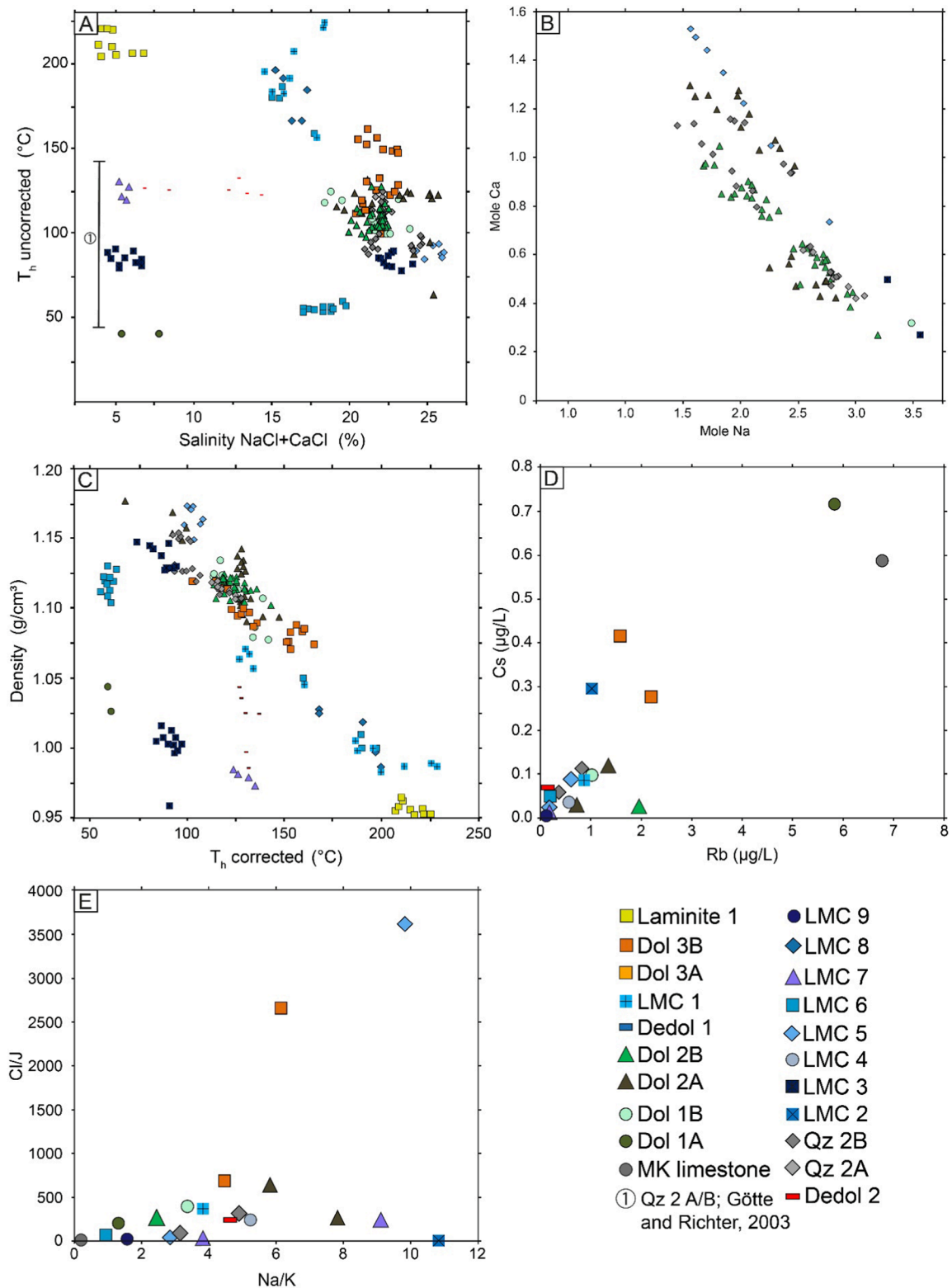


Fig. 18. Fluid inclusion and crush leach data compiled from single phases in the context of this study. (A) Salinity versus T_h uncorrected for all analysed fluid inclusions in this study. (B) Mole Na versus mole Ca content of the fluid. Variations in Ca contents of the fluids based on microthermometry of individual inclusions. (C) T_h corrected versus fluid inclusion density for all analysed fluid inclusions in this study. (D) Rb versus Cs content. (E) Na/K versus Cl/J.

variability in the fluid chemistry of hydrothermal precipitates with 0–28 wt% salinity and 50 to 350 °C even within a single vein (Walter et al., 2018a, b). The source of the fluids trapped in the Steltenberg Quarry faults is likely meteoric or marine, but various processes later altered these waters. Interaction with halite is indicated by a $Na_{\text{deficit}}/$

Ca_{excess} diagram, whereas the Rb/Cs ratios provide strong evidence for interaction with clay minerals. The Cl/Br ratios are significantly below seawater (Cl/Br = 288), indicating a fluid evolution via bittern brine generation.

Given that a bittern brine and a halite dissolution brine both contain

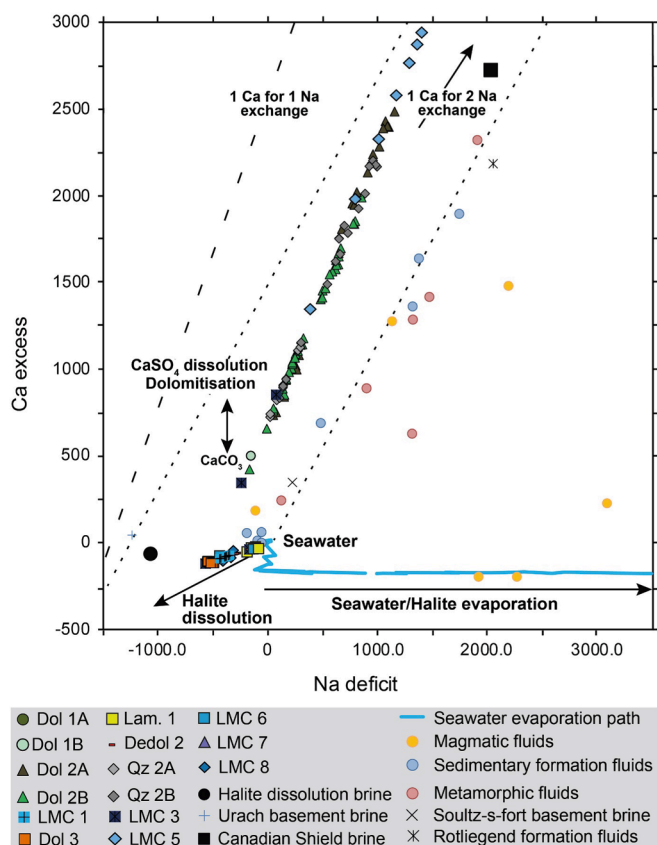


Fig. 19. $\text{Na}_{\text{deficit}}/\text{Ca}_{\text{excess}}$ plot for all analysed fluid inclusions after [Davisson and Criss \(1996\)](#). Halite dissolution into seawater or freshwater produces negative values along a slope of 1:4. When followed by 2Na for 1 Ca exchange, excess-deficit values increase along a unit slope. Reactions involving 1Na for 1 Ca exchange produce slopes of 2:1 in this construction. Reactions involving Ca only produce vertical shifts, while seawater evaporation initially follows a vertical descent but afterwards produces large deficits along with a horizontal trend. Mixing on the excess-deficit plot forms a straight line between two involved endmember fluids. Note, due to the absence of published fluid chemistry data from underlying strata, data from other studies were used to characterise this study's $\text{Na}_{\text{deficit}}/\text{Ca}_{\text{excess}}$ data. Note: The latter plots between three endmember fluids: Seawater, a halite dissolution brine, and a crystalline/metamorphic fluid. Several endmember fluid compositions from published literature were included from [MacCaffrey et al. \(1987\)](#); [Pauwels et al. \(1993\)](#); [Stober and Bucher \(2004\)](#); [Yardley, 2005](#); [Lüders et al. \(2010\)](#) and [Göb et al. \(2013\)](#).

salinities > 20 wt% NaCl + CaCl₂, but the fluid salinities show strong variabilities towards lower contents; it is most likely a third low salinity meteoric/connate fluid that dilutes the two mixed high salinity brines. The observations indicate a multi-component mixing between a modified bittern brine, a halite dissolution brine and a low salinity meteoric/connate fluid. Once more, the same fluid endmembers were identified in the Schwarzwald and Odenwald mining districts in Germany and seem over-regional ([Burisch et al., 2017](#); [Walter et al., 2018a, b, 2020b](#)).

Quartz trace element patterns for Qz 2 and 3 strongly support the fluid mixing process. These reflect changes in the mixing ratios during the fluid mixing process as the trace elements behave in concert and rhythmic. Moreover, the fluid data indicate a mixing line ([Fig. 19](#)). A relationship to the Cenozoic magmatism in southern and western

Germany is unlikely as it has been previously shown that the Cenozoic magmatism is following the same tectonic forces compared to the Cenozoic hydrothermal system. No genetic relationship between the magmatites and the hydrothermal fluids can be deciphered ([Braunger et al., 2018](#); [Walter et al., 2018b, c](#); [Burisch et al., 2018](#); [Binder et al., 2023](#) and references therein).

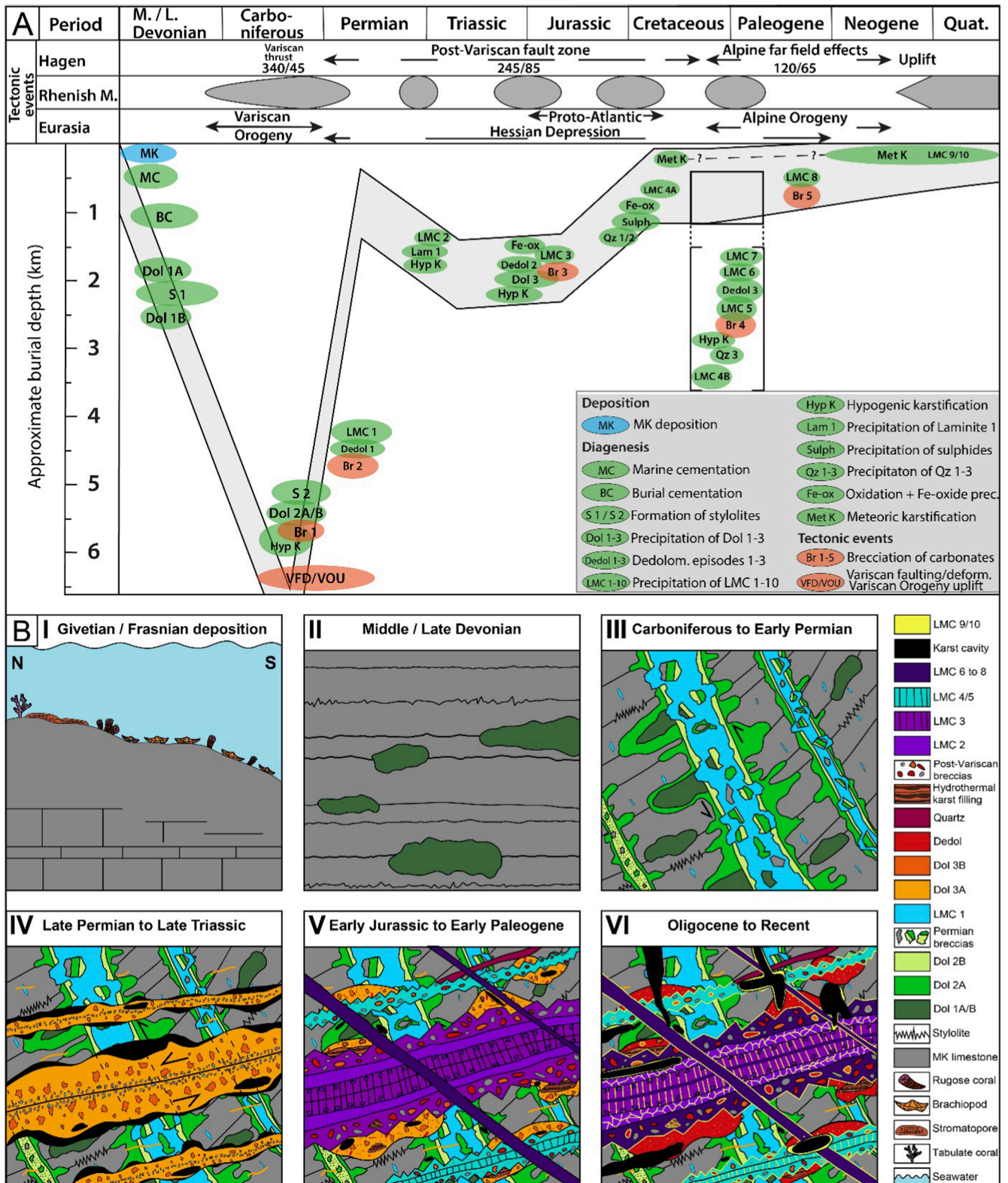
Evidence for yet another karstification interval comes from Dedol 3 ([Table 1](#), [Fig. 11](#)). Karstification occurred prior to hydrothermal LMC 5 to LMC 7 precipitation in veins cross-cutting dolostones (LMC 5A: $60.81 \pm 6.02/6.04$ Ma; LMC 5B: $63.85 \pm 5.62/5.64$ Ma; LMC 7: $60.5 \pm 9.57/9.58$ Ma; [Fig. 9](#), [Table 2](#)). The karstification timing prior to LMC 5 to LMC 7 precipitation is supported by sediments filling a single karst chute containing Late Cretaceous microfossils ([Drozdowski et al., 2017](#)). These findings may indicate both a hypogene component as well as a meteoric during karstification or, alternatively, two individual karstification intervals prior to LMC precipitation. LMC 8 between Breccia 5 clasts ([Figs. 11, 13](#)) within the Post-Variscan fault zone indicates over-pressured fluid or renewed tectonism coeval to hydrothermal LMC 8 precipitation. Generally, regional hydrothermal activity became less significant after the Eocene. According to [Hammerschmidt et al. \(1995\)](#), overlying Cretaceous sediments were largely eroded in the region within the Late Paleogene, a feature that gave access to near-surface meteoric karstification and cementation of the Devonian units ([Fig. 3G](#)).

Carbonate dissolution under the influence of meteoric fluids led to Oligocene to (most dominantly) Quaternary karstification in this portion of the Rhenish Massif ([Drozdowski et al., 2017](#); [Niggemann et al., 2018](#) and references therein). Meteoric cement phases LMC 9 and 10 are characterised by $\delta^{13}\text{C}$ values as low as -6% and a clumped isotope temperature of 23 ± 8 °C (LMC 9). Refer to [Fig. 20](#) for a chronological overview of all depositional, diagenetic and tectonic stages, including the reconstructed burial history of the Massenkalk limestones.

5.3. Significance of this work for proxy research and proposed way forward

The analytical tools applied here, such as phase-specific isotope geochemistry, fluid paleo-temperature reconstruction, or age dating, have been applied in numerous previous studies. The rigorous combination of these tools, however, placed into a very detailed and dated paragenetic context, has been rarely used and defines the significance of this study for geochemical proxy research ([Table 5](#)). This study documents that even extremely complex carbonate archives can be understood in terms of their proxy data. The difficulty in extracting environmental archive data from carbonate rocks may increase with progressively older strata ([Mueller et al., 2020](#) and references therein), but that is not always so. Proxy data in some Precambrian carbonate archives seem well preserved, and such in Neogene rocks may be fully overprinted. In this sense, this study's relevance is not limited to geologically old rocks.

Acknowledging that (fortunately!) not all carbonate archives are as complex as the case example described here, it is argued that geochemical proxy data must be placed in a solid petrographic/paragenetic context to decipher their meaning. Even the most sophisticated geochemical instrumentation in the laboratory, often combined with modelling, cannot compensate for a lack of geological/petrographic context of proxy data analysed. This understanding is relevant as petrographically altered rocks might record fairly well-preserved (closed system) geochemical proxy data, while even aragonitic archives, often considered pristine, might have experienced some degree of (open system) geochemical resetting ([Fichtner et al., 2018](#); [Pederson](#)



(caption on next page)

Fig. 20. Chronological evolution of the rocks in Steltenberg Quarry. (A) Interpreted burial history, tectonic events, and the associated diagenetic processes affecting Massenkalk carbonates from deposition in the Middle/Late Devonian to Recent. Large-scale tectonic processes include the Variscan Orogeny, the development of the Hessian Depression and Alpine Orogeny. The maximum burial depth and tectonic events were compiled after Drozdowski and Wrede (1994), Götte (2004), Sengör and Natal'in (2001) and complemented by own data. The formation depth of phases Dol 3 to LMC 3 and LMC 4 to LMC 7 is given in rectangles above these two groups. (B) Summary of the key events that lead to precipitation and overprint of the carbonate phases discussed in this study. (I) Deposition and early diagenetic cementation in a shallow marine fore-reefal environment in the Middle/Late Devonian. (II) Deep burial down to 6–7 km, precipitation of Dol 1 and development of stylolites. (III) Folding and faulting during Variscan Orogeny and later overprint by the Variscan thrust fault zone, resulting in the precipitation of Dol 2 and later brecciation and precipitation of LMC 1 in the Permian. (IV) Tectonic and hydrothermal overprint by the Post-Variscan fault zone from the Permian to the Early Triassic, resulting in precipitation of Dol 3, hypogenic karstification (Laminite 1), brecciation and multiphase quartz and LMC cementation also leading to partial dedolomitisation. (V) Renewed hydrothermal and tectonic overprint by the Post-Variscan fault zone from the Triassic to Early Paleogene, resulting in multiphase LMC and quartz (gangue) cementation, partial dedolomitisation, brecciation and rapid cementation with LMC 3. Alpine Orogeny far-field effects triggered the Cretaceous-Paleogene fluids from which hydrothermal cement LMC 5 to LMC 8 precipitated. (VI) This phase was followed by intense Meteoric karstification and cementation with meteoric LMC 9 and 10, partly overprinting many older carbonate phases.

Table 5

Exemplary compilation of some well-cited diagenetic studies in predominantly highly overprinted Archean to Mesozoic rocks from the last three decades and their applied methods plotted against the methods from this study.

Study	Age	U-Pb carb. dating	Microscopy	CL	Cement strat.	XRF	Δ_{47}	Fluid incl.	Crush-Leach	$\delta^{13}\text{C} / \delta^{18}\text{O}$	$^{87}\text{Sr}/^{86}\text{Sr}$	Trace elem.
This study	Devonian-Subrecent	X	X	X	X	X	X	X	X	X	X	X
Mangenot et al., 2018	Jurassic-Paleogene	X	X	X	X	n/a	X	X	n/a	X	n/a	n/a
Hansman et al., 2018	Palaeozoic-Quaternary	X	n/a	n/a	n/a	n/a	n/a	n/a	n/a	n/a	n/a	n/a
Guo et al., 2016	Cambrian-Ordovician	n/a	X	X	X	n/a	n/a	X	n/a	X	X	n/a
Cui et al., 2016	Neoproterozoic	n/a	X	X	X	n/a	n/a	n/a	n/a	X	X	n/a
Bristow et al., 2011	Neoproterozoic	n/a	X	n/a	n/a	n/a	X	n/a	n/a	X	X	X
Pecoits et al., 2009	Neoproterozoic	n/a	X	n/a	X	n/a	n/a	n/a	n/a	n/a	n/a	X
Melezhik et al., 2009	Neoproterozoic	n/a	X	n/a	n/a	X	n/a	n/a	n/a	X	X	X
Jiang et al., 2006	Neoproterozoic	n/a	X	n/a	n/a	n/a	n/a	n/a	n/a	X	n/a	n/a
Campbell et al., 2002	Jurassic-Cretaceous	n/a	X	X	X	n/a	n/a	n/a	n/a	X	n/a	X
Azmy et al., 2001	Neoproterozoic	n/a	X	X	X	n/a	n/a	X	n/a	X	X	X
Kamber and Webb, 2001	Neoproterozoic	n/a	n/a	n/a	n/a	n/a	n/a	n/a	n/a	n/a	X	X
Kennedy, 1996	Neoproterozoic	n/a	X	n/a	n/a	n/a	n/a	n/a	n/a	X	X	n/a
Kaufman et al., 1991	Neoproterozoic	n/a	X	X	n/a	n/a	n/a	n/a	n/a	X	n/a	n/a
Burley et al., 1989	Jurassic	n/a	X	X	X	n/a	n/a	X	n/a	n/a	n/a	n/a

et al., 2020 and references therein). Compiling a detailed paleo-temperature record of diagenetic fluids is not trivial but a further prerequisite of an in-depth understanding of proxy data. Combining fluid inclusion data and carbonate-clumped isotope temperatures is the most promising way forward (Millán et al., 2016; Came et al., 2017; Honlet et al., 2018; Mueller et al., 2022b).

The temporal and regional framework of the chain of diagenetic events that shape complex geological archives and their proxy data is often poorly constrained, even when the depositional age of the unit is well established. Compiling a radiometric chronology of diagenetic events in ancient carbonate archives is a prerequisite for complex carbonate archives. Platform- or basin-wide events, contact metamorphism (Kaufman et al., 1991; Melezhik et al., 2003; Holness and Fallick, 2004; Laskar et al., 2016), or orogenic and other far-field tectonic phases may be recorded in the cross-cutting relationships of cemented veins and their geochemical data (Burley et al., 1989; Campbell et al., 2002; Guo et al., 2016; Dong et al., 2017). A given regional or even local tectonic framework may respond to tectonic processes > 1000 km away, such as the opening of the Proto-Atlantic from the Early Jurassic to the Early Cretaceous (Walter et al., 2018; Mueller et al., 2020; Burisch et al., 2022), and these events may, in turn, be recorded in proxy data. Radiometric U-Pb series dating in carbonates is not restricted to specific

carbonate mineralogy as long as the naturally occurring U:Pb is variable enough within a given sample (Rasbury and Cole, 2009). These data can be used to build a quantitative age model of diagenetic events.

6. Conclusions

This study documents and discusses the significance of marine-depositional and local to far-field diagenetic events preserved in a highly complex, U-Pb-dated Devonian-Cenozoic carbonate archive. Carbon, oxygen and radiogenic strontium data are extracted from a succession of sedimentary and diagenetic phases and placed in a paleo-temperature context.

The geological history of these limestones began in the Middle/Late Devonian with protolith deposition and partial dolomitisation during rapid burial (Dol 1 = $384.2 \pm 4.7/5.6$ Ma) at fluid temperatures up to 180 °C. Following subsequent burial to ca 6.5 km depth. Variscan Orogeny caused fault zone brecciation and hydrothermal dolomitisation (Dol 2 = $343.9 \pm 19.9/20.0$ Ma) from highly saline burial fluid (18–25 wt% NaCl + CaCl₂) at temperatures between ca 90 and 150 °C.

Rapid uplift to ca 1–2 km burial depth and reorganisation of the stress regime in the late phase of Variscan Orogeny resulted in additional fault zone overprint and a series of hydrothermal fluid pulses triggered

by multiple tectonic far-field effects between the latest Paleozoic and Cenozoic. These fluids' chemical composition varied from being corrosive to highly oversaturated for carbonates, silicates and sulphates. While pre-existing dolomites were partly brecciated and dissolved (Dedol 1) by corrosive fluids, cement precipitation within this interval is first recorded in LMC 1 formation at 200 to 240 °C. Corrosive fluids created hypogene karst voids up to tens of metres in size filled by dolomite (Lam 1) and calcite (LMC 2) cement at fluid temperatures between ca 50 and 220 °C in the latest Permian/earliest Triassic (Lam 1 = $252.4 \pm 8.5/8.7$ Ma; LMC 2 = $254.1 \pm 3.9/4.4$ Ma).

Tectonic quiescence prevailed until the Late Triassic/Early Jurassic when hydrothermal activity was likely reactivated by large-scale tectonism related to the opening of the Proto-Atlantic Ocean until the Early Cretaceous. This series of tectonic/hydrothermal precipitation and/or brecciation events was initiated with an additional pulse of corrosive fluids followed by a series of dolomite (Dol 3), dedolomite (Dedol 2), calcite (LMC 3), quartz cement (Qz 1, 2), and sulphides. Dolomite Dol 3 precipitated between ca 90 and 130 °C, whereas calcite LMC 3 formed at ca 50 to 90 °C and quartz Qz 2 at ca 100 °C.

The uppermost layers of the limestone host rock were partially dissolved by surface water-related meteoric karstification from the Early Cretaceous onwards. In contrast, deeper buried units were affected by hydrothermal fluid pulses between the Early Cretaceous and the late Paleogene. These pulses lead to renewed hypogene karstification and later precipitated hydrothermal calcites LMC 4A ($125.6 \pm 8.2/8.4$ Ma) to LMC 8 ($30.0 \pm 2.80/2.81$ Ma). The calcite cements formed from different fluids between ca 50 °C (LMC 7) and ca 180 °C (LMC 8). Late Cretaceous-Paleogene fluid pulses were most likely related to Alpine Orogeny.

Meteoric karstification and cement precipitation are recorded during the Oligocene to Recent, and calcite phases LMC 9 and LMC 10 formed, characterised by $\delta^{13}\text{C}$ values as low as -6% .

The work shown here has broader significance for understanding the complexity of geochemical proxy systems, mechanisms and processes in their petrographic and temporal context. Most importantly, and in spite of the complex tectono-diagenetic evolution of these rocks, protolith limestones preserved their respective Middle/Late Devonian dissolved inorganic carbon (DIC) and to a large extent their $^{87}\text{Sr}/^{86}\text{Sr}$ signatures. Despite partially rock buffered $\delta^{13}\text{C}$, all other phases reflect the composition of their diagenetic parent fluids. The data and interpretations presented in this study cannot be uncritically applied to geologically complex archives as such; each archive is perhaps a case of its own. That said, the message brought forward here is encouraging. If properly applied, the tools in our hands can potentially reconstruct environmental proxy data even from old and very complex carbonate archives.

CRedit authorship contribution statement

M. Mueller: Writing – review & editing, Writing – original draft, Visualization, Validation, Supervision, Software, Resources, Project administration, Methodology, Investigation, Funding acquisition, Formal analysis, Data curation, Conceptualization. **B.F. Walter:** Writing – review & editing, Writing – original draft, Methodology, Investigation, Funding acquisition, Formal analysis, Data curation. **R.J. Giebel:** Writing – review & editing, Writing – original draft, Visualization, Methodology, Investigation, Formal analysis, Data curation. **A. Beranoaguirre:** Writing – review & editing, Writing – original draft, Project administration, Funding acquisition, Conceptualization. **P.K. Swart:** Writing – review & editing, Writing – original draft, Methodology, Formal analysis, Data curation. **C. Lu:** Writing – review & editing, Writing – original draft, Visualization, Formal analysis, Data curation. **S. Riechelmann:** Writing – review & editing, Writing – original draft, Methodology, Formal analysis, Data curation. **A. Immenhauser:** Writing – review & editing, Writing – original draft, Project administration, Funding acquisition, Conceptualization.

Data Availability

All data associated to this paper (Data S1 – C, O, XRD, ICP, Sr isotopes; Data S2 – Clumped isotopes; Data S3 – Fluid inclusions; Data S4 – Crush leach; Data S5 – U-Pb; Data S6 – Quartz trace elements) are available through Mendeley Data at <https://doi.org/10.17632/8rzs9hx6tv.2>.

Declaration of competing interest

The authors declare that they have no known competing financial interests or personal relationships that could have appeared to influence the work reported in this paper.

Acknowledgements

This study was performed in the context of the DFG grants MU 4916/1-1, IM 44/22-1, IM 44_27_1 and WA 3116_16-1. The authors are grateful to the managers of Steltenberg Quarry Dr. C. Lange and Dr. M. Lange, for their continuous permission to perform fieldwork. Special thanks go to Dr. K. Lippert for his continuous support during fieldwork. Thanks go to M. Born, A. Schulz, and T. Seemann from the thin section preparation department at Ruhr-Universität Bochum. For the execution of X-ray diffraction measurements, thanks go to H. Mammen from the central microanalytics department. For assistance in element concentration and C, O and Sr isotope analyses, thanks go to K. Krimmler and B. Gehnen. J. Parr and N. Marre are thanked for their assistance in drawing figures. Thanks go to T. Unger for proofreading. E. Eiche, M. Denker, and C. Möbner (all LERA facilities, KIT) are acknowledged for their help with crush leach analyses. The LERA laser ablation facility is supported by DFG INST 121384/213-1 FUGG. We greatly acknowledge the editors J. G. Catalano and C. Li and the valuable comments of four anonymous GCA reviewers.

Appendix A. Supplementary material

Supplementary file includes detailed methodology and results, four figures (circumstantial cathodoluminescence images), and six tables (detailed results of all methods used for comprehensive tables in the paper).

Supplementary material to this article can be found online at <https://doi.org/10.1016/j.gca.2024.04.029>.

References

- Agemar, T., Schellschmidt, R., Schulz, R., 2012. Subsurface Temperature Distribution of Germany. *Geothermics* 44, 65–77.
- Al-Aasm, I.S., Mrad, C., Packard, J., 2019. Fluid compartmentalization of Devonian and Mississippian dolostones, Western Canada Sedimentary Basin: petrologic and geochemical evidence from fracture mineralization. *Can. J. Earth Sci.* 56, 265–305.
- Allan, J.R., Matthews, R.K., 1982. Isotope signatures associated with early meteoric diagenesis. *Sedimentology* 29, 797–817.
- Anderson, N.T., Kelson, J.R., Kele, S., Daëron, M., Bonifacie, M., Horita, J., Mackey, T.J., John, C.M., Kluge, T., Petschnig, P., Jost, A.B., Huntington, K.W., Bernasconi, S.M., Bergmann, K.D., 2021. A Unified Clumped Isotope Thermometer Calibration (0.5–1,100 °C) Using Carbonate-Based Standardization. *Geophys. Res. Lett.* 48 e2020GL092069.
- Balcewicz, M., Ahrens, B., Lippert, K., Saenger, E.H., 2021. Characterization of discontinuities in potential reservoir rocks for geothermal applications in the Rhine-Ruhr metropolitan area (Germany). *Solid Earth* 12 (1), 35–58.
- Bathurst, R.G.C., 1971. Carbonate sediments and their diagenesis. *Sedimentology* 12, 394–413.
- Beckmann, H., 1948. Mikrofaunen von der Mitteldevon-Oberdevongrenze im nördlichen Sauerland. *Doctoral dissertation University of Marburg*.
- Beranoaguirre, A., Vasiliev, I., Gerdes, A., 2022. In situ LA-ICPMS U-Pb dating of sulfates: applicability of carbonate reference materials as matrix-matched standards. *Geochronology* 4, 601–616.
- Bernard, S., Daval, D., Ackerer, P., et al., 2017. Burial-induced oxygen-isotope re-equilibration of fossil foraminifera explains ocean paleotemperature paradoxes. *Nat Commun* 8, 1134.
- Binder, T., Marks, M.A., Gerdes, A., Walter, B.F., Grimmer, J., Beranoaguirre, A., Wenzel, T., Markl, G., 2023. Two distinct age groups of melilitites, foidites, and

- basanites from the southern Central European Volcanic Province reflect lithospheric heterogeneity. *Int. J. Earth Sci.* 112, 881–905.
- Blättler, C.L., Higgins, J.A., Swart, P.K., 2019. Advected glacial seawater preserved in the subsurface of the Maldives carbonate edifice. *Geochim. Cosmochim. Acta* 257, 80–95.
- Böhm, F., Gussone, N., Eisenhauer, A., Dullo, W.-C., Reynaud, S., Paytan, A., 2006. Calcium isotope fractionation in modern scleractinian corals. *Geochim. Cosmochim. Acta* 70, 4452–4462.
- Boiron, M.C., Cathelineau, M., Richard, A., 2010. Fluid flows and metal deposition near basement/cover unconformity: lessons and analogies from Pb-Zn-F-Ba systems for the understanding of Proterozoic U deposits. *Geofluids* 10, 270–292.
- Boni, M., Parente, G., Bechstadt, T., De Vivo, B., Iannace, A., 2000. Hydrothermal dolomites in SW Sardinia (Italy): evidence for a widespread late-Variscan fluid flow event. *Sed. Geol.* 131 (3–4), 181–200.
- Bonifacie, M., Calmels, D., Eiler, J.M., Horita, J., Chaduteau, C., Vasconcelos, C., Agrinier, P., Katz, A., Passey, B.H., Ferry, J.M., Bourrand, J.-J., 2017. Calibration of the dolomite clumped-isotope thermometer from 25 to 350 °C, and implications for a universal calibration for all (Ca, Mg, Fe)CO₃ carbonates. *Geochim. Cosmochim. Acta* 200, 255–279.
- Bons, P.D., Fusswinkel, T., Gomez-Rivas, E., Markl, G., Wagner, T., Walter, B., 2014. Fluid mixing from below in unconformity-related hydrothermal ore deposits. *Geology* 42, 1035–1038.
- Brand, U., Logan, A., Bitner, M.A., Griesshaber, E., Azmy, K., Buhl, D., 2011. What is the ideal proxy of Palaeozoic seawater chemistry? *AAP Memoir* 41, 9–24.
- Braunger, S., Marks, M.A.W., Walter, B.F., Neubauer, R., Reich, R., Wenzel, T., Parsapoor, A., Markl, G., 2018. The petrology of the Kaiserstuhl Volcanic Complex, SW Germany: The importance of metasomatized and oxidized lithospheric mantle for carbonate generation. *J. Petrol.* 59 (9), 1731–1762.
- Bruckschen, P., Richter, D.K., 1993. Zementstratigraphische Grundmuster in marinen Karbonatablagerungen des Phanerozoikums – Ein Abbild der normalen Beckenentwicklung. *Zentralblatt für Geologie und Paläontologie, Teil I: Allgemeine, Angewandte, Regionale Und Historische Geologie* 7–8, 959–972.
- Bruckschen, P., Neuser, R.D., Richter, D.K., 1992. Cement stratigraphy in Triassic and Jurassic limestones of the Weserbergland (northwestern Germany). *Sed. Geol.* 81 (3–4), 195–214.
- Buggisch, W., Joachimski, M.M., 2006. Carbon isotope stratigraphy of the Devonian of Central and Southern Europe. *Palaeogeogr. Palaeoclimatol. Palaeoecol.* 240 (1–2), 68–88.
- Büker, C., 1996. Absenkungs-, Erosions- und Wärmeflussgeschichte des Ruhr-Beckens und des nordöstlichen Rechtsrheinischen Schiefergebirges. - *Diss. Forschungszentrum Jülich*, 212 p., Jülich.
- Burisch, M., Gerdes, A., Walter, B.F., Neumann, U., Fettel, M., Markl, G., 2017. Methane and the origin of five-element veins: Mineralogy, age, fluid inclusion chemistry and ore forming processes in the Odenwald, SW Germany. *Ore Geol. Rev.* 81, 42–61.
- Burisch, M., Walter, B.F., Gerdes, A., Lanz, M., Markl, G., 2018. Late-stage anhydrite-gypsum-siderite-dolomite-calcite assemblages record the transition from a deep to a shallow hydrothermal system in the Schwarzwald mining district, SW Germany. *Geochim. Cosmochim. Acta* 223, 259–278.
- Burisch, M., Markl, G., Gutzmer, J., 2022. Breakup with benefits-hydrothermal mineral systems related to the disintegration of a supercontinent. *Earth Planet. Sci. Lett.* 580, 117373.
- Burley, S.D., Mullis, J., Matter, A., 1989. Timing diagenesis in the Tartan Reservoir (UK North Sea): constraints from combined cathodoluminescence microscopy and fluid inclusion studies. *Mar. Pet. Geol.* 6 (2), 98–104.
- Came, R.E., Azmy, K., Tripathi, A.K., Olanipekun, B.-J., 2017. Comparison of clumped-isotope signatures of dolomite cements to fluid-inclusion thermometry in the temperature range of 73–176 °C. *Geochim. Cosmochim. Acta* 199, 31–47.
- Campbell, K.A., Farmer, J.D., Des Marais, D., 2002. Ancient hydrocarbon seeps from the Mesozoic convergent margin of California: carbonate geochemistry, fluids and palaeoenvironments. *Geofluids* 2, 63–94.
- Chen, D., Qing, H., Yang, C., 2004. Multistage hydrothermal dolomites in the Middle Devonian (Givetian) carbonates from the Guilin area, South China. *Sedimentology* 51, 1029–1051.
- Chen, S., Ryb, U., Piasecki, A.M., Lloyd, M.K., Baker, M.B., Eiler, J.M., 2019. Mechanism of solid-state clumped-isotope reordering in carbonate minerals from aragonite heating experiments. *Geochim. Cosmochim. Acta* 258, 156–173.
- Cramer, B.D. and Jarvis, I., 2020. Carbon Isotope Stratigraphy. In: Gradstein, F.M., Ogg, J.G., Schmitz, M.D. and Ogg, G.M., 2020 (eds.). *Geologic Time Scale 2020*, Elsevier: 309–343.
- Czerniakowski, L.A., Lohmann, K.C., Wilson, J.L., 1984. Closed-system marine burial diagenesis: isotopic data from the Austin Chalk and its components. *Sedimentology* 31 (6), 863–877.
- Davisson, M.L., Criss, R.E., 1996. Na-Ca-Cl relations in basinal fluids. *Geochim. Cosmochim. Acta* 60, 2743–2752.
- De Riese, T., Bons, P.D., Gomez-Rivas, E., Sachau, T., 2020. Interaction between Crustal-Scale Darcy and Hydrofracture Fluid Transport: A Numerical Study. *Geofluids* 2020 (3), 1–14.
- Dickson, J.A.D., 1990. Carbonate mineralogy and chemistry. In: Tucker, M.E., Wright, V. P. (Eds.), *Carbonate Sedimentology*. Blackwell Scientific, Oxford, pp. 284–313.
- Dong, S., Chen, D., Zhou, X., Qian, Y., Tian, M., Qing, H., 2017. Tectonically driven dolomitization of Cambrian to Lower Ordovician carbonates of the Qurqutagh area, north-eastern flank of Tarim Basin, north-west China. *Sedimentology* 64, 1079–1106.
- Drozdowski, G., Hartkopf-Fröder, C., Lange, F.-G., Oesterreich, B., Ribbert, K.-H., Voigt, S. and Wrede, V., 1998. Vorläufige Mitteilung über unterkretazischen Tiefenkarst im Wülfrather Massenkalk (Rheinisches Schiefergebirge). - *Mitt. Verb. Dt. Höhlen- u. Karstforsch.*, 44(2): 53-66; München.
- Drozdowski, G., Wrede, V., 1994. Faltung und Bruchtektonik – Analyse der Tektonik im Subvariscikum. *Fortschr. Geol. Rheinl. Westfal.* 38, 7–187.
- Drozdowski, G., Richter, D.K., Wrede, V., 2017. Hydrothermalkarst im nördlichen Rheinischen Schiefergebirge. *Verband der Deutschen Höhlen und Karstforscher e. V.* München, p. 89.
- Epp, T., Walter, B.F., Scharrer, M., Lehmann, G., Henze, K., Heimgärtner, C., Markl, G., 2019. Quartz veins with associated Sb-Pb-Ag±Au mineralization in the Schwarzwald, SW Germany: a record of metamorphic cooling, tectonic rifting, and element remobilization processes in the Variscan belt. *Miner. Deposita* 54, 281–306.
- Fantle, M.S., Bullen, T.D., 2009. Essentials of iron, chromium, and calcium isotope analysis of natural materials by thermal ionization mass spectrometry. *Chem. Geol.* 258, 50–64.
- Fantle, M.S., Barnes, B.D., Lau, K.V., 2020. The role of diagenesis in shaping the geochemistry of the marine carbonate record. *Annu. Rev. Earth Planet. Sci.* 48, 549–583.
- Ferry, J.M., Wing, B.A., Penniston-Dorland, S.C., Rumble, D., 2002. The direction of fluid flow during contact metamorphism of siliceous carbonate rocks: new data for the Monzoni and Predazzo aureoles, northern Italy, and a global review. *Contrib. Miner. Petrol.* 142, 679–699.
- Fichtner, V., Strauss, H., Mavromatis, V., Dietzel, M., Huthwelker, T., Borca, C.N., Guagliardo, P., Kilburn, M.R., Göttlicher, J., Pederson, C.L., Griesshaber, E., Schmah, W.W., Immenhauser, A., 2018. Incorporation and subsequent diagenetic alteration of sulfur in Arctic islandica. *Chem. Geol.* 482, 72–90.
- Flügel, E., 2004. *Microfacies of Carbonate Rocks - Analysis, interpretation and application*. Springer, 984 p.
- Folk, R.L., 1965. Some aspects of recrystallization in ancient limestones. In: Pray, L.C. and Murray, R.C. (eds.) *Dolomitization and limestone diagenesis. SEPM Special Publication*, 13: 14–18.
- Franke, W., Cocks, L., Torsvik, T., 2020. Detrital zircons and the interpretation of palaeogeography, with the Variscan Orogeny as an example. *Geol. Mag.* 157 (4), 690–694.
- Frape, S.K., Fritz, P., McNutt, R.H., 1984. Water-rock interaction and chemistry of groundwaters from the Canadian Shield. *Geochim. Cosmochim. Acta* 48, 1617–1627.
- Frazer, M., Whitaker, F., Hollis, C., 2014. Fluid expulsion from overpressured basins: Implications for Pb-Zn mineralisation and dolomitisation of the East Midlands platform, northern England. *Mar. Pet. Geol.* 55, 68–86.
- Friedman, G.M., 1965. Terminology of crystallization textures and fabrics in sedimentary rocks. *J. Sediment. Petrol.* 35, 643–655.
- Fußwinkel, T., Wagner, T., Wenzel, T., Wälle, M., Lorenz, J., 2014. Red bed and basement sourced fluids recorded in hydrothermal Mn-Fe-As veins, Sailauf (Germany): A LA-ICPMS fluid inclusion study. *Chem. Geol.* 363, 22–39.
- Gabellone, T., Iannace, A., Gasparrini, M., 2014. Multiple Dolomitization Episodes In Deep-Water Limestones of the Triassic Lagonero Basin (Southern Italy): From Early Reflux To Tectonically Driven Fluid Flow. *J. Sediment. Res.* 84 (5), 435–456.
- Galante, C.E., Cioffi, C.R., Machado, J.P., Miranda, T., Lopes, L.B., Weinberg, R.F., Celestino, M.A., Carvalho, B., Guillon, M., Roberts, N.M.W., 2022. Recurrent tectonic activity in northeastern Brazil during Pangea breakup: Constraints from U-Pb carbonate dating. *Geology* 50 (8), 969–974.
- Gasparrini, M., Bechstadt, T., Boni, M., 2006. Massive hydrothermal dolomites in the southwestern Cantabrian Zone (Spain) and their relation to the Late Variscan evolution. *Mar. Pet. Geol.* 23 (5), 543–568.
- Gerdes, A., Zeh, A., 2006. Combined U-Pb and Hf isotope LA-(MC)-ICP-MS analyses of detrital zircons: comparison with SHRIMP and new constraints for the provenance and age of an Armorican metasediment in Central Germany. *Earth Planet. Sci. Lett.* 249, 47–61.
- Gerdes, A., Zeh, A., 2009. Zircon formation versus zircon alteration — new insights from combined U-Pb and Lu-Hf in-situ LA-ICP-MS analyses, and consequences for the interpretation of Archean zircon from the Central Zone of the Limpopo Belt. *Chem. Geol.* 261 (3–4), 230–243.
- Geske, A., Zorlu, J., Richter, D.K., Buhl, D., Niedermayr, A., Immenhauser, A., 2012. Impact of diagenesis and low grade metamorphism on isotope (⁶²⁶Mg, ⁶¹³C, ⁶¹⁸O and ⁸⁷Sr/⁸⁶Sr) and elemental (Ca, Mg, Mn, Fe and Sr) signatures of Triassic sabkha dolomites. *Chem. Geol.* 332–333, 45–64.
- Geske, A., Goldstein, R.H., Mavromatis, V., Richter, D.K., Buhl, D., Kluge, T., John, C.M., Immenhauser, A., 2015. The magnesium isotope (⁶²⁶Mg) signature of dolomites. *Geochim. Cosmochim. Acta* 149, 131–151.
- Gillhaus, A., Götze, T., Richter, D.K., 2003. Polyphase spätdiagenetische Dolomitbildung im mittel- bis oberdevonischen Massenkalk von Hagen-Hohenlimburg (Remscheid-Altenaer Sattel, Rheinisches Schiefergebirge). *Mitt. Ges. Geol. Bergbaustud. Österr.* 46, 51–66.
- Göb, S., Loges, A., Nolde, N., Bau, M., Jacob, D.E., Markl, G., 2013. Major and trace element compositions (including REE) of mineral, thermal, mine and surface waters in SW Germany and implications for water-rock interaction. *Appl. Geochem.* 33, 127–152.
- Goldstein, R.H., Reynolds, T.J., 1994. Systematics of fluid inclusions in diagenetic minerals. *Short Course 31. Society of Economic Paleontologists and Mineralogists* 31, 199 p.
- Götze, T., Richter, D.K., 2003. Late Paleozoic and Early Mesozoic hydrothermal events in the northern Rhinish Massif: results from uid inclusion analyses and cathodoluminescence investigations. *J. Geochem. Explor.* 78–79, 531–535.
- Götze, T., 2004. Petrographische und geochemische Untersuchungen zu den postvariszischen Mineralisationen im devonischen Massenkalk des nordwestlichen Rechtsrheinischen Schiefergebirges unter besonderer Berücksichtigung der Kathodolumineszenz. *Dissertation University of Bochum*, 186 p.

- Grossman, E.L. and Joachimski, M.M., 2020. Oxygen Isotope Stratigraphy. In: Gradstein, F.M., Ogg, J.G. and Schmitz, M.D., 2020. *Geologic Time Scale 2020*: 279–307.
- Guillong, M., Wotzlaw, J.F., Looser, N., Laurent, O., 2020. Evaluating the reliability of U-Pb laser ablation inductively coupled plasma mass spectrometry (LA-ICP-MS) carbonate geochronology: matrix issues and a potential calcite validation reference material. *Geochronology* 2, 155–167.
- Guo, C., Chen, D., Qing, H., Dong, S., Li, G., Wang, D., Qian, Y., Liu, C., 2016. Multiple dolomitization and later hydrothermal alteration on the Upper Cambrian-Lower Ordovician carbonates in the northern Tarim Basin, China. *Mar. Pet. Geol.* 72, 295–316.
- Hammerschmidt, E., Niggemann, S., Grebe, W., Oelze, R., Brix, M.R., Richter, D.K., 1995. Höhlen in Iserlohn. *Schriften Zur Karst- Und Höhlenkunde in Westfalen* 1, 1–182.
- Hejilun, W., Muchez, P., Banks, D.A., 2001. Origin and evolution of high-salinity, Zn-Pb mineralising fluids in the Variscides of Belgium. *Miner. Deposita* 36, 165–176.
- Higgins, J.A., Blättler, C.L., Lundstrom, E.A., Santiago-Ramos, D.P., Akhtar, A.A., Ahm, A.-S.-C., Bialik, O., Holmden, C., Bradbury, H., Murray, S.T., Swart, P.K., 2018. Mineralogy, early marine diagenesis, and the chemistry of shallow-water carbonate sediments. *Geochim. Cosmochim. Acta* 220, 512–534.
- Hips, K., Haas, J., Györi, O., 2016. Hydrothermal dolomitization of basinal deposits controlled by a synsedimentary fault system in Triassic extensional setting, Hungary. *Int J Earth Sci (geol Rundsch)* 105, 1215–1231.
- Hitzman, M.W., Allan, J.R., Beaty, D.W., 1998. Regional dolomitization of the Waulsortian limestone in southeastern Ireland: Evidence of large-scale fluid flow driven by the Hercynian orogeny. *Geology* 26 (6), 547–550.
- Holness, M.B., Fallick, A.E., 2004. Palaeohydrology of the calcisilicate aureole of the Beinn an Dubhaich granite, Skye, Scotland: a stable isotopic study. *J. Metam. Geol.* 15, 71–83.
- Honlet, R., Gasparrini, M., Muchez, P., Swennen, R., John, C.M., 2018. A new approach to geobarometry by combining fluid-inclusion and clumped-isotope thermometry in hydrothermal carbonates. *Terra Nova* 30, 199–206.
- Horita, J., 2014. Oxygen and carbon isotope fractionation in the system dolomite–water–CO₂ to elevated temperatures. *Geochim. Cosmochim. Acta* 129, 111–124.
- Horstwood, M.S.A., Košler, J., Gehrels, G., Jackson, S.E., McLean, N.M., Paton, C., Pearson, N.J., Sircombe, K., Sylvester, P., Vermeesch, P., Bowring, J.F., 2016. Community-derived standards for LA-ICP-MS U-(Th)-Pb geochronology-Uncertainty propagation, age interpretation and data reporting. *Geostand. Geoanal. Res.* 40, 311–332.
- Immenhauser, A., 2022. On the delimitation of the carbonate burial realm. *Depositional Rec.* 8 (2), 524–574.
- Immenhauser, A., Hoffmann, R., Riechelmann, S., Mueller, M., Scholz, D., Voigt, S., Niggemann, S., Buhl, D., Dornseif, M., Platte, A., 2023. Petrographic and geochemical constraints on the formation of gravity-defying speleothems. *The Depositional Record* 9 (3), 413–436.
- Jébrak, M., 1997. Hydrothermal breccias in vein-type ore deposits: a review of mechanisms, morphology and size distribution. *Ore Geol. Rev.* 12 (3), 111–134.
- Jochum, K.P., Weis, U., Stoll, B., Kuzmin, D., Yang, Q., Raczek, I., Jacob, D.E., Stracke, A., Birbaum, K., Frick, D.A., Günther, D., Enzweiler, J., 2011. Determination of reference values for NIST SRM 610–617 glasses following ISO guidelines. *Geostand. Geoanal. Res.* 35, 97–429.
- Kamp, H.V., 1968. Hauptversammlung der Deutschen Geologischen Gesellschaft in Hagen/Westfalen. *Excursion* 21–22.
- Kaufman, A.J., Hayes, J.M., Knoll, A.H., Germs, G.J.B., 1991. Isotopic compositions of carbonates and organic carbon from upper Proterozoic successions in Namibia: stratigraphic variation and the effects of diagenesis and metamorphism. *Precamb. Res.* 49 (3–4), 301–327.
- Kim, S.-T., O’Neil, J.R., 1997. Equilibrium and nonequilibrium oxygen isotope effects in synthetic carbonates. *Geochim. Cosmochim. Acta* 61, 3461–3475.
- Kirnbauer, Th., Schneider, J., Schwenzler, S.P., 1998. Geologie und hydrothermale Mineralisationen im rechtsrheinischen Schiefergebirge. *Nassauischer Verein Für Naturkunde Special Publication* 1, 327 p.
- Klein, C., 2005. Some Precambrian banded iron-formations (BIFs) from around the world: Their age, geologic setting, mineralogy, metamorphism, geochemistry, and origin. *Am. Miner.* 90, 1473–1499.
- Kley, J., 2013. Saxonische Tektonik im 21. Jahrhundert. *z. Dt. Ges. Geowiss. (german J. Geosci.)* 164 (2), 295–311.
- Klimchouk, A., Palmer, A.N., De Waele, J., Auler, A.S. and Audra, P. (eds.), 2017. *Hypogene Karst Regions and Caves of the World*. Springer, 911 p.
- Koch, L., Voigt, S., Brauckmann, C., 2018. Nautiliden aus der Klutertöhle (Ennepetal, Nordrhein-Westfalen), aus benachbarten Höhlen und weiteren Fundorten in Oberen Honsel Schichten (Unter-Givetium). *Geologie Und Paläontologie in Westfalen* 90, 15–24.
- Kolchugin, A., Immenhauser, A., Morozov, V., Walter, B., Eskin, A., Korolev, E., Neuser, R., 2020. A comparative study of two Mississippian dolostone reservoirs in the Volga-Ural Basin, Russia. *J. Asian Earth Sci.* 199, 104465.
- Krebs, W., 1974. Devonian carbonate complexes of central Europe. In: *The Society of Economic Paleontologists and Mineralogists (SEPM) - Reefs in Time and Space*, 18: 155–208.
- Kreissl, S., Gerdes, A., Walter, B.F., Neumann, U., Wenzel, T., Markl, G., 2018. Reconstruction of a > 200 Ma multi-stage “five element” Bi-Co-Ni-Fe-As-S system in the Penninic Alps, Switzerland. *Ore Geol. Rev.* 95, 746–788.
- Lange, S.M., Krause, S., Ritter, A.-C., Fichtner, V., Immenhauser, A., Strauss, H., Treude, T., 2018. Anaerobic microbial activity affects earliest diagenetic pathways of bivalve shells. *Sedimentology* 65, 1390–1411.
- Lanser, K.P., Heimhofer, U., 2015. Evidence of theropod dinosaurs from a Lower Cretaceous karst filling in the northern Sauerland (Rhenish Massif, Germany). *Paläontol. z.* 89, 79–94.
- Laskar, A.H., Yui, T.F., Liang, M.C., 2016. Clumped isotope composition of marbles from the Backbone Range of Taiwan. *Terra Nova* 28 (4), 265–270.
- Lippert, K., Ahrens, B., Nehler, M., Balcewicz, M., Mueller, M., Bracke, R. and Immenhauser, A., 2022. Geothermal reservoir characterization of Devonian carbonates in North Rhine-Westphalia (W. Germany): Mineralogy- and depofacies-related extrapolation of petrophysical parameters. *Geothermics*, 106(4): 102549.
- Littke, R., Bükler, C., Hertle, M., Karg, H., Stroetmann-Heinen, V. and Oncken, O., 2000. Heat flow evolution, subsidence and erosion in the Rheno-Hercynian orogenic wedge of central Europe. In W. Franke, V. Haak, O. Oncken, and D. Tanner (eds.), *Orogenic processes: Quantification and modelling in the Variscan Belt. Special Publication – Geological Society of London*, 179: 231–255.
- Liu, S., Huang, W., Jansa, L.F., Wang, G., Song, G., Zhang, C., Sun, W., Ma, W., 2014. Hydrothermal dolomite in the upper Sinian (upper Proterozoic) Dengying formation, east Sichuan basin, China. *Acta Geologica Sinica-English Edition* 88, 1466–1487.
- Lloyd, M.K., Ryb, U., Eiler, J.M., 2018. Experimental calibration of clumped isotope reordering in dolomite. *Geochim. Cosmochim. Acta* 242, 1–20.
- Lohmann, K.C., 1988. Geochemical patterns of meteoric diagenetic systems and their application to studies of paleokarst. In: James, N.P., Choquette, P.W. (Eds.), *Paleokarst*. Springer-Verlag, New York, pp. 58–80.
- Löw, M., Söte, T., Becker, R.T., Stichling, S., May, A., Aboussalam, Z.S., Zoppe, S.F., 2022. The initial phase of the Hönne Valley Reef at Binolen (northern Rhenish Massif, Middle Devonian). *Palaeobio Palaeogeogr.* 102, 573–612.
- Lüders, V., Plessen, B., Romer, R.L., Weise, S.M., Banks, D.A., Hoth, P., Dulski, P., Schettler, G., 2010. Chemistry and isotopic composition of Rotliegend and Upper Carboniferous formation waters from the North German Basin. *Chem. Geol.* 276, 198–208.
- Ludwig, K.R., 2012. User’s Manual for Isoplot Version 3.75–4.15: a Geochronological Toolkit for Microsoft Excel. Berkeley Geochronological Center Special Publication, p. 5.
- Maccaffrey, M.A., Lazar, B.H.D.H., Holland, H.D., 1987. The evaporation path of seawater and the coprecipitation of Br (super-) and K (super+) with halite. *J. Sediment. Petrol.* 57, 928–937.
- Maillard, A., Mauffret, A., 1999. Crustal structure and riftogenesis of the Valencia Trough (north-western Mediterranean Sea). *Basin Res.* 11 (4), 357–379.
- Mangenot, X., Bonifacie, M., Gasparrini, M., Götz, A., Chaduteau, C., Ader, M., Rouchon, V., 2017. Coupling $\Delta 47$ and fluid inclusion thermometry on carbonate cements to precisely reconstruct the temperature, salinity and $\delta^{18}O$ of paleo-groundwater in sedimentary basins. *Chem. Geol.* 472, 44–57.
- Mangenot, X., Gasparrini, M., Gerdes, A., Bonifacie, M., Rouchon, V., 2018. An emerging thermochronometer for carbonate-bearing rocks: $\Delta 47$ / (U-Pb). *Geology* 46 (12), 1067–1070.
- Martin, T., Averianov, A.O., Schultz, J.A., Schwermann, A.H., 2021. First multituberculate mammals from the Lower Cretaceous of Germany. *Cretac. Res.* 119, 104699.
- Mavromatis, V., Purgstaller, B., Dietzel, M., Buhl, D., Immenhauser, A., Schott, J., 2017. Impact of amorphous precursor phases on magnesium isotope signatures of Mg-calcite. *Earth Planet. Sci. Lett.* 464, 227–236.
- McArthur, J.M., Howarth, R.J., Shields, G.A. and Zhou, Y., 2020. Strontium Isotope Stratigraphy. In: Gradstein, F.M., Ogg, J.G., Schmitz, M.D. and Ogg, G.M., 2020. *Geologic Time Scale 2020*, Elsevier, 211–238.
- Melezhik, V.A., Zwaan, B.K., Motuza, G., Roberts, D., Solli, A., Fallick, A.E., Gorokhov, I.M., Kusnetzov, A.B., 2003. New insights into the geology of high-grade Caledonian marbles based on isotope chemostratigraphy. *Norwegian Journal of Geology/norsk Geologisk Forening* 83, 209–242.
- Melezhik, V.A., Roberts, D., Fallick, A.E., Gorokhov, I.M., Kusnetzov, A.B., 2005. Geochemical preservation potential of high-grade calcite marble versus dolomite marble: implication for isotope chemostratigraphy. *Chem. Geol.* 216, 203–224.
- Millán, M.I., Machel, H., Bernasconi, S.M., 2016. Constraining Temperatures of Formation and Composition of Dolomitizing Fluids in the Upper Devonian Nisku Formation (Alberta, Canada) with Clumped Isotopes. *Journal of Sedimentary Research* 86 (1), 107–112.
- Moore, C.H. and Wade, W.J., 2013. Carbonate Diagenesis: Introduction and Tools. In: Moore, C.H. and Wade, W.J. (eds.), 2013. *Developments in Sedimentology*. 67: 67–89.
- Mueller, M., Igbokwe, O.A., Walter, B., Pederson, C.L., Riechelmann, S., Richter, D.K., Albert, R., Gerdes, A., Buhl, D., Neuser, R.D., Bertotti, G., Immenhauser, A., 2020. Testing the preservation potential of early diagenetic dolomites as geochemical archives. *Sedimentology* 67, 849–881.
- Mueller, M., Jacquemyn, C., Walter, B.F., Pederson, C.L., Schurr, S.L., Igbokwe, O.A., Jöns, N., Riechelmann, S., Dietzel, M., Immenhauser, A., 2022a. Constraints on the preservation of proxy data in carbonate archives: lessons from a marine limestone to marble transect, Latemar, Italy. *Sedimentology* 69, 423–460.
- Mueller, M., Walter, B.F., Swart, P.K., Jöns, N., Jacquemyn, C., Igbokwe, O.A., Immenhauser, A., 2022b. A tale of three fluids: Fluid-inclusion and carbonate clumped-isotope paleothermometry reveals complex dolomitization and dedolomitization history of the Latemar platform. *J. Sediment. Res.* 92 (12), 1141–1168.
- Mueller, M., Walter, B.F., Beranoguirre, A., Heinelt, M., Immenhauser, A., 2023. Hydrothermal karst cavities in a Devonian carbonate reservoir analogue (Rhenish Massif, Germany): Implications for geothermal energy potential. *Symposium on Energy Geotechnics 2023*, 1–2.

- Neuser, R.D., Bruhn, F., Götze, J., Habermann, D., Richter, D.K., 1996. Kathodolumineszenz: Methodik und Anwendung [Cathodoluminescence: method and application]. *Zbl. Geol. Paläont. Teil 1*, 287.
- Nielsen, P., Swennen, R., Muhez, P., Keppens, E., 1998. Origin of Dinantian zebra dolomite south of the Brabant-Wales Massif, Belgium. *Sedimentology* 45 (4), 727–743.
- Niggemann, S., Richter, D.K., Hammerschmidt, E., Dreyer, R., Grebe, W., Platte, A., 2018. Dechenhöhle -Erdgeschichten. Müllerdruck, Iserlohn, p. 301.
- Nordeng, S.H., Sibley, D.F., 1994. Dolomite stoichiometry and Ostwald's step rule. *Geochim. Cosmochim. Acta* 58, 191–196.
- Nöth, S., Karg, H., Littke, R., 2001. Reconstruction of Late Paleozoic heat flows and burial histories at the Rhenohercynian-Subvariscan boundary, Germany. *Int. J. Earth Sciences* 90, 234–256.
- Oliver, J., 1986. Fluids expelled tectonically from orogenic belts: Their role in hydrocarbon migration and other geologic phenomena. *Geology* 14, 99–102.
- Oncken, O., 1988. Aspects of the reconstruction of the stress history of a fold and thrust belt (Rhenish Massif, Federal Republic of Germany). *Tectonophysics* 152 (1–2), 19–40.
- Osborne, M.J., Swarbrick, R.E., 1997. Mechanisms for Generating Overpressure in Sedimentary Basins: A reevaluation. *AAPG Bull.* 81 (6), 1023–1041.
- Pagel, M., Bonifacie, M., Schneider, D.A., Gautheron, C., Brigaud, B., Calmels, D., Cros, A., Saint-Bezar, B., Landrein, P., Sutcliffe, C., Davis, D., 2018. Improving paleohydrological and diagenetic reconstructions in calcite veins and breccia of a sedimentary basin by combining Δ_47 temperature, $\delta^{18}\text{O}$ water and U-Pb age. *Chem. Geol.* 481, 1–17.
- Passey, B.H., Henkes, G.A., 2012. Carbonate clumped isotope bond reordering and geospeedometry. *Earth Planet. Sci. Lett.* 351–352, 223–236.
- Pastor-Galán, D., Groenewegen, T., Brouwer, D., Krijgsman, W., Dekkers, M.J., 2015. One or two oroclines in the Variscan orogen of Iberia? Implications for Pangea Amalgamation. *Geology* 43 (6), 527–530.
- Pauwels, H., Fouillac, C., Fouillac, A.M., 1993. Chemistry and isotopes of deep geothermal saline fluids in the Upper Rhine Graben: origin of compounds and water-rock interactions. *Geochim. Cosmochim. Acta* 57, 2737–2749.
- Peacock, D.C.P., Rotevatn, A., Sanderson, D.J., 2019. Brecciation driven by changes in fluid column heights. *Terra Nova* 31, 76–81.
- Pederson, C., Mavromatis, V., Dietzel, M., Rollion-Bard, C., Nehrke, G., Jöns, N., Jochum, K.P., Immenhauser, A., 2019. Diagenesis of mollusc aragonite and the role of fluid reservoirs. *Earth Planet. Sci. Lett.* 514, 130–142.
- Pederson, C.L., Mavromatis, V., Dietzel, M., Rollion-Bard, C., Breitenbach, S.F.M., Yu, D., Nehrke, G., Immenhauser, A., 2020. Variation in the diagenetic response of aragonite archives to hydrothermal alteration. *Sed. Geol.* 406, 105716.
- Pederson, C., Mueller, M., Lippert, K., Igbokwe, O.A., Riechelmann, S., Lersch, S., Benger, P., Verdecchia, A., Immenhauser, A., 2021. Impact of a regional fault zone on the properties of a deep geothermal carbonate reservoir unit (Devonian of NRW). *Z. Dt. Ges. Geowiss. (J. Appl. Reg. Geol.)* 172, 339–364.
- Peng, B., Li, G., Li, Z., Liu, C., Zuo, Y., Zhang, W., Yuan, L., Zhao, S., Yao, C., 2018. Discussion of multiple formation mechanisms of saddle dolomites—comparison of geochemical data of Proterozoic-Paleozoic dolomites. *Energy Explor. Exploit.* 36, 66–96.
- Perrin, C., Smith, D.C., 2007. Earliest Steps of Diagenesis in Living Scleractinian Corals: Evidence from Ultrastructural Pattern and Raman Spectroscopy. *J. Sediment. Res.* 77 (6), 495–507.
- Preto, N., Breda, A., Dal Corso, J., Spötl, C., Zorzi, F., Frisia, S., 2015. Primary dolomite in the Late Triassic Travenanzes Formation, Dolomites, Northern Italy: Facies control and possible bacterial influence. *Sedimentology* 62 (3), 697–716.
- Rasbury, E.T., Cole, J.M., 2009. Directly dating geologic events: U-Pb dating of carbonates. *Rev. Geophys.* 47, RG3001.
- Rddad, L., Kraemer, D., Walter, B.F., Darling, R., Cousens, B., 2022. Unravelling the fluid flow evolution and precipitation mechanisms recorded in calcite veins in relation to Pangea rifting—Newark Basin, USA. *Geochemistry* 82 (4), 125918.
- Richter, D.K., 2000. Die Eifeler Nord-Süd-Zone: Vom Devonmeer zur Kulturhöhle. *Bochumer Geol. U. Geotech. Arb.* 55, 205–222.
- Richter, D.K., Götze, Th., Götze, J., Neuser, R.D., 2003. Progress and application of cathodoluminescence in sedimentary petrology. *Mineral. and Petrol.* 79 (3–4), 127–166.
- Richter, D.K., Mueller, M., Platte, A., Scholz, D., 2020. Erste weichselzeitliche Kryocalcite im Attendorf-Elsper Riffkomplex (Frettermühler Wasserhöhle, Südwestfalen). *Geologie Und Paläontologie in Westfalen* 93, 1–16.
- Roberts, N.M.W., Rasbury, E.T., Parrish, R.R., Smith, C.J., Horstwood, M.S.A., Condon, D.J., 2017. A calcite reference material for LA-ICP-MS U-Pb geochronology. *Geochemistry, Geophysics, Geosystem* 18, 2807–2814.
- Rosenfeld, U., 1961. Der Massenkalk des nördlichen Sauerlandes. *Mitteilungen Des Verbandes Der Deutschen Höhlen- Und Karstforscher* 7, 41–64.
- Schaeffer, R., 1984. Die postvariszische Mineralisation im nordöstlichen Rheinischen Schiefergebirge. *Bswg. Geol.-Paläont. Diss.* 3, 206 p.
- Schulmann, K., Martinez Catalan, J. R., Lardeaux, J. M., Janousek, V. and Oggiano, G. (eds.), 2014. *The Variscan Orogeny: Extent, Timescale and the Formation of the European Crust. Geological Society, London, Special Publications*, 405: 1–6.
- Schurr, S., Strauss, H., Mueller, M., Immenhauser, A., 2021. Assessing the robustness of carbonate-associated sulfate during hydrothermal dolomitization of the Latemar platform. *Italy. Terra Nova* 33 (6), 621–629.
- Sengör, A.M.C., and Natal'in, B.A., 2001. Rifts of the world. In: Ernst, R.E. and Buchan, K.L. (eds.), *Mantle Plumes: Their Identification Through Time: Geological Society of America Special Paper*, 352: 389–482.
- Sharma, T., Clayton, R.N., 1965. Measurement of $\text{O}^{18}/\text{O}^{16}$ ratios of total oxygen of carbonates. *Geochim. Cosmochim. Acta* 29, 1347–1353.
- Sheppard, S.M., Schwarz, H.P., 1970. Fractionation of carbon and oxygen isotopes and magnesium between coexisting metamorphic calcite and dolomite. *Contrib. Miner. Petrol.* 26, 161–198.
- Sibley, D.F., Gregg, J.M., 1987. Classification of Dolomite Rock Texture. *J. Sediment. Petrol.* 57, 967–975.
- Spence, G.H., Le Heron, D., Fairchild, I.J., 2016. Sedimentological perspective on climate, atmospheric and environmental change in the Neoproterozoic Era. *Sedimentology* 63, 253–306.
- Staudigel, P.T., Swart, P.K., 2016. Isotopic behavior during the aragonite–calcite transition: implications for sample preparation and proxy interpretation. *Chem. Geol.* 442, 130–138.
- Stichling, S., Becker, R.T., Hartenfels, S., Aboussalam, Z.S., May, A., 2022. Drowning, extinction, and subsequent facies development of the Devonian Hönne Valley Reef (northern Rhenish Massif, Germany). *Palaeobiodivers. Palaeoenviro.* 102, 629–696.
- Stober, I., Bucher, K., 2004. Fluid sinks within the earth's crust. *Geofluids* 4, 143–151.
- Stolper, D.A., Eiler, J.M., 2015. The kinetics of solid-state isotope-exchange reactions for clumped isotopes: a study of inorganic calcites and apatites from natural and experimental samples. *Am. J. Sci.* 315, 363–411.
- Swart, P.K., 2015. The geochemistry of carbonate diagenesis: The past, present and future. *Sedimentology* 62, 1233–1304.
- Swart, P.K., Murray, S.T., Staudigel, P.T., Hodell, D.A., 2019. Oxygen isotopic exchange between CO_2 and phosphoric acid: Implications for the measurement of clumped isotopes in carbonates. *Geochem. Geophys. Geosyst.* 20, 3730–3750.
- Tingay, M.R.P., Hillis, R.R., Swarbrick, R.E., Morley, C.K., Damit, R., 2007. 'Vertically transferred' overpressures in Brunei: Evidence for a new mechanism for the formation of high-magnitude overpressure. *Geology* 35 (11), 1023–1026.
- Udflut, H., 1929. Die Genesis der flächenhaft verbreiteten Dolomite des mitteldevonischen Massenkalkes, insbesondere des Schwelmer Kalkes der Gegend von Elberfeld-Barmen. *Jb. Preuß. Geol. Landesanst. Berlin, Band L 1*, 396–436.
- Vandeginste, V., John, C.M., Cosgrove, J.W., Manning, C., 2014. Dimensions, texture distribution, and geochemical heterogeneities of fracture-related dolomite geobodies hosted in Ediacaran limestones, northern Oman. *AAPG Bull.* 98 (9), 1789–1809.
- Veizer, J., Prokoph, A., 2015. Temperatures and oxygen isotopic composition of Phanerozoic oceans. *Earth Sci. Rev.* 146, 92–104.
- Veizer, J., Ala, D., Azmy, K., Bruckschen, P., Buhl, D., Bruhn, F., Carden, G.A.F., Diener, A., Ebneth, S., Godderis, Y., Jasper, T., Korte, C., Pawellek, F., Podlaha, O.G., Strauss, H., 1999. $^{87}\text{Sr}/^{86}\text{Sr}$, $\delta^{13}\text{C}$ and $\delta^{18}\text{O}$ evolution of Phanerozoic seawater. *Chem. Geol.* 161, 59–88.
- Walter, B.F., Immenhauser, A., Geske, A., Markl, G., 2015. Exploration of hydrothermal carbonate magnesium isotope signatures as tracers for continental fluid aquifers, Schwarzwald mining district, SW Germany. *Chem. Geol.* 400, 87–105.
- Walter, B.F., Gerdes, A., Kleinhanns, I.C., Dunkl, I., von Eynatten, H., Kreissl, S., Markl, G., 2018a. The connection between hydrothermal fluids, mineralization, tectonics and magmatism in a continental rift setting: fluorite Sm-Nd and hematite and carbonates U-Pb geochronology from the Rhinegraben in SW Germany. *Geochim. Cosmochim. Acta* 240, 11–42.
- Walter, B.F., Burisch, M., Fusswinkel, T., Marks, M.A., Steele-MacInnis, M., Wälle, M., Apukhtina, O.B., Markl, G., 2018b. Multi-reservoir fluid mixing processes in rift-related hydrothermal veins, Schwarzwald, SW-Germany. *J. Geochem. Explor.* 186, 158–186.
- Walter, B.F., Kortenbruck, P., Scharrer, M., Zeitvogel, C., Wälle, M., Mertz-Kraus, R., Markl, G., 2019. Chemical evolution of ore-forming brines—Basement leaching, metal provenance, and the redox link between barren and ore-bearing hydrothermal veins. A case study from the Schwarzwald mining district in SW-Germany. *Chem. Geol.* 506, 126–148.
- Walter, B.F., Steele-MacInnis, M., Giebel, R.J., Marks, M.A.W., Markl, G., 2020a. Complex carbonate-sulfate brines in fluid inclusions from carbonatites: Estimating compositions in the system $\text{H}_2\text{O}-\text{Na}-\text{K}-\text{CO}_3-\text{SO}_4-\text{Cl}$. *Geochim. Cosmochim. Acta* 277, 224–242.
- Walter, B.F., Scharrer, M., Burisch, M., Apukhtina, O., Markl, G., 2020b. Limited availability of sulfur promotes copper-rich mineralization in hydrothermal Pb-Zn veins: A case study from the Schwarzwald, SW Germany. *Chemical Geology* 532, 119358.
- Xiong, L., Yao, G., Xiong, S., Wang, J., Ni, C., Shen, A., Hao, Y., 2018. Origin of dolomite in the Middle Devonian Guanwushan Formation of the western Sichuan Basin, western China. *Palaeogeogr. Palaeoclimatol. Palaeoecol.* 495, 113–126.
- Yao, Q., Demicco, R.V., 1995. Paleoflow patterns of dolomitizing fluids and paleohydrogeology of the southern Canadian Rocky Mountains: Evidence from dolomite geometry and numerical modeling. *Geology* 23, 791–794.
- Yardley, B.W.D., 2005. Metal concentrations in crustal fluids and their relationship to ore formation. *Econ. Geol.* 100, 613–632.
- Zou, Y., You, D., Chen, B., Yang, H., Tian, Z., Liu, D., Zhang, L., 2023. Carbonate U-Pb Geochronology and Clumped Isotope Constraints on the Origin of Hydrothermal Dolomites: A Case Study in the Middle Permian Qixia Formation, Sichuan Basin, South China. *Minerals* 13 (2), 223.